

Studying protein unfolding and translocation by the protease FtsH with optical tweezers

Overtoom-van Aartrijk, C.M.M.

DOI

[10.4233/uuid:c00bad95-f968-4693-a278-f96cc9489503](https://doi.org/10.4233/uuid:c00bad95-f968-4693-a278-f96cc9489503)

Publication date

2023

Document Version

Final published version

Citation (APA)

Overtoom-van Aartrijk, C. M. M. (2023). *Studying protein unfolding and translocation by the protease FtsH with optical tweezers*. [Dissertation (TU Delft), Delft University of Technology].
<https://doi.org/10.4233/uuid:c00bad95-f968-4693-a278-f96cc9489503>

Important note

To cite this publication, please use the final published version (if applicable).
Please check the document version above.

Copyright

Other than for strictly personal use, it is not permitted to download, forward or distribute the text or part of it, without the consent of the author(s) and/or copyright holder(s), unless the work is under an open content license such as Creative Commons.

Takedown policy

Please contact us and provide details if you believe this document breaches copyrights.
We will remove access to the work immediately and investigate your claim.

**Studying protein unfolding and
translocation by the protease FtsH with
optical tweezers**

Studying protein unfolding and translocation by the protease FtsH with optical tweezers

Dissertation

for the purpose of obtaining the degree of doctor
at Delft University of Technology
by the authority of the Rector Magnificus, prof. dr. ir. T.H.J.J. van der
Hagen,
chair of the Board for Doctorates
to be defended publicly on
Wednesday 13 December 2023 at 10.00 o'clock

by

Chaline Maria Margerethe OVERTOOM-VAN AARTRIJK

Master of Science in Physics and Astronomy,
Radboud University, Nijmegen, The Netherlands
Born in Hilversum, The Netherlands

This dissertation has been approved by the promotor.

Composition of the doctoral committee:

Rector Magnificus,	chairperson
Dr. M.-E. Aubin-Tam	Delft University of Technology, promotor
Dr. A. Jakobi	Delft University of Technology, copromotor

Independent members:

Prof.dr. C. Joo	Delft University of Technology
Prof.dr.ir. S.J. Tans	Delft University of Technology
Prof.dr. J. Lipfert	University of Utrecht
Dr. K.S. Grubmayer	Delft University of Technology
Dr. I. Heller	VU Amsterdam



Keywords: FtsH, optical tweezers, membrane protein
Printed by: Gildeprint
Cover by: Chaline Maria Margerethe Overtoom-van Aartrijk

Copyright ©2023 by C.M.M. Overtoom-van Aartrijk
ISBN 978-94-6384-518-2
Casimir PhD series

An electronic version of this dissertation is available at
<http://repository.tudelft.nl/>

Contents

Summary	1
Samenvatting	3
1 Introduction	5
1.1 FtsH, a protease of the AAA+ superfamily	6
1.1.1 The classical AAA clade of the AAA+ superfamily .	6
1.1.2 The discovery of FtsH and its essential function . . .	9
1.1.3 FtsH structure	10
1.1.4 Unfoldase activity of FtsH	14
1.2 I27 a module of the muscle protein titin, a model substrate for AAA+ proteases	16
1.2.1 The extensible muscle protein titin	16
1.2.2 The structure of titin module I27 and some point mutations	17
1.2.3 Mechanical stability of titin I27	19
1.3 Optical tweezers	21
1.3.1 Optical tweezers	21
1.3.2 Heating an optical tweezers sample	25
1.4 This thesis	26
References	28
2 Building and programming a dual trap optical tweezers setup	37
2.1 Introduction	38
2.2 Building a dual trap optical tweezers	39
2.2.1 The components on the optical table	39

Contents

2.2.2	Microscope	45
2.2.3	Electrical and mechanical noise	46
2.3	Programming optical tweezers	46
2.3.1	From LabVIEW to Python	46
2.4	Data acquisition and analysis	47
2.4.1	Alignment of the trapping and detection beams	47
2.4.2	Position calibration	49
2.4.3	Trap stiffness calibration	50
2.5	Passive force clamp experiment	52
2.5.1	Materials and method	52
2.5.2	Results	54
2.6	Discussion	55
2.6.1	Optical alignment	55
2.6.2	Programming	56
2.6.3	Passive force clamp	57
2.7	Supplementary material	58
2.7.1	Beam expander calculations	58
2.7.2	Data analysis equipartition method	58
	References	62
3	Local temperature sensing in optical tweezers with dual-sided heating approach	65
3.1	Introduction	66
3.2	Materials and methods: our design	68
3.2.1	Objective heating	68
3.2.2	Thermocouple	68
3.2.3	Copper flow cell	68
3.2.4	ITO flow cell	70
3.2.5	Sample preparation	71
3.2.6	Heating protocol	73
3.2.7	Equipartition method + Drag Force method (E-DF method)	73
3.2.8	Data acquisition and analysis of the E-DF method	74
3.2.9	Equipartition method + power spectrum method (E-PS method)	75
3.2.10	Data acquisition E-PS method	76

3.2.11	TEM (bead size)	76
3.3	Results and discussion	76
3.3.1	Confirming uniform heating of our flow cell designs .	76
3.3.2	The use of water vs. 'substitute oil' on water im- mersion objective	77
3.3.3	Impact of laser heating	80
3.3.4	Double sided heating	84
3.3.5	Objective heating	85
3.3.6	ITO heating	87
3.3.7	Temperature determination at different heights . . .	87
3.4	Conclusion	89
	References	92
4	Studying the mechanical properties of FtsH	95
4.1	Introduction	96
4.2	Materials and Methods	100
4.2.1	Substrate expression and purification	100
4.2.2	aaFtsH expression and purification	100
4.2.3	The aaFtsH heating flow cell	101
4.2.4	Optical tweezers experiment	102
4.2.5	Data analysis	103
4.3	Results and discussion	105
4.3.1	Observed aggregation during the aaFtsH experiment	105
4.3.2	Optimizing the aaFtsH experiment	108
4.3.3	Bead recordings of aaFtsH linked to I27 ^{V13P}	111
4.3.4	Bead recordings of aaFtsH linked to I27 ^{V15P}	116
4.3.5	Double tethered beads	116
4.4	Conclusion	118
4.5	Supplementary information	119
4.5.1	Aggregation observed during optical tweezers aaFtsH experiments	119
4.5.2	Bulk degradation of I27 ^{V13P} by aaFtsH	119
4.5.3	Luminescence results	120
4.5.4	AaFtsH aggregation	121
	References	123

Contents

5 Conclusion and outlook	127
5.1 Conclusion	128
5.2 Future work	130
References	133
Acknowledgements	137
Curriculum Vitæ	141

Summary

The AAA+ superfamily protease FtsH degrades misfolded and abundant proteins. These proteins may be located in the membrane or cytoplasm. Many FtsH substrates have been unraveled and its essential role in the bacterium *E. coli* established. However, the mechanism by which it unfolds and subsequently degrades its substrate is still under investigation.

Recently, full-length purification of FtsH was established. The purified full-length FtsH can be used to study this unfolding and degradation mechanism by optical tweezers. With one catch, the purified full-length FtsH is from a thermophilic bacterium and optical tweezers studies are generally performed at room temperature.

Before we could study FtsH, a heating system for optical tweezers was designed. The system consists of two parts: a heating microscope slide, that heats the sample from above; and an objective heating system, that heats the sample from below. The temperature increase of the objective is restricted, to prevent damage. Higher temperatures can be obtained by increasing the heat generated by the microscope slide.

The heating system has been validated by a thermocouple located ~ 2 mm from the trapped bead and two novel approaches to locally determine the temperature with the trapped bead. One of these approaches demonstrated to be a valid method and local temperatures were obtained from the trapped bead. However, the method requires knowledge of the viscosity and the change in viscosity due to temperature. On the other hand, this method combined with the thermocouple could be used to determine the change in viscosity due to temperature.

With the validated heating system, FtsH was studied and temperature was obtained from the thermocouple. The high temperature required for FtsH activity is close to the temperature at which the organic compounds

Summary

malfunction, this led to the inclusion of the thermocouple. However, even within the temperature range for which FtsH is active and the organic compounds do not malfunction, aggregation of enzymes in the experimental buffer was observed. The enzymes had to be excluded and may compromise the study.

As the experiment remained unsuccessful, the individual components were tested. This confirmed the presence and activity of the individual components. Unexpectedly, one of these tests showed that the tag used by FtsH to recognize the substrate seems to covalently bind to FtsH. This may explain why FtsH becomes inactive after prolonged degradation.

Unfortunately, no successful unfolding and degradation patterns were obtained. The unfolding and degradation mechanisms of FtsH remain thus unknown. Future studies are needed to find out whether the experimental conditions have the potential to inform us on FtsH's mechanism.

Samenvatting

De protease FtsH, die behoort tot de superfamilie AAA+, kan verkeerd gevouwen en overtollige eiwitten afbreken. Deze eiwitten kunnen zich bevinden in het membraam of in het cytoplasma. Veel van de substraten die FtsH afbreekt zijn gevonden en ook zijn essentiële rol in de bacterie *E. coli* is ontdekt. Echter, het mechanisme waarmee hij zijn substraten afbreekt wordt nog onderzocht.

Onlangs zijn wetenschappers erin geslaagd om intacte FtsH te purifiëren. Deze kan nu gebruikt worden om de wijze van ontvouwing en afbreken te demonstreren met behulp van een optische pincet. Helaas is de gepurificeerde FtsH alleen werkzaam bij hoge temperaturen. Dit komt doordat deze normaal gevonden wordt in een thermofiele bacterie. Metingen met de optische pincet worden normaal gesproken uitgevoerd op kamertemperatuur.

Alvorens we FtsH kunnen bestuderen moet er een verwarmingssysteem voor de optische pincet ontworpen worden. Het verwarmingssysteem bestaat uit twee delen: een microscoopglas dat het monster vanaf boven verwarmd en een objectief verwarmingssysteem dat het monster van onderaf verwarmd. De temperatuurtoename van het objectief is beperkt om schade aan het objectief te voorkomen. Hogere temperaturen kunnen worden bereikt door verwarming met het microscoopglasje.

De werking van het verwarmingssysteem is bevestigd door een temperatuursensor die zich ongeveer op 2 mm afstand bevindt van de gevangen kraal. Daarnaast zijn er twee nieuwe methodes gedemonstreerd en getest om de temperatuur nog dichterbij de bron te bepalen. Om dit te doen is voorkennis van de viscositeit en hoe deze verandert door een toenemende temperatuur nodig. Als deze niet beschikbaar is, biedt deze methode indien gecombineerd met de temperatuursensor een mogelijkheid om de

Samenvatting

verandering van de viscositeit door temperatuur te bepalen.

Nu de werking van het verwarmingssysteem bevestigd is, kan FtsH bestudeerd worden. De temperatuur werd gemeten aan de hand van de temperatuursensor, omdat de temperatuur waarbij FtsH actief is en het uitvallen van organische component dicht bij elkaar ligt. Ondanks dat het temperatuur bereik in acht genomen was, vond samen clustering van enzymen in de experimentele oplossing plaats. Om die reden werden deze enzymen niet langer gebruikt.

Aangezien de metingen geen succes opleverden, werden losse componenten van de studie getest. Dit bevestigde aanwezigheid en activiteit. Onverwachts toonde dit ook dat het aanhangsel wat wordt door FtsH gebruikt wordt om een substraat te herken zich covalent bindt aan FtsH. Dit zou een verklaring kunnen geven voor de beperkte tijd dat deze actief is.

Helaas is het in deze studie niet gelukt om ontvouwing en afbreking van het substraat door FtsH te meten. Hierdoor blijft het mechanisme onbekend. Toekomstige studies zullen moeten uitwijzen of de experimentele omstandigheden gunstig genoeg zijn om de mechanismes achter het ontvouwen en afbreken door FtsH te kunnen bepalen.

Chapter 1

Introduction

First principle: never to let one's self be beaten down by persons or by events - Marie Curie

1.1 FtsH, a protease of the AAA+ superfamily

1.1.1 The classical AAA clade of the AAA+ superfamily

A wide variety of processes in the cell depend on protein complexes (macromolecular machines) that can undergo conformational changes driven by the energy extracted from nucleotide hydrolysis (NTPase activity) [1]. The biological functions that they employ can be divided into three groups. There are transporting motor proteins, which do useful work for the cell by translocation; timing devices, which regulate the coupling and decoupling of different proteins; and recycling machines, which recycle misfolded and mistranslated proteins by proteolysis [1, 2].

These molecular machines play such important roles that they can be found in all life forms (archaea, bacteria, and eukaryotes). The machines that share conserved sequences and have structural and mechanistic similarities might have originated from a single common ancestor, the last universal common ancestor (LUCA). Grouping all (distantly) related proteins will reveal their evolution from a common ancestor throughout the evolution in different life forms.

This classification is termed with superfamilies, families, subfamilies, and clades, see fig. 1.1 for the representation of the AAA+ superfamily. A superfamily contains all distantly related proteins and is divided into different protein families. Each protein family consists of a group of proteins that can be traced back to a LUCA of all modern cellular life forms (archaea, bacteria, and eukaryotes). Within a protein family there can be subfamilies, which occur when a protein family has diversified within a cellular life form. Then the families encompassed in a superfamily can also be divided into (super)clades. A clade includes (multiple) protein families and subfamilies sharing a LUCA. Clades can be nested within one another as long as they share a LUCA, forming a nested hierarchy. A clade can therefore include many distantly related proteins or only small group of closely related proteins. A superclade consists of the clades that have diversified after the superfamily and before LUCA.

A superfamily that consists of molecular machines that can undergo conformational changes driven by nucleotide hydrolysis is the AAA+ superfamily. This family encompasses **A**TPases associated with diverse cellular activities (AAA+), which utilizes ATP hydrolysis to assist in assembly,

1.1 *FtsH*, a protease of the AAA+ superfamily

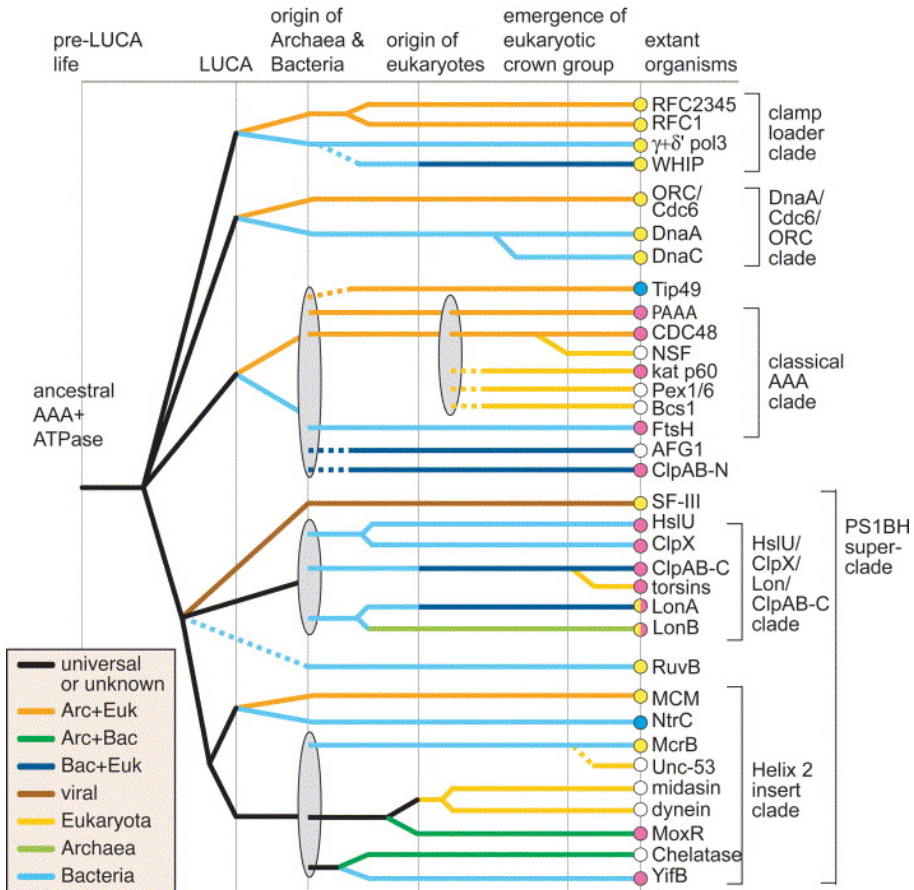


Figure 1.1: Schematic representations of the AAA+ superfamily divided into families, subfamilies, super clade, and a clade. Figure taken from [3].

1 Introduction

operation, or disassembly of protein complexes as a molecular chaperone [2, 3]. Evolutionary classification of proteins within this superfamily demonstrated multiple groups, clades, families and subfamilies [2–7]. The seven clades defining the AAA+ superfamily are the clamp loader clade, initiator clade, classical AAA clade, superfamily III helicase clade, HslU/-ClpAB/Ion/RuvB (HCLR) clade, H2 insert clade, and PS-II insert clade [7]. These clades slightly differ from the ones depicted in fig. 1.1 as the classification has recently been updated [7].

The focus of this thesis is on FtsH, which belongs to the classical AAA clade. Therefore, the AAA clade will be further investigated before we move on to the details of FtsH.

The classical AAA clade was originally defined as the AAA superfamily and contained all ATPases related to the proteasomal ATPases, FtsH, and CDC48 [3]. This clade encompasses such functionally diverse proteins that it has more recently been subdivided into two AAA+ protein categories: type I and type II (Puchades et al. [8]). The type I includes proteins with a single AAA+ domain, such as the proteasomal ATPases and FtsH, whereas type II includes proteins with a double AAA+ domain within its protein chain, such as CDC48.

Even though this clade consists of functionally diverse proteins, all the families contribute in processes related to protein unfolding and degradation [3, 7]. For instance, the 26S proteasome unfolds and degrades (aberrant) ubiquitylated substrates [8], FtsH unfolds and degrades aberrant membrane-anchored and cytoplasmic proteins [9, 10], and CDC48 mediates retro-translocation of misfolded or damaged ubiquitylated membrane and secretory proteins into the cytosol to be degraded by the proteasome [8]. They thus all regulate protein homeostasis of the cell, which is the major task the entire superfamily performs.

These three families share conserved sequences and have structural and mechanistic similarities. The majority of the proteins in the classical AAA clade consist of an oligomeric (generally hexameric) ring structure with a central pore to unfold and translocate substrates [2, 3, 6, 7]. With their presence in all three life forms, it is highly likely that they share a single LUCA. The proteasomal ATPases and CDC48 families are conserved throughout the archaea-eukaryotic branch and the FtsH family is conserved throughout the bacterial branch[3].

1.1.2 The discovery of FtsH and its essential function

The gene coding for FtsH in *E. coli* was independently discovered by four different groups, all designating it differently due to the difference in phenotype [11]. It was discovered as HflB (**H**igh frequency of lysogenization **B**), as it was found to degrade the transcriptional activator II (a key regulator of lysogenization); as FtsH (**F**ilamentation temperature sensitive mutant **H**), when they were searching for temperature sensitive mutants after chemical mutagenesis; as TolZ (colicin **t**olerant **Z**), when it showed tolerance to the protein antibiotics colicin, and as mrsC (**m**RNA stability **C**), when it was involved in degradation of bulk mRNA [11]. The designation FtsH will be used throughout this thesis, as it is the designation used by scientists nowadays.

The different designations already implied the ability of FtsH to degrade various proteins. Later research indeed demonstrated that FtsH degrades a wide variety of proteins, both cytosolic and membrane-anchored. It is, for instance, involved in regulating the phospholipid to lipopolysaccharide ratio in the outer membrane by degrading LpxC protein [12]; in avoiding the cell of going into a heat stress response by degrading the heat shock sigma factor at physiological temperatures [10]; and it degrades YfgM, a periplasmic chaperone and a negative regulator of RcsB, during an osmotic shock or during stress conditions related to stationary growth phase [10]. FtsH, thus, contributes to the cell's protein homeostasis and to bacterial stress responses, triggered by a change in temperature, pH, salts, oxidation, or nutrients.

The wide variety of protein substrates and the importance of FtsH to the vitality of the cell, makes it an attractive drug target. However, immobilization of FtsH could also be used to kill the cell, as it has, in most Gram-negative bacteria, an essential LpxC regulatory function [10]. It was indeed found that FtsH was involved in the antibiotic resistance of tobramycin in *Pseudomonas aeruginosa* [13]. Deletion of the *ftsH* gene led to a dramatic increase in sensitivity to the aminoglycoside antibiotic tobramycin. Thereby demonstrating its importance to the vitality of the cell and emphasizing the potentiality as a drug target or antibiotic enhancement.

Besides its importance in bacteria, mutations in the human ortholog of FtsH, m-AAA, has been found to cause hereditary spastic paraplegia. This

1 Introduction

is a neurodegenerative disorder in humans, causing progressive spastic paralysis in the lower limbs [14, 15]. The progressivity of this disease could be explained by accumulation of oxidatively damaged protein substrates over the years. However, the mechanisms causing this disease are not fully understood yet [14]. Therefore, mechanical studies of FtsH (mutations, and orthologs) is of medical and fundamental importance.

1.1.3 FtsH structure

FtsH has been found in many different bacteria, for instance, in *Escherichia coli* (*E. coli*), *Aquifex aeolicus* (*A. aeolicus*), and *Thermotoga maritima* (*T. maritima*) [11]. In *E. coli* it is one of the five energy driven proteases from the AAA+ superfamily (ClpXP, ClpAP, HslUV, FtsH and Lon) [16]. FtsH distinguishes itself from the other proteases, since it is the only one that belongs to a different clade, it is anchored to the membrane and it is the only essential protease in *E. coli* [10, 17].

Purifying (full-length) FtsH has been challenging, as it is non-soluble and anchored to the membrane. Structural and functional studies, therefore, predominantly focused on the cytosolic domain of FtsH, containing the ATPase and protease domain [15, 18–22]. FtsH is able to hexamerize without the transmembrane- and periplasmic domain. However, An et al. [17] argued that functionally the periplasmic domain is required, as it might be involved in recognition of misfolded membrane proteins.

All structural studies of the ATPase and protease domains of the FtsH hexamer demonstrated a sixfold symmetry [18–22]. These studies resolved the zinc-binding sequences, which stimulates proteolytic activity, and its narrow (~ 1.5 nm diameter [19]) central pore, in which the substrate gets degraded.

The ATPase domain, however, has shown to adopt a twofold- [19, 21], a threefold- [18, 22], and a sixfold symmetry [20]. The two- and threefold symmetry was observed for ADP bound tmFtsH (*T. maritima* FtsH) and aaFtsH (*A. aeolicus* FtsH) and the sixfold symmetry for *apo* bound tmFtsH [20]. Nonetheless, they did resolve the second region of homology (SRH) motif and the conserved FGV (phenylalanine, glycine, and valine) pore motif which are required for ATP hydrolysis and oligomerization, and substrate recognition and translocation, respectively [20].

The ATPase domain symmetry and mechanism to translocate a sub-

1.1 FtsH, a protease of the AAA+ superfamily

strate have not (yet) been resolved for FtsH. However, it has been resolved for the ATP- and substrate bound yeast homolog YME1 [23], showing no symmetry. In this homolog, four of the six ATP binding sites were bound with ATP, one was bound with ADP and one was empty (*apo*) adopting an asymmetric spiral staircase around the substrate. It was proposed that the substrate is translocated in a stepwise manner upon sequential ATP hydrolysis [23], see fig. 1.2.

Conformational changes were also observed for FtsH when the electron microscopy images of ADP and *apo* bound tmFtsH were compared [20]. The observed distance between the two states was more than 4.5 nm [20]. The occupancy of different conformational states were also seen for tmFtsH with single molecule Förster resonance energy transfer (smFRET) [15]. They found five different states when they analyzed the distances between the protease and ATPase domain, each state with a different affinity, in the absence of a substrate. These affinities were ATP dependent and showed the preference towards a more closed configuration when ATP was present.

Recently, the full-length FtsH structure, resolved by cryo-electron microscopy (cryo-EM) and negative stain electron microscopy (negative stain EM), became available [24–26]. The negative stain images of aaFtsH and the cryo-EM map of *E. coli* FtsH (ecFtsH) are shown in fig. 1.3. Interestingly, Carvalho et al. [24] and Liu et al. [25] both observed that the cytosolic domain of FtsH was tilted with respect to the transmembrane and periplasmic domains. This tilt was observed for *Aquifex aeolicus* FtsH (aaFtsH) in detergent micelles and in the presence of ATP [24], and for *Thermotoga maritima* FtsH (tmFtsH) in lipid nanodiscs and the absence of ATP and ADP, yet still bound to ADP [25]. This tilt, possibly, promotes substrate recognition and entry. However, Qiao et al. [26] did not observe this tilt for ecFtsH in detergent micelles and the presence of non-hydrolysable ATP, presumably due to the chemical cross-linking of the cytosolic domain to achieve more rigidity for a higher resolution structure.

The full-length images also contribute to the discrepancy in symmetry. When Liu et al. [25] studied full-length ADP bound tmFtsH, with a mutation prohibiting binding of zinc and thereby abolishing proteolytic activity, a sixfold symmetry was observed. They argued that the observed two- and threefold symmetry of ADP bound FtsH [18, 19, 21, 22] may have been

1 Introduction

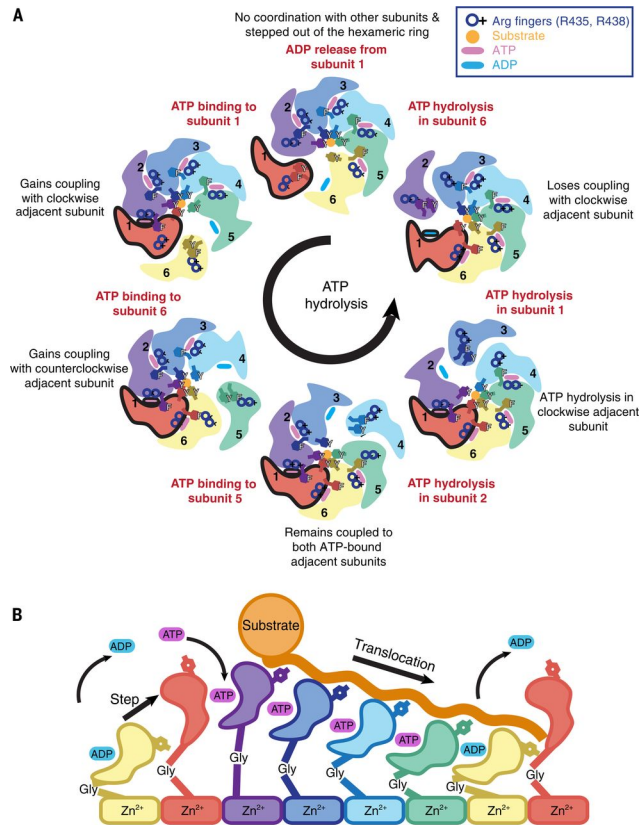


Figure 1.2: **Proposed substrate translocation of the yeast FtsH homolog YME1.** a) Cartoon representation of the proposed ATP binding and hydrolysis cycle of the YME1 ATPase domain. The ATPase domain has six ATPase domains, with four subunits bound to ATP, one to ADP and one empty. The hydrolysis steps are indicated for the black encircled subunit 1 in a counterclockwise manner. The substrate is depicted in orange, and ATP and ADP in pink and blue respectively. b) Cartoon representation of substrate-subunit interaction through the aromatic tyrosine for a full hydrolysis cycle. The yellow and red (ADP and *apo*) subunits shown twice to highlight the complete cycle. Figure taken from [23].

1.1 *FtsH*, a protease of the AAA+ superfamily

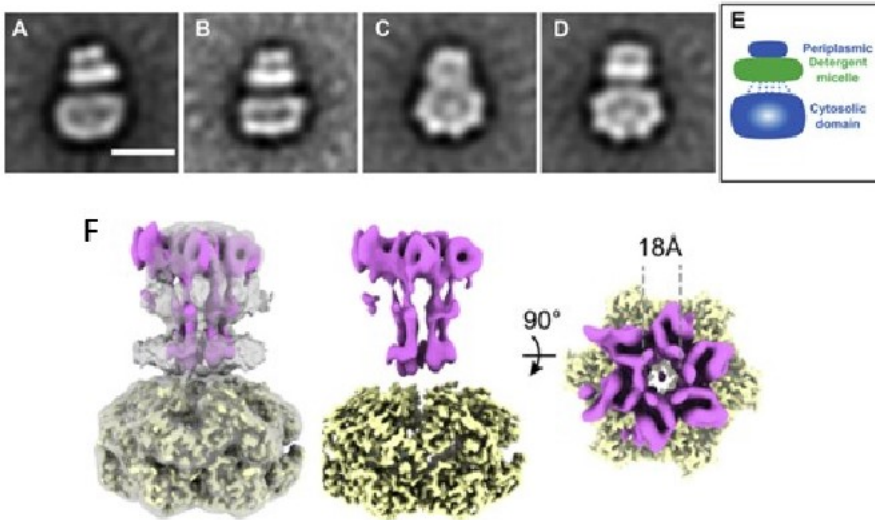


Figure 1.3: **Full length structure of FtsH.** a-d) Side and tilted views of negatively stained *Aquifex aeolicus* FtsH (AaFtsH) hexamers. The scale bar represents 11 nm. e) Schematic representation of AaFtsH with the periplasmic and cytosolic domain in blue, the blue dashed lines indicating six linking peptides present in the protein sequence, and the (lauryl maltose neopentyl glycol) LMNG-micelle wrapping around the transmembrane domain in green. f) A side and top view of the cytoplasmic domain map of *Escherichia coli* FtsH in yellow and the periplasmic and transmembrane domain map in violet. The maps are fitted into the full length FtsH hexamer in gray. Figure A-E taken from [24] and figure F from [26].

1 Introduction

the result of the absence of the transmembrane- and periplasmic domain. This absence caused FtsH to be monomeric in solution and only upon crystallization became hexameric, this might have induced intermolecular packing and lattice contacts causing the symmetries observed. Carvalho et al. [24] imaged full-length, ATP bound, non-mutated, aaFtsH in detergent micelles and observed asymmetry in the ATPase domain, which shared the asymmetry found by Puchades et al. [23].

The spiral staircase mechanism observed for YME1 [23] fitted the low resolution aaFtsH asymmetry of Carvalho et al. [24] and was also proposed by Liu et al. [25] when they observed a sixfold ADP symmetry for tmFtsH. This stepwise translocation, has been verified for other proteases, such as ClpXP [27–31] and ClpAP [29, 31] (reviewed in [32, 33]) by dual-beam optical tweezers section 4.2.4. However, this is still not conclusive for FtsH, a functional study showed cooperative ATP hydrolysis events where four to five hydrolysis events were coupled [34], rather than the single or double steps (hydrolysis events) observed for ClpXP [28] and ClpAP [29].

1.1.4 Unfoldase activity of FtsH

FtsH degrades aberrant and excessive membrane and cytosolic proteins to avoid lethal accumulation in the cell. To degrade, it first needs to unfold the protein. When a protease has the ability to unfold strongly folded proteins, it has a high unfoldase activity. This activity has been a major point of discussion for FtsH. The argumentation for weak unfoldase activity was found two decades ago when Herman et al. [35] discovered that FtsH, unlike ClpXP and ClpAP, was unable to degrade stable substrate proteins *in vivo* and *in vitro*, such as ssrA-tagged dihydrofolate reductase (ssrA-DHFR). They proposed that FtsH requires a low to moderate thermostability or an altered protein folding state of substrate proteins in order to be able to degrade them.

It should be denoted that experimental procedures affect proteolytic activity. Substrate degradation is, for example, dependent on the (length of the) substrate tag [9, 34, 36] and on directionality (N- to C-terminal or C- to N-terminal degradation) [34, 36], but also ATP concentration [34] and substrate concentration [36] play a role. Besides that, mutations and solubilization for *in vitro* experiments of FtsH can affect activity [17, 21, 37, 38] and the in- or exclusion of the HflKC-FtsH complex in a study, as this

1.1 FtsH, a protease of the AAA+ superfamily

complex promotes degradation of cytoplasmic substrates while preventing degradation of normal functional membrane proteins [26].

In contrast with the finding of Herman et al. [35], Morehouse et al. [36] showed that detergent-solubilized FtsH can degrade ssrA-DHFR *in vitro*. Even more interestingly, they showed that degradation occurred for DHFR with an ssrA-tag, an 8 to 49-residue linker plus an ssrA-tag, and also without an ssrA-tag [36]. More evidence of a “not so weak” unfoldase activity has been obtained. FtsH demonstrated to degrade the transmembrane protein ProW₁₋₁₈₂ with two consecutive tags (ProW₁₋₁₈₂-FLAG-ssrA) *in vivo* [39], the membrane associated cyclopropane fatty acid synthase (CFA synthase) *in vivo* and *in vitro* [40], and the highly thermostable membrane protein GlpG *in vivo* [41]. Especially, for the extraction of GlpG from the membrane, FtsH needs to overcome a large energy barrier.

When Yang et al. [34] found that FtsH could degrade GlpG, they continued by looking into the ATP hydrolysis and degradation rate of FtsH. It was found that the maximal degradation rate depends on conformational stability of the substrate rather than ATP hydrolysis rate. Therefore, indicating that a different mechanism is rate limiting. Unfolding or membrane dislocation are evident rate limiting mechanisms, but were ruled out as rate limiting step, because the rate limited degradation was also observed for degradation of casein (weakly folded and not membrane bound). They suspected that the protease domain was not fully functional in their reconstituted system, possibly causing the rate limiting step. The unfoldase activity of FtsH, thus, remains ambiguous.

To investigate whether FtsH translocates substrates in a step wise manner and to test the translocation pulling power, degradation of mutated titin’s module I27 by the full-length FtsH from the thermophilic bacterium *A. aeolicus* in detergent micelles at a temperature of 53-60 °C will be studied here with optical tweezers.

1 Introduction

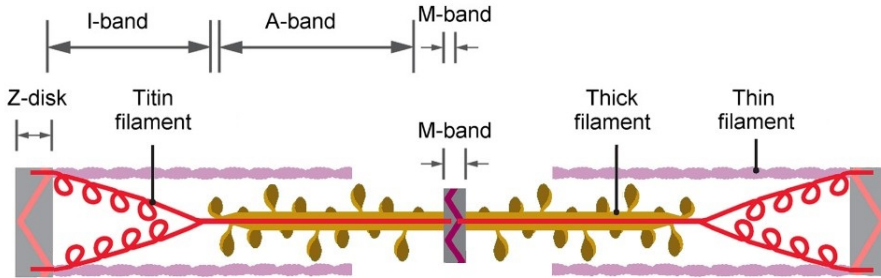


Figure 1.4: **Schematic representation of a titin filament within the sarcomere.** Figure is modified from [45].

1.2 I27 a module of the muscle protein titin, a model substrate for AAA+ proteases

1.2.1 The extensible muscle protein titin

The giant modular protein titin can be found in vertebrate muscles and is believed to function as a molecular spring responsible for the passive elasticity of muscles [42–44]. A single titin molecule is longer than $1\ \mu\text{m}$ and spans half the sarcomere connecting the Z-disk to the M-band, as shown in fig. 1.4. Along its length, it has different domains (the I-band, the A-band and the M-band (or M-line)) and each domain a different property (elastic domain, a stiff and thick domain, and an integral part of a protein meshwork, respectively).

These properties can be explained by the composition of the domains and interaction with other proteins. The domains consist of combinations of fibronectin type III (Fn3) modules, immunoglobulin-like (Ig-like) modules, and one (or multiple) nonrepetitive linker sequence(s). The M-band domain of titin consists of (relatively) stable Ig-like modules separated by nonrepetitive linker sequences and serves as a rigid anchoring plane for the thick filament [42, 43]. The A-band domain contains Fn3 and Ig-like modules, which alternate, such that Ig-like modules are always flanked by Fn3 modules. The single modules of this band have, *in vitro*, the lowest thermal and chemical stability [42]. However, it is expected that *in vivo*

1.2 I27 a module of the muscle protein titin

the band will be stabilized by other protein interactions (myosin and C-protein) making it a stiff and thick domain [42, 43]. The I-band domain consists of a nonrepetitive linker sequence and Ig-like modules with differing (thermal and chemical) stabilities, and acts as an elastic connection between the thick filaments and the Z-disc [42, 43].

When single titin molecules were stretched, the elastic I-band domain was found to lengthen [44]. This band consists of up to ~ 100 Ig-like modules, no Fn3 modules, and one large PEVK-segment (a proline, glutamic acid, valine, and lysine rich segment) [45]. When only the I-band was subject to stretching experiments, it was observed that, during physiological stretch, especially the PEVK-segment contributes to the lengthening of the I-band domain [44, 46, 47], see fig. 1.5 for a schematic representation of titin stretching. Nonetheless, Rivas-Pardo et al. [48] also observed proximal (close to z-disk) Ig-like module unfolding at physiological relevant forces of 6-8 pN. At higher force ($F > 15$ pN), Kellermayer et al. [46] and Tskhovrebova et al. [47] observed unfolding of Fn3 and Ig-like modules. Interestingly, they all reported that refolding would only occur at forces much lower than the unfolding forces (2.5-5 pN). Complete refolding of the entire titin molecule was not observed by Kellermayer et al. [46] and Tskhovrebova et al. [47], but complete refolding of a constructed polypeptide consisting of eight repeats of an Ig-like module was observed by Rivas-Pardo et al. [48]. It remains obscure whether module unfolding is physiological [45].

1.2.2 The structure of titin module I27 and some point mutations

A module of the I-band that has been extensively studied and is a model substrate for proteases, is module I27. This module consists of 89 amino acids with eight β -strands (A, A', B, C, D, E, F, and G) forming two, against each other packed, β sheets [43], see fig. 1.6a. Except for the A and A' β -strands, all adjacent strands are antiparallel. The surface of I27 is predominately covered with hydrophilic residues, whereas the hydrophobic side chains are well packed within its core. Another amino acid which is also part of the (hydrophobic) core of I27 is a unique tryptophan [43], which is well buried and conserved in all Ig-like modules of titin [42].

1 Introduction

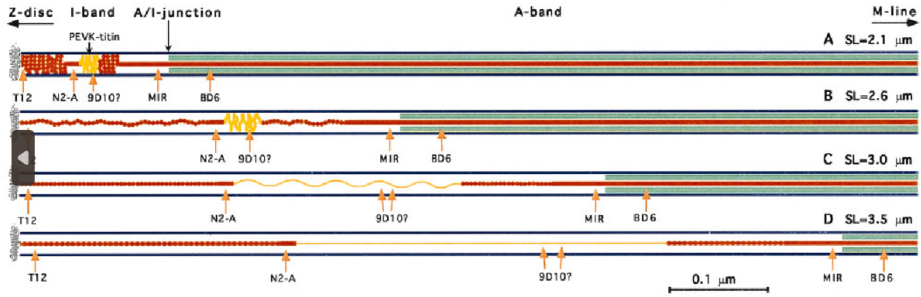


Figure 1.5: **Schematic representation of stretching soleus and psoas myofibrils.** A, the myofibril is in slack with the type II modules and PEVK-segment folded. B, a small stretch is applied causing the type II modules to straighten, while the PEVK-segment remains folded. C, a moderate stretch is applied causing the PEVK-segment to unravel, while the type II modules remain folded. And D, at high (but still physiological) stretch the PEVK-segment is stretched and the type II modules are highly strained. Figure is taken from [44].

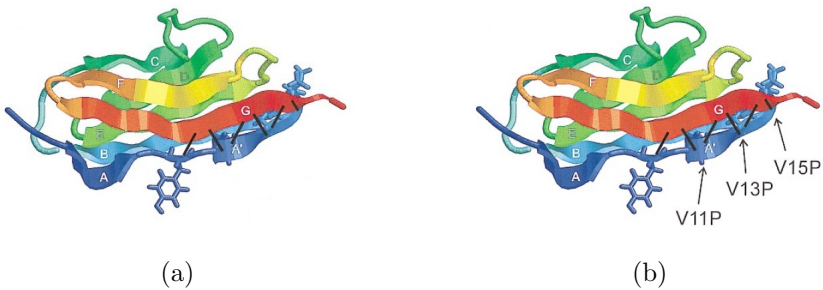


Figure 1.6: **A cartoon representation of the β -sandwich structure of the titin module I27.** a) The black lines, linking the A' and G β strands, represent backbone hydrogen bonds between the two strands. b) Position of the valine to proline mutations on the A' β strands, disrupting the hydrogen bonds between the A' and G β strands. Figure is modified from [49].

1.2.3 Mechanical stability of titin I27

The unfolding behavior of the (mutated) I27 module has been studied extensively by atomic-force microscopy (AFM) [49–51], infrared absorption [52], fluorescence emission spectra [42, 50, 52], far ultraviolet circular dichroism [42], nuclear magnetic resonance (NMR) [42], and magnetic tweezers [53–55]. These studies done with varies techniques followed different procedures in turns of temperature, applied forces, applied loading rates, and point mutations for the I27 domain.

Since protein degradation by FtsH will be studied at temperatures far above room temperature (53-60 °C), the thermal stability of titin I27 is important. The melting temperature (when half of the proteins are denatured) of I27 at neutral pH, atmospheric pressure, and low ionic solution was found to be ~ 73 °C [42]. A decrease in pH did not result in a significant change of melting temperature, but an increase in ionic strength (10 to 200 mM phosphate) caused a decrease in melting temperature (~ 73 °C to ~ 59 °C, respectively). A different study also observed a state in which the tertiary structure of I27 is loosened before it melted [52]. However, it should be noted that the ionic strength of their buffer was really high (1250 mM). Possibly inducing the loosened state at 50 °C and the lower melting temperature of 65 °C.

A partially unfolded state (intermediate state) of I27 has also been found by AFM studies [49–51]. The presence or absence of this intermediate state affects the extension upon (partially) unfolding and is therefore of importance. Williams et al. [56] argued that this intermediate state is only populated at forces higher than 100 pN, which is the case for AFM studies. Magnetic tweezers, on the other hand, can study the low force regime of I27 unfolding. However, due to the limited spatial temporal resolution an intermediate state could not be observed [53]. Nonetheless, the unfolding rates of (mutated) I27 at constant, low forces ($F < 100$ pN) do indicate a non-monotonic force-dependent unfolding [54, 55]. The decrease in unfolding rate, which occurred from 0 to 22 pN, was explained by a catch-bond behavior (upon increasing force, unfolding is less likely to occur) and the increase in unfolding rate, which occurred from 22 to 100 pN by a slip-bond-like behavior (upon increasing force, unfolding is more likely to occur). The switching force, when the catch-bond behavior switches to slip-bond-like behavior, was found to be 22 pN at 21 °C. This

1 Introduction

switching force will increase upon increasing temperature [54, 55].

The expected force dependent extension upon unfolding of the I27 domain is $x = x_t - x_{WLC}$; where x_t is the change in length from the folded to the transition state depending on force, which is determined by [54]:

$$x_t(F) = x_f(F) + \delta \coth\left(\frac{F\delta}{k_B T}\right) - \frac{k_B T}{F} \quad (1.1)$$

$$F_{WLC} = \frac{k_B T}{L_p} \left(\frac{1}{4(1 - x/L_c)^2} - \frac{1}{4} + \frac{x}{L_c} \right) \quad (1.2)$$

and $x_f(F)$ is the distance between the N- and C-termini of native I27 as determined by the worm-like chain model (WLC model, x in eq. (1.2)), F is the force in pN, δ the length between the 14th residue and the C-terminus ($\delta = 0.64$ nm [54]), k_B is the Boltzmann constant in pN*nm/K, T is the temperature in Kelvin, L_p is the persistence length of I27 ($L_p = 0.8$ nm [57]), and L_c is the contour length of the intermediate state of I27 ($L_c = 4.94$ nm [54]). The change in length from the transition state to the unfolded state x_{WLC} is determined by eq. (1.2), with x being x_{WLC} , the persistence length $L_p = 0.8$ nm, and the theoretical contour length of I27 $L_c \approx 33$ nm (89 aa x 0.38 nm) [50].

The force-extension dependency of I27 has also been studied at elevated temperatures [51, 55]. In these studies, a stretch was applied to a chain of multiple I27 modules that were connected through a short flexible linker at a constant temperature. Single unfolding and refolding events could be observed. The critical force was defined as the force at which folding and refolding were equally probable. The computed critical forces for mutated I27 (cysteines 47 and 63 were mutated to alanines, which possibly destabilized the protein) were between 3 and 5 pN for temperatures of 21 °C to 37 °C [53, 55]. A reduction in the force required to unfold mutated I27 (cysteines 47 and 63 were mutated to serines) due to an increase in temperature was also observed by Taniguchi et al. [51]. However, their force range was over 20-fold larger than the critical force found by Yu et al. [55]. The link used between the individual I27 modules should be taken into account as well, because this could affect the required force to unfold [58].

Besides temperature, point mutations in the β -strand A' of I27 have demonstrated to reduce mechanical stability [49]. More specifically, mutating valine 11, 13, or 15 of the β -strand A' to proline disrupts a specific

backbone hydrogen bond between the β -strands A' and G, see fig. 1.6b. These single mutations (hereafter I27^{V11P}, I27^{V13P}, and I27^{V15P}) lowered the unfolding force of the I27 module, and likely also decreases the melting temperature.

The point mutations I27^{V13P} and I27^{V15P} will be used here to study protein unfolding and translocation by FtsH, a possibly weak unfoldase, FtsH at a temperature between 53 and 60 °C.

1.3 Optical tweezers

1.3.1 Optical tweezers

Optical tweezers are highly suitable to study a wide variety of biological phenomena, such as motor proteins [27, 59], unfolding and refolding of proteins [46], flagella [60, 61] and lipid bilayers [62]. A dielectric micrometer sized particle is trapped in a highly focused laser beam [63, 64], the trap laser. The position of the trapped bead can be determined with a camera or with a second highly focused laser beam, the detection laser. The focus of the detection beam has to align with the trap laser, but the detection beam is much weaker and has a different wave length to minimize interference. The deflections of the detection light can then be measured with a position sensitive detector and converted into bead position.

Even though a bead is trapped, it is still subject to external forces that push the bead away from the trap center. This external force can be small, when water molecules bump unto the bead, or much larger, if an external flow is applied. For small displacements, the bead feels an attractive force towards the center of the trap. This force increases linearly with the displacement of the bead and the trap acts as a Hookean spring ($F = -\kappa * x$) with F the force applied to the bead, x the distance of the bead to the trap center and κ the stiffness of the trap [65]. When displacements are much larger, this attractive force does no longer linearly increase with displacement, but will plateau off. And for even larger displacements, the bead will experience a repulsive force and will eventually escape from the trap [66].

The forces pulling the bead towards the center of the trap are due to the reflection and refraction of laser light, see fig. 1.7a. The reflected light

1 Introduction

rays cause a change in momentum. The conservation of linear momentum then dictates that the bead experiences an equal but opposite change in momentum, causing the bead to move downwards (fig. 1.7b). However, an upwards reactive force is induced by the refracted light rays that are deflected forward, see fig. 1.7b. This occurs when the bead has a higher refractive index than the surrounding medium. When the bead moves laterally out of the trap (along the x- and y-axis in fig. 1.7c), the bead experiences an attracting force towards the center due to the Gaussian intensity profile of the trap laser. The higher laser intensity at the center induces a larger force than the lower laser intensity away from the center, see fig. 1.7c. Hence, the bead experiences an attractive force towards the trap center. The bead is stably trapped if the forces are balanced [65, 67].

To study biological phenomenon with optical tweezers the molecule of interest is generally linked to a bead. Different types of coated beads that can form strong bonds and are commercially available can be used to establish such a link. For instance, streptavidin coated beads can bind to biotin, which could itself be covalently linked to the molecule of interest and is unlikely to disturb the biological behavior due to its small size. When the streptavidin beads and the biotinylated molecules are mixed, they will spontaneously bind. For stretching or folding-unfolding experiments, the other end of the molecule can be linked to the glass surface or a second bead through a different bond (for example an antibody-antigen pair). Two bead assays can be performed either with a single-trap and a micropipette holding the bead by suction or with a dual-trap [67].

The advantage of a two bead two trap assay is that it enables a passive force clamp, which maintains a constant force (within $< 5\%$ change) for small displacements (~ 50 nm) [66]. To obtain this passive force region, a force-displacement curve of the trap has to be determined. This should be done by trapping bead 1 in trap 1 (T1) and bead 2 in trap 2 (T2) while the beads are linked through a tether, double-stranded DNA for example, see fig. 1.8a. T2 should be roughly three times stiffer than T1 to ensure that the bead in T2 remains within the linear force region of the trap while bead 1 is being pulled out of the trap. This can be achieved by moving one of the traps in a step wise manner away from the other trap while measuring the position of the beads at each step. The displacement of the bead with respect to the trap center can be determined at each trap. With

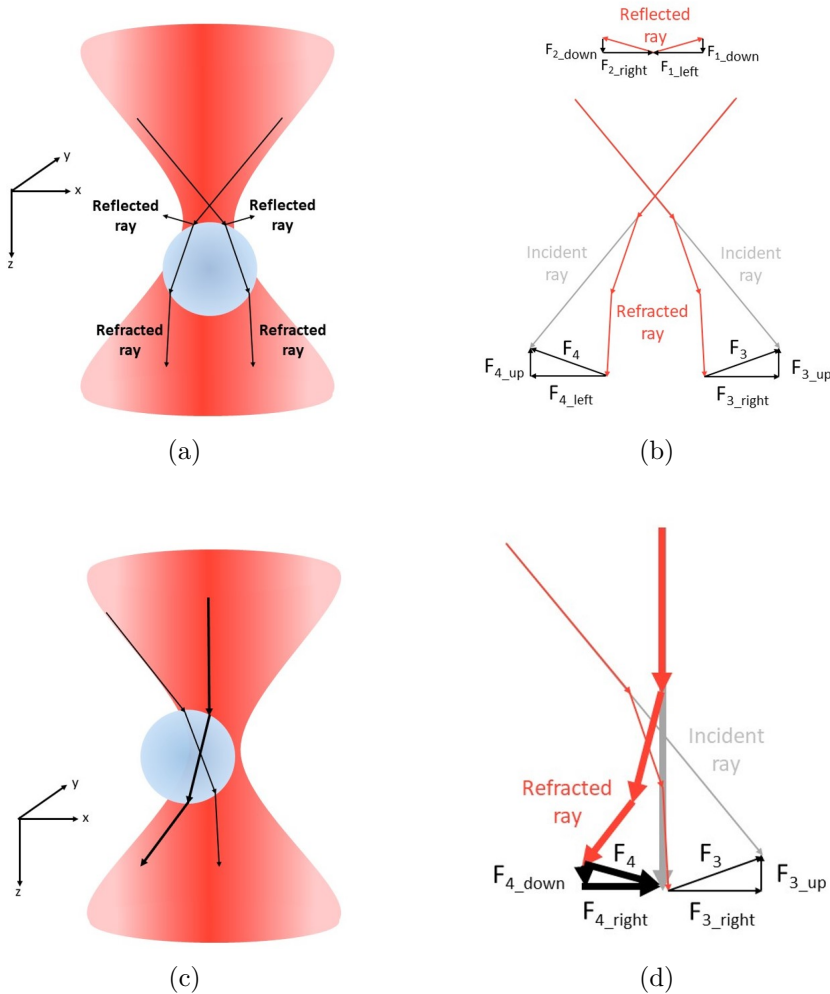


Figure 1.7: **Light refraction and reflection on a trapped bead.** a) Schematic representation of an optically trapped bead and the reflected and refracted light rays. b) The force balancing of the reflected rays F_{1_down} , F_{1_right} , F_{2_down} , and F_{2_left} and of the refracted rays F_{3_up} , F_{3_right} , F_{4_up} , and F_{4_left} . c) A schematic representation of a bead laterally moved out of the trap (-x direction). d) The force balancing of a bead moved leftwards from the trap center. A thicker arrow representing a higher light intensity inducing a larger force.

1 Introduction

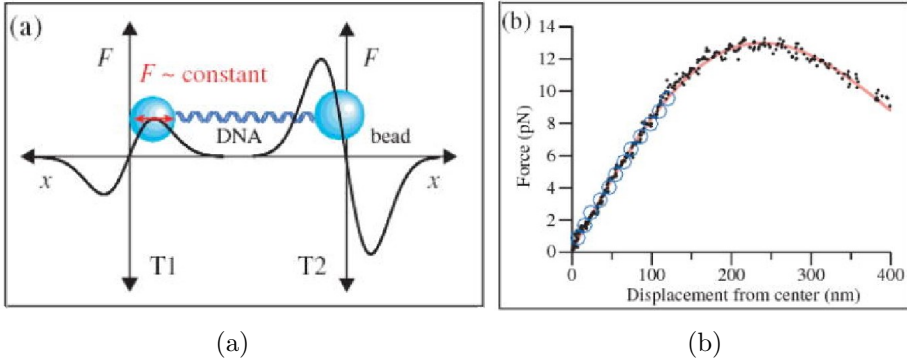


Figure 1.8: **Experimentally determining the attractive force felt by a bead displacing from the trap center.** a) The experimental setup to determine the geometry of trap T1. Two beads are trapped and linked through double stranded DNA. Trap T2 is roughly three times stiffer than T1, such that the bead trapped in T2 stays within the linear force-displacement region of the trap (as indicated by the black curve) while the bead in T1 is pulled out of the trap. The attractive force (towards the center of the trap) felt by both beads is determined by the stiffness of T2 and the bead-to-trap center distance. Concurrently, the bead-to-trap center of the bead in T1 is determined. In b) the force-displacement curve of T1 is shown with the force determined by T2 and the (bead) displacement from the center by T1. Figure is modified from [66].

the displacement and the stiffness of the stiffer trap (T2), the force felt by both beads can be determined. At the same time, the displacement of the bead in the weaker trap (T1) is used to get the displacement (fig. 1.8b) [66]. The constant force region is valuable, especially for force dependent phenomena, such as hairpin unfolding [66]. The construction of a dual trap optical tweezers and the obtained passive force clamp region will be discussed in chapter 2.

1.3.2 Heating an optical tweezers sample

Many of the above described phenomena were studied at room temperature even though this is below their physiological temperature. In optical tweezers, it is substantially more convenient to measure at room temperature due to practical considerations: the sample must be transparent to near infrared light; the optics and objective are affected by temperature changes; the objective, sample, and condenser are tightly packed; and optical tweezers measurements are highly sensitive to vibrations and air flows which might arise due to heating system or the heat itself.

Nonetheless, it is of great significance to study the sample at physiological temperature as it might significantly change the behavior of the studied phenomenon. Examples, relevant for this thesis, include the finding of Yu et al. [55] who found that unfolding rate of the protein domain I27 from titin, at physiological forces, increased roughly a 100-fold when the temperature was increased from 23 to 37 °C; in a double-stranded DNA (dsDNA) overstretching experiment, Mao et al. [68] observed that at temperatures below 21 °C the overstretching transitions were smooth and reversible, but for temperatures above 33 °C fragments of the dsDNA start to melt [68]; and the activity of the AAA+ protease ClpXP significantly increased when the temperature was increased from 15 °C to 37 °C [28].

We therefore designed and tested a newly developed heating system for optical tweezers, see chapter 3 for more details. This system locally heats the solution under study, from above and below to ensure uniform heating. The heating system consists of two parts: a glass slide with a conductive layer and a conductive wire twisted around and mounted on the objective. They are both based on Joule heating [69]. This is a process in which an electrical current runs through a conductor and produces heat by $P = I^2R$, with P the heating power in Watt, I the current in Ampère and R the resistance in Ohm. To ensure that no current leaks into the sample solution, the conductive layer on the glass slide is shielded from the solution by another thin glass slide glued to it.

A gradient free temperature increase along the height (z-axis) of the sample can be ensured by equally heating from above and from below. A possible gradient along the other directions, x- and y-axis, were diminished by reducing the dimensions of the sample under study such that they fall

1 Introduction

within the surface of the heating systems, especially the one of the objective. With our design equal heating can be guaranteed up to 40 °C, after that the temperature can be further increased with the heating system above the sample. The effect of this heat difference has been investigated and is reported in chapter 3.

1.4 This thesis

Throughout this thesis, I will describe my path towards the optical tweezers study of the protease FtsH. The first step, described in chapter 2, was to build and program a dual beam optical tweezers. While building the new setup, the passive force clamp region on the existing setup was determined.

When the new setup was build an objective heating system, as described in chapter 3, was mounted on it. The heating system is required to study the purified full-length FtsH found in the thermophilic bacterium *Aquifex aeolicus* (aaFtsH) [24]. This bacterium was first found in the outflow of a hot spring in Yellowstone national park and grows best between 85 and 95 °C. After an activity assay at varying experimental temperatures, it was found that aaFtsH was active at temperatures above ~ 53 °C (chapter 4).

As described in chapter 3, the heating system was complemented by a flow cell with a commercially available microscope slide enhanced with a thin conductive layer of indium tin oxide (ITO). The temperature was measured by a thin thermocouple placed within the flow cell and by our novel method that locally computes the temperature from bead recordings. The method was tested by obtaining the laser-induced heating in our trap. This resulted in an increase comparable to theory for a non-conductive flow cell. The ITO flow cell demonstrated a much larger laser-induced effect, which can be attributed to laser absorption by the ITO layer. The absorption was minimized by utilizing a low laser power.

With the objective and ITO flow cell heating a temperature of ~ 70 °C was achieved. The temperature increase computed by our method and the thermocouple gave a similar temperature increase. However, the temperature computed by our method at room temperature was typically higher, this was expected as our method measures the temperature locally around the trap and would here fore also be sensitive to laser-induced heating.

Our heating system was then used to study aaFtsH at temperatures between 53 and 60 °C (chapter 4). The high temperature caused the formation of large aggregates and caused the exclusion of the oxygen-scavenging and ATP regeneration system. Establishing a link between the substrate and aaFtsH during the optical tweezers experiment was rare. The individual components, such as substrate and aaFtsH, has been tested and their presence or activity confirmed. A few recordings have been obtained, but unfortunately none of these recordings was suitable to determine the mechanical activity of aaFtsH.

References

- (1) Alberts, B.; Miake-Lye, R. Unscrambling the puzzle of biological machines: The importance of the details. *Cell* **1992**, *68*, 415–420.
- (2) Neuwald, A. F.; Aravind, L.; Spouge, J. L.; Koonin, E. V. AAA+: A Class of Chaperone-Like ATPases Associated with the Assembly, Operation, and Disassembly of Protein Complexes. *Genome Research* **1999**, *9*, 27–43.
- (3) Iyer, L. M.; Leipe, D. D.; Koonin, E. V.; Aravind, L. Evolutionary history and higher order classification of AAA+ ATPases. *Journal of Structural Biology* **2004**, *146*, 11–31.
- (4) Erzberger, J. P.; Berger, J. M. Evolutionary Relationships and Structural Mechanisms of AAA+ Proteins. *Annual Review of Biophysics and Biomolecular Structure* **2006**, *35*, 93–114.
- (5) Ammelburg, M.; Frickey, T.; Lupas, A. N. Classification of AAA+ proteins. *Journal of Structural Biology* **2006**, *156*, 2–11.
- (6) Snider, J.; Thibault, G.; Houry, W. A. The AAA+ superfamily of functionally diverse proteins. *Genome Biology* **2008**, *9*, 216.
- (7) Khan, Y. A.; White, K. I.; Brunger, A. T. The AAA+ superfamily: a review of the structural and mechanistic principles of these molecular machines. *Critical Reviews in Biochemistry and Molecular Biology* **2021**, *57*, 156–187.
- (8) Puchades, C.; Sandate, C. R.; Lander, G. C. The molecular principles governing the activity and functional diversity of AAA+ proteins. *Nature Reviews Molecular Cell Biology* **2020**, *21*, 43–58.
- (9) Chiba, S.; Akiyama, Y.; Ito, K. Membrane Protein Degradation by FtsH Can Be Initiated from Either End. *Journal of Bacteriology* **2002**, *184*, 4775–4782.
- (10) Bittner, L.-M.; Arends, J.; Narberhaus, F. When, how and why? Regulated proteolysis by the essential FtsH protease in *Escherichia coli*. *Biological Chemistry* **2017**, *398*, 625–635.
- (11) Schumann, W. FtsH - a single-chain charonin? *FEMS Microbiology Reviews* **1999**, *23*, 1–11.

- (12) Schäkermann, M.; Langklotz, S.; Narberhaus, F. FtsH-Mediated Coordination of Lipopolysaccharide Biosynthesis in *Escherichia coli* Correlates with the Growth Rate and the Alarmone (p)ppGpp. *Journal of Bacteriology* **2013**, *195*, 1912–1919.
- (13) Hinz, A.; Lee, S.; Jacoby, K.; Manoil, C. Membrane Proteases and Aminoglycoside Antibiotic Resistance. *Journal of Bacteriology* **2011**, *193*, 4790–4797.
- (14) Nolden, M.; Ehses, S.; Koppen, M.; Bernacchia, A.; Rugarli, E. I.; Langer, T. The m-AAA Protease Defective in Hereditary Spastic Paraplegia Controls Ribosome Assembly in Mitochondria. *Cell* **2005**, *123*, 277–289.
- (15) Ruer, M.; Krainer, G.; Gröger, P.; Schlierf, M. ATPase and Protease Domain Movements in the Bacterial AAA+ Protease FtsH Are Driven by Thermal Fluctuations. *Journal of Molecular Biology* **2018**, *430*, 4592–4602.
- (16) Hanson, P. I.; Whiteheart, S. W. AAA+ proteins: have engine, will work. *Nature Reviews Molecular Cell Biology* **2005**, *6*, 519–529.
- (17) An, J. Y.; Sharif, H.; Kang, G. B.; Park, K. J.; Lee, J.-G.; Lee, S.; Jin, M. S.; Song, J.-J.; Wang, J.; Eom, S. H. Structural insights into the oligomerization of FtsH periplasmic domain from *Thermotoga maritima*. *Biochemical and Biophysical Research Communications* **2018**, *495*, 1201–1207.
- (18) Suno, R.; Niwa, H.; Tsuchiya, D.; Zhang, X.; Yoshida, M.; Morikawa, K. Structure of the Whole Cytosolic Region of ATP-Dependent Protease FtsH. *Molecular Cell* **2006**, *22*, 575–585.
- (19) Bieniossek, C.; Schalch, T.; Bumann, M.; Meister, M.; Meier, R.; Baumann, U. The molecular architecture of the metalloprotease FtsH. *Proceedings of the National Academy of Sciences* **2006**, *103*, 3066–3071.
- (20) Bieniossek, C.; Niederhauser, B.; Baumann, U. M. The crystal structure of *apo*-FtsH reveals domain movements necessary for substrate unfolding and translocation. *Proceedings of the National Academy of Sciences* **2009**, *106*, 21579–21584.

1 Introduction

- (21) Vostrukhina, M.; Popov, A.; Brunstein, E.; Lanz, M. A.; Baumgartner, R.; Bieniossek, C.; Schacherl, M.; Baumann, U. The structure of *Aquifex aeolicus* FtsH in the ADP-bound state reveals a C2-symmetric hexamer. *Acta Crystallographica Section D Biological Crystallography* **2015**, *71*, 1307–1318.
- (22) Uthoff, M.; Baumann, U. Conformational flexibility of pore loop-1 gives insights into substrate translocation by the AAA+ protease FtsH. *Journal of Structural Biology* **2018**, *204*, 199–206.
- (23) Puchades, C.; Rampello, A. J.; Shin, M.; Giuliano, C. J.; Wiseman, R. L.; Glynn, S. E.; Lander, G. C. Structure of the mitochondrial inner membrane AAA+ protease YME1 gives insight into substrate processing. *Science* **2017**, *358*, DOI: 10.1126/science.aao0464.
- (24) Carvalho, V.; Prabudiansyah, I.; Kovacik, L.; Chami, M.; Kieffer, R.; van der Valk, R.; de Lange, N.; Engel, A.; Aubin-Tam, M.-E. The cytoplasmic domain of the AAA+ protease FtsH is tilted with respect to the membrane to facilitate substrate entry. *Journal of Biological Chemistry* **2021**, *296*, 100029.
- (25) Liu, W.; Schoonen, M.; Wang, T.; McSweeney, S.; Liu, Q. Cryo-EM structure of transmembrane AAA+ protease FtsH in the ADP state. *Communications Biology* **2022**, *5*, DOI: 10.1038/s42003-022-03213-2.
- (26) Qiao, Z.; Yokoyama, T.; Yan, X.-F.; Beh, I. T.; Shi, J.; Basak, S.; Akiyama, Y.; Gao, Y.-G. Cryo-EM structure of the entire FtsH-HflKC AAA protease complex. *Cell Reports* **2022**, *39*, 110890.
- (27) Aubin-Tam, M.-E.; Olivares, A. O.; Sauer, R. T.; Baker, T. A.; Lang, M. J. Single-Molecule Protein Unfolding and Translocation by an ATP-Fueled Proteolytic Machine. *Cell* **2011**, *145*, 257–267.
- (28) Cordova, J. C.; Olivares, A. O.; Shin, Y.; Stinson, B. M.; Calmat, S.; Schmitz, K. R.; Aubin-Tam, M.-E.; Baker, T. A.; Lang, M. J.; Sauer, R. T. Stochastic but Highly Coordinated Protein Unfolding and Translocation by the ClpXP Proteolytic Machine. *Cell* **2014**, *158*, 647–658.

- (29) Olivares, A. O.; Nager, A. R.; Iosefson, O.; Sauer, R. T.; Baker, T. A. Mechanochemical basis of protein degradation by a double-ring AAA+ machine. *Nature Structural; Molecular Biology* **2014**, *21*, 871–875.
- (30) Iosefson, O.; Olivares, A. O.; Baker, T. A.; Sauer, R. T. Dissection of Axial-Pore Loop Function during Unfolding and Translocation by a AAA+ Proteolytic Machine. *Cell Reports* **2015**, *12*, 1032–1041.
- (31) Olivares, A. O.; Kotamarthi, H. C.; Stein, B. J.; Sauer, R. T.; Baker, T. A. Effect of directional pulling on mechanical protein degradation by ATP-dependent proteolytic machines. *Proceedings of the National Academy of Sciences* **2017**, *114*, DOI: 10.1073/pnas.1707794114.
- (32) Olivares, A. O.; Baker, T. A.; Sauer, R. T. Mechanistic insights into bacterial AAA+ proteases and protein-remodelling machines. *Nature Reviews Microbiology* **2015**, *14*, 33–44.
- (33) Olivares, A. O.; Baker, T. A.; Sauer, R. T. Mechanical Protein Unfolding and Degradation. *Annual Review of Physiology* **2018**, *80*, 413–429.
- (34) Yang, Y.; Gunasekara, M.; Muhammednazaar, S.; Li, Z.; Hong, H. Proteolysis mediated by the membrane-integrated ATP-dependent protease FtsH has a unique nonlinear dependence on ATP hydrolysis rates. *Protein Science* **2019**, DOI: 10.1002/pro.3629.
- (35) Herman, C.; Prakash, S.; Lu, C. Z.; Matouschek, A.; Gross, C. A. Lack of a Robust Unfoldase Activity Confers a Unique Level of Substrate Specificity to the Universal AAA Protease FtsH. *Molecular Cell* **2003**, *11*, 659–669.
- (36) Morehouse, J. P.; Baker, T. A.; Sauer, R. T. FtsH degrades dihydrofolate reductase by recognizing a partially folded species. *Protein Science* **2022**, *31*, DOI: 10.1002/pro.4410.
- (37) Akiyama, Y.; Kihara, A.; Mori, H.; Ogura, T.; Ito, K. Roles of the Periplasmic Domain of Escherichia coli FtsH (HflB) in Protein Interactions and Activity Modulation. *Journal of Biological Chemistry* **1998**, *273*, 22326–22333.

1 Introduction

- (38) Prabudiansyah, I.; van der Valk, R.; Aubin-Tam, M.-E. Reconstitution and functional characterization of the FtsH protease in lipid nanodiscs. *Biochimica et Biophysica Acta (BBA) - Biomembranes* **2021**, *1863*, 183526.
- (39) Hari, S. B.; Sauer, R. T. The AAA+ FtsH Protease Degrades an *ssrA*-Tagged Model Protein in the Inner Membrane of *Escherichia coli*. *Biochemistry* **2016**, *55*, 5649–5652.
- (40) Hari, S. B.; Morehouse, J. P.; Baker, T. A.; Sauer, R. T. FtsH degrades kinetically stable dimers of cyclopropane fatty acid synthase via an internal degron. *Molecular Microbiology* **2022**, *119*, 101–111.
- (41) Yang, Y.; Guo, R.; Gaffney, K.; Kim, M.; Muhammednazaar, S.; Tian, W.; Wang, B.; Liang, J.; Hong, H. Folding-Degradation Relationship of a Membrane Protein Mediated by the Universally Conserved ATP-Dependent Protease FtsH. *Journal of the American Chemical Society* **2018**, *140*, 4656–4665.
- (42) Politou, A.; Thomas, D.; Pastore, A. The folding and stability of titin immunoglobulin-like modules, with implications for the mechanism of elasticity. *Biophysical Journal* **1995**, *69*, 2601–2610.
- (43) Improta, S.; Politou, A. S.; Pastore, A. Immunoglobulin-like modules from titin I-band: extensible components of muscle elasticity. *Structure* **1996**, *4*, 323–337.
- (44) Linke, W. A.; Ivemeyer, M.; Olivieri, N.; Kolmerer, B.; Rüegg, C. J.; Labeit, S. Towards a Molecular Understanding of the Elasticity of Titin. *Journal of Molecular Biology* **1996**, *261*, 62–71.
- (45) Linke, W. A. Stretching the story of titin and muscle function. *Journal of Biomechanics* **2023**, *152*, 111553.
- (46) Kellermayer, M. S. Z.; Smith, S. B.; Granzier, H. L.; Bustamante, C. Folding-Unfolding Transitions in Single Titin Molecules Characterized with Laser Tweezers. *Science* **1997**, *276*, 1112–1116.
- (47) Tskhovrebova, L.; Trinick, J.; Sleep, J. A.; Simmons, R. M. Elasticity and unfolding of single molecules of the giant muscle protein titin. *Nature* **1997**, *387*, 308–312.

- (48) Rivas-Pardo, J. A.; Eckels, E. C.; Popa, I.; Kosuri, P.; Linke, W. A.; Fernández, J. M. Work Done by Titin Protein Folding Assists Muscle Contraction. *Cell Reports* **2016**, *14*, 1339–1347.
- (49) Li, H.; Carrion-Vazquez, M.; Oberhauser, A. F.; Marszalek, P. E.; Fernandez, J. M. Point mutations alter the mechanical stability of immunoglobulin modules. *Nature Structural Biology* **2000**, *7*, 1117–1120.
- (50) Carrion-Vazquez, M.; Oberhauser, A. F.; Fowler, S. B.; Marszalek, P. E.; Broedel, S. E.; Clarke, J.; Fernandez, J. M. Mechanical and chemical unfolding of a single protein: A comparison. *Proceedings of the National Academy of Sciences* **1999**, *96*, 3694–3699.
- (51) Taniguchi, Y.; Brockwell, D. J.; Kawakami, M. The Effect of Temperature on Mechanical Resistance of the Native and Intermediate States of I27. *Biophysical Journal* **2008**, *95*, 5296–5305.
- (52) Somkuti, J.; Mártonfalvi, Z.; Kellermayer, M. S.; Smeller, L. Different pressure-temperature behavior of the structured and unstructured regions of titin. *Biochimica et Biophysica Acta (BBA) - Proteins and Proteomics* **2012**, *1834*, 112–118.
- (53) Chen, H.; Yuan, G.; Winardhi, R. S.; Yao, M.; Popa, I.; Fernandez, J. M.; Yan, J. Dynamics of Equilibrium Folding and Unfolding Transitions of Titin Immunoglobulin Domain under Constant Forces. *Journal of the American Chemical Society* **2015**, *137*, 3540–3546.
- (54) Yuan, G.; Le, S.; Yao, M.; Qian, H.; Zhou, X.; Yan, J.; Chen, H. Elasticity of the Transition State Leading to an Unexpected Mechanical Stabilization of Titin Immunoglobulin Domains. *Angewandte Chemie International Edition* **2017**, *56*, 5490–5493.
- (55) Yu, M.; Lu, J.-H.; Le, S.; Yan, J. Unexpected Low Mechanical Stability of Titin I27 Domain at Physiologically Relevant Temperature. *The Journal of Physical Chemistry Letters* **2021**, *12*, 7914–7920.
- (56) Williams, P. M.; Fowler, S. B.; Best, R. B.; Toca-Herrera, J. L.; Scott, K. A.; Steward, A.; Clarke, J. Hidden complexity in the mechanical properties of titin. *Nature* **2003**, *422*, 446–449.

1 Introduction

- (57) Rief, M.; Fernandez, J. M.; Gaub, H. E. Elastically Coupled Two-Level Systems as a Model for Biopolymer Extensibility. *Physical Review Letters* **1998**, *81*, 4764–4767.
- (58) Tong, B.; Tian, F.; Zheng, P. Interdomain Linker Effect on the Mechanical Stability of Ig Domains in Titin. *International Journal of Molecular Sciences* **2022**, *23*, 9836.
- (59) Kato, H.; Nishizaka, T.; Iga, T.; Jr., K. K.; Ishiwata, S. Imaging of thermal activation of actomyosin motors. *Proceedings of the National Academy of Sciences* **1999**, *96*, 9602–9606.
- (60) Block, S. M.; Blair, D. F.; Berg, H. C. Compliance of bacterial flagella measured with optical tweezers. *Nature* **1989**, *338*, 514–518.
- (61) Wei, D.; Dehnavi, P. G.; Aubin-Tam, M.-E.; Tam, D. Measurements of the unsteady flow field around beating cilia. *Journal of Fluid Mechanics* **2021**, *915*, DOI: 10.1017/jfm.2021.149.
- (62) Dols-Perez, A.; Marin, V.; Amador, G. J.; Kieffer, R.; Tam, D.; Aubin-Tam, M.-E. Artificial Cell Membranes Interfaced with Optical Tweezers: A Versatile Microfluidics Platform for Nanomanipulation and Mechanical Characterization. *ACS Applied Materials & Interfaces* **2019**, *11*, 33620–33627.
- (63) Ashkin, A. Acceleration and Trapping of Particles by Radiation Pressure. *Physical Review Letters* **1970**, *24*, 156–159.
- (64) Ashkin, A.; Dziedzic, J. M.; Bjorkholm, J. E.; Chu, S. Observation of a single-beam gradient force optical trap for dielectric particles. *Optics Letters* **1986**, *11*, 288.
- (65) Neuman, K. C.; Block, S. M. Optical trapping. *Review of Scientific Instruments* **2004**, *75*, 2787–2809.
- (66) Greenleaf, W. J.; Woodside, M. T.; Abbondanzieri, E. A.; Block, S. M. Passive All-Optical Force Clamp for High-Resolution Laser Trapping. *Physical Review Letters* **2005**, *95*, 208102.
- (67) Bustamante, C. J.; Chemla, Y. R.; Liu, S.; Wang, M. D. Optical tweezers in single-molecule biophysics. *Nature Reviews Methods Primers* **2021**, *1*, DOI: <https://doi.org/10.1038/s43586-021-00021-6>.

References

- (68) Mao, H.; Arias-Gonzalez, J. R.; Smith, S. B.; Tinoco Jr., I.; Bustamante, C. Temperature Control Methods in a Laser Tweezers System. *Biophysical Journal* **2005**, *89*, 1308–1316.
- (69) Joule, J. P. On the production of heat by voltaic electricity. *Abstracts of the Papers Printed in the Philosophical Transactions of the Royal Society of London* **1843**, *4*, 280–282.

Chapter 2

Building and programming a dual trap optical tweezers setup

A dual trap optical tweezers setup has the benefit of measuring at constant force and to accurately move one trapped bead while measuring the effect of this movement on the other bead some distance away. To establish a dual trap, the laser beam is polarized, split into two and recombined. The splitting in polarization allows for individual steering of each beam and thus of each trap. A new dual trap optical tweezers setup was built and improved in trapping range, compared to the existing setup. In the new setup a trapped bead can be moved as far as $10\ \mu\text{m}$ in all directions. Besides that, it is now programmed in the open source programming language Python rather than the commercial engineering software LabVIEW. Being one step closer to an open access world.

2.1 Introduction

A dual optical tweezers setup has two optical traps and two detection beams. This second trap allows for an even wider variety of measurements, each unravelling a different mechanism of biological phenomena. For example, force-extension measurements for DNA [1] or titin [2] stretching, interaction force of microtubules with a microtubule associated protein [3], stroke size determination of molecular motors [4, 5] at different forces [6], the transition of fluid flow across a lipid bilayer [7], the influence of changing force upon hairpin opening [8], and the deformability of red blood cells [9].

A dual trap optical tweezers can be constructed in multiple ways. The most commonly used designs are a time-shared multiple-beam optical trap [10, 11] or a dual-beam optical trap [1, 3, 4, 8, 10]. In a time-shared multiple-beam optical trap a single laser beam is rapidly switched between two (or more) positions, creating an optical trap at each location. With this construction, Visscher et al. [10] managed to trap ten beads with a single laser beam in ten different traps. In a dual-beam optical trap, on the other hand, a single laser beam is split into two, based on polarization. In contrast with the time-shared multiple-beam optical trap, these traps are simultaneously present and have little to no interference with one another due to the orthogonal polarizations [10].

In this chapter, I will explain the procedure used to build a dual-beam optical tweezers. First, the optical components and their alignment is discussed. As well as, how electrical and mechanical vibrations (noise) are minimized to establish precise and accurate measurements. Next, a brief explanation on how the optical tweezers is programmed and why it was decided to use the programming language Python rather than the engineering software LabVIEW. After that, the fine alignment of the detection beam and corresponding detector, as well as, three techniques to acquire and analyze the stiffness of the trap are briefly discussed. Finally, the alignment and programming are discussed.

In parallel to building and programming the optical tweezers, I familiarized myself with a dual trap optical tweezers by performing the passive force clamp experiment on the existing setup. As described in section 1.3.1, two beads were linked through a dsDNA and one bead was

trapped in the weak trap and the other one in the strong trap. The weak trap was moved and bead positions were recorded. The bead displacement from the center of the weak trap were calculated from bead positions and trap positions of the trap, and forces were calculated by the bead positions of the bead in the strong trap. With the results visualized in a force-displacement curve.

2.2 Building a dual trap optical tweezers

2.2.1 The components on the optical table

The optical tweezers setup was built on an optical table with mounting holes. All optics were mounted on a breadboard (600 mm x 900 mm x 58 mm, M6 x 1.0 Mounting Holes from Thorlabs, Inc.), rather than the table itself. The existing optical tweezers setup of the group has been moved previously. Having the optics on a breadboard instead of the table eases a relocation.

The optics (e.g. lenses and mirrors), to be mounted on the breadboard, were chosen according to Sung et al. [4] (the *4f-arrangement*, explained below) and the experience and knowledge of the group. A schematic representation of the setup is shown in fig. 2.1. The main adjustments made, compared to the existing setup, were the replacement of an expensive lens inside the microscope body by a regular optical table lens (L4 in fig. 2.1) and the *4f-arrangement*. This arrangement requires that the distance between the acousto-optic deflector (AOD)/piezo mirror 1 (PM1) and lens L3 should equal the focal length of L3 ($1f$), the distance between L3 and L4 should equal the sum of the focal length of L3 and L4 ($2f$ and $3f$), and the distance between L4 and the objective on the microscope should equal the focal length of L4 ($4f$) for the path of the 1064 nm laser in the schematic representation of fig. 2.1. This positioning ensures an efficient steering of the laser beam. The 830 nm laser path also satisfies the *4f-arrangement* with the distance between PM2/PM3 and L5 being the focal length of L5, the distance between L5 and L4 being the sum of the focal lengths, and the distance between L4 and the objective being the focal length of L4.

Before optical alignment, the beam diameter and collimation of the

2 Building and programming a dual trap optical tweezers setup

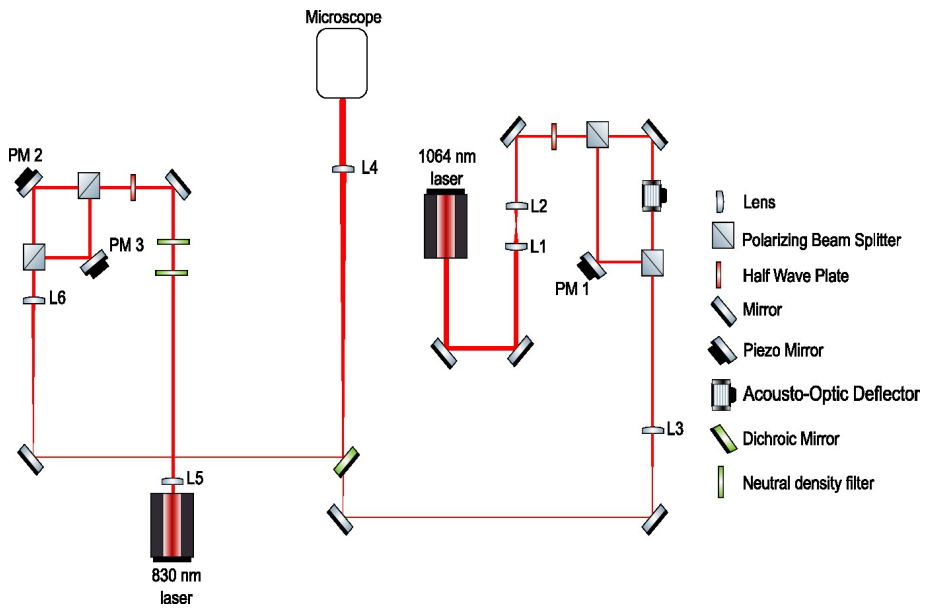


Figure 2.1: Schematic of the optical components and their alignment on the breadboard.

2.2 Building a dual trap optical tweezers

trap and detection laser were determined, see fig. 2.2. The beam diameter was determined by measuring the laser intensity with a power meter (Coherent[®] FieldMate Laser Power Meter 1098297) while blocking (part of) the laser light with a (retractable knife) blade in a stepwise manner. To do so, the blade was placed between the laser and the power meter. At first, the blade did not block any of the laser light; yielding the highest intensity as measured by the power meter. Moving the blade a known distance towards the laser beam, part of the laser beam was blocked; resulting in a lower intensity compared to the previous step. The blade was moved, and intensity was measured until the entire laser beam was blocked by the knife; resulting in zero intensity. In fig. 2.2 the intensity difference is shown, this was determined by subtracting the intensity of the next position from the intensity of the current position. As a result of the Gaussian intensity profile of the laser, the intensity difference measured also follows a Gaussian profile. This can be seen by the increase in intensity difference towards the center of the trap and a decrease afterwards. The beam diameter was then determined by the standard deviation of the Gaussian fit multiplied by two to get the diameter rather than radius.

To determine if the laser beam was collimated, the measurement described previously was carried out at two distances: first, nearby, with the blade 40 or 50 mm from the trap or detection laser, respectively, and far away, with the blade 535 or 550 mm from the trap or detection laser, respectively. The beam diameter of the trap laser was found to be 4.6 mm nearby and far away and therefore collimated. The detection beam diameter, on the other hand, was found to increase from 1.8 mm nearby to 1.9 mm far away and therefore slightly divergent. The beam was later adjusted, such that the focal height of the detection beam coincides with the focal height of the trap beam. From the beam diameters the appropriate lenses were determined, the calculations are shown in section 2.7.1.

On the breadboard, a linearly polarized Ytterbium laser (IPG YLR-10-LP-Y12, $\lambda = 1064$ nm, $P_{max} = 10$ W) was mounted and directed towards two mirrors, see fig. 2.1 for a schematic representation of the optics on the breadboard. The mirrors allow for adjustment in height, direction and angle of the laser beam, such that the beam was parallel to the breadboard in all directions. Then the beam was directed towards the beam expander, consisting of two lenses (L1 and L2) and were chosen such that the final

2 Building and programming a dual trap optical tweezers setup

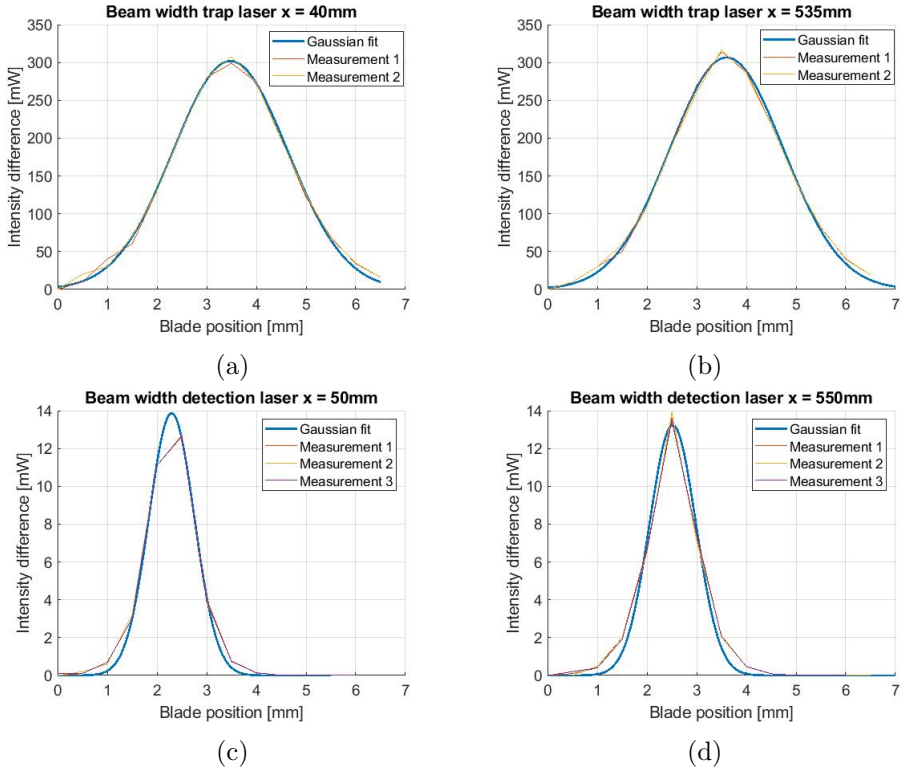


Figure 2.2: **Determination of trap and detection laser beam diameter close by and far away from the laser.** The laser beam is blocked in 0.5 mm steps with a knife blade. The change in intensity is determined by subtracting the intensity of the next step from the current intensity. a&b) Change in intensity of the trap laser with the knife blade 40 mm a) and 535 mm b) from the laser. c&d) Change in intensity of the trap laser with the knife blade 50 mm c) and 550 mm d) from the laser.

2.2 Building a dual trap optical tweezers

beam diameter was smaller than the aperture (4x4 mm) of the AOD (2-axis AOD system from IntraAction). Between L2 and the AOD, the beam passes through a half-wave plate and polarizing beam splitter. With the half-wave plate being mounted on a rotation stage with continuous 360° rotation (newport), the polarization state can be adjusted to control the laser intensity in each polarization. The polarized beam was then split into two beams one was sent to the AOD by a mirror and the other was directly sent to PM1. After the AOD and PM1, the beams were recombined by another polarizing beam splitter. A shutter was mounted between the first polarizing beam splitter and the AOD/PM1 to control the number of traps present in the sample.

An AOD device deflects and controls the angle and power of the entering laser beam. It consists of a tellurium dioxide glass cube with a transducer to generate an electrical signal of a certain frequency along the cube. The incoming laser beam is partially transmitted and partially diffracted. The frequency applied along the glass cube is used to control the angle of diffraction of one axis. To spatially control the laser beam in two dimensions a 2-axis AOD system can be used. It consists of two consecutive glass cubes with perpendicular electrical signal. Therefore, the applied signals are perpendicular to one another and to the propagation of the laser beam.

To align the AOD, the diffraction orders have to be taken into account, see fig. 2.3. After the first cube, the laser beam is partially transmitted (0th order) and partially diffracted (1st order). Both beams then enter the next cube and are again partially transmitted (0th0th order and 1st0th order) and partially diffracted (1st0th order and 1st1st order), resulting in four beams exiting the AOD. From these four beams, one beam has been transmitted through both cubes (0th0th order) and cannot be spatially controlled. Two beams are once transmitted and once diffracted and can therefore only be controlled along one axis (0th1st order and 1st0th order). The last beam (1st1st order) can be spatially controlled in both axis, as it is diffracted by both cubes. The maximum diffraction efficiency stated by the manufacturer of the AOD is > 50%. Nonetheless, the actual power of the outgoing diffraction beam is dependent on the alignment of the AOD and the amplitude of the electrical signal. The AOD is thus not only capable of spatially controlling the laser beam, but can also adjust

2 Building and programming a dual trap optical tweezers setup

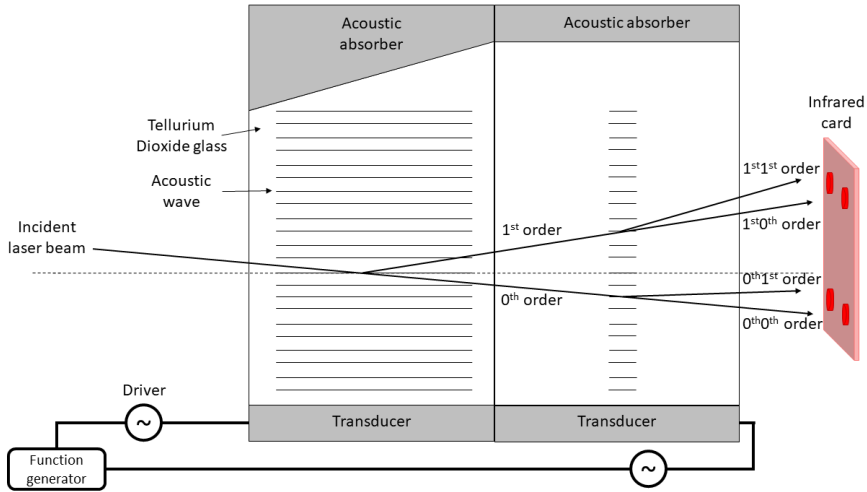


Figure 2.3: **Schematic representation of an acousto-optic deflector.**

the power of the laser beam.

To spatially control the other polarized beam, it was steered to PM1 which can also be computer controlled. However, this movement is less controllable (in terms of accuracy and speed) than with the AOD. Besides that, the power of the laser beam cannot be adjusted with this mirror, but there also is no loss of power as there is with the AOD. Nonetheless, the power of this beam can be changed by either changing the laser power or rotating the half-wave plate, simultaneously changing the power of the other beam.

After recombination of the beams, they were steered through a second beam expander (L3 and L4) to adjust the beam diameter to slightly overfill the objective aperture. Overfilling the objective ($\sim 10\%$) promotes optical trapping by obtaining a diffraction limited spot [4, 12], which increases the gradient force [12]. After L3 the beams were steered by two mirrors and transmitted through a dichroic mirror before passing through L4. This was necessary to create enough distance between L3 and L4 to satisfy the $4f$ -arrangement and simultaneously fit on the breadboard. After this lens the beams were sent towards the microscope by two mirrors, elevating the beams to match the height of the microscope (not shown in fig. 2.1).

2.2 Building a dual trap optical tweezers

On the other half of the breadboard, the detection path was lined up. The optics and their alignment were chosen to satisfy the $4f$ -arrangement and overfilling of the objective. The laser beam (TOPAG, LDT-830-30GC, $\lambda = 830$ nm) was first adjusted by L5 and then the intensity was reduced by 80% with two neutral density filters (Thorlabs, Inc. NE03B-B and NE05B-B), see fig. 2.1. The collimated and reduced beam was steered to a half-wave plate on a rotation stage by a mirror. Then the beam was split into two by a polarizing beam splitter and both beams were sent to a piezo mirror before recombining them with a second polarizing beam splitter. In the independent beam paths a shutter was placed to control the number of detection beams in the sample. After recombination, the beam diameter was adjusted by L6 and L4 to overfill the objective. The distances between PM2/PM3, L6, L4, and the objective satisfy the $4f$ -arrangement. The detection beam was combined with the trap beam by a dichroic mirror before L4 and were elevated together with the trap beam to match the microscope height as described above.

2.2.2 Microscope

The laser- and detection beam were sent into the inverted microscope (Eclipse Ti-U, Nikon) from the breadboard. With a dichroic mirror the beams were reflected towards the objective (Nikon CFI Plan Apo IR 60XC WI), while transmitting the visible light of the microscope to visualize the sample under study with a camera (Thorlabs, Inc. DCC1545M). The reflected beams were highly focused by the objective to form the trap. After focusing, the beams entered the condenser (Nikon TI2-C-LHO HNA oil lens) which collimated them. The detection beam was then reflected out of the microscope, through a lens, and was split into two with a polarizing beam splitter before illuminating the position sensitive device (PSD, DL100-7 PCBA3 First Sensor) to image the back focal plane interference pattern of a trapped bead.

The sample under study can be placed in a clamp holder on the piezo electric stage (NANO-LPS100, Mad City Labs), which is located between the objective and condenser. The sample is in contact with the objective through a layer of water or oil substitute (as described in section 3.3.2, Immersoil™W (2010), Zeiss) and on the other side with the condenser through a layer of oil (Immoil-F30CC, Olympus). The sample has sizes

2 Building and programming a dual trap optical tweezers setup

such that it fits into the sample holder and is compatible with the working distance of the objective (0.18-0.16 mm).

2.2.3 Electrical and mechanical noise

Optical tweezers are highly sensitive to vibrations. The vibrations caused by the electronics were minimized by connecting all devices (except for the power supplies of the heating system which has a regulatory system of itself) that require power to an uninterruptible power supply (UPS, Power-Walker VFI 1000 TG). The UPS provides emergency power to the devices in case of a power failure. And more importantly, the device corrects for power problems, as observed in the power sockets of the building, such as voltage spikes and harmonic distortions. Especially the laser stability was affected by these power disturbances, deteriorating trap stability.

Mechanical vibrations induced by air turbulations, for example caused by sound, temperature differences, and fans, but also vibrations from cooling fans of devices were minimized. Apparatus with fans, such as the laser power supply, the AOD driver, and computer were placed in a different room and other apparatus without fans, such as piezo stage controller, objective heating power supply and PSD reader (DAQ) were placed above the optical table and connected to their devices with a flexible cable. Mechanical vibrations of the building can be caused by the wind or traffic, but also due to people opening and closing doors between rooms with different pressure (as is the case in all of the wet lab area). These vibrations were minimized by installing the setup on a free floating table and vibration reducing floorplate, dampening any mechanical vibration.

2.3 Programming optical tweezers

2.3.1 From LabVIEW to Python

The original optical tweezers setup, build by our group, is controlled by the engineering software LabVIEW. For this new setup I decided to use the programming language Python instead. We are striving to a world with open access, which is more easily possible with the use of Python. Furthermore, it enables the setup to be independent of a company and

their updates, to be cheaper, and also we get the chance to improve, update and organize all programmed measurements.

To structure all the coding, Dr. Martin Caldarola and I decided to implement different levels: controller - model - view. In the controller level the connection/communication with the devices (waveform/function generator to control the AOD, Nano-Drive[®] to control the piezo stage, and NI DAQ-card for data acquisition) is established. The model level can be split into two subdivisions: preparation and implementation for the measurements. In the preparation subdivision, communication with the devices is established through the controller level and then prepared for further use by adding units. In the implementation subdivision, the desired measurements are programmed (e.g. moving the trap with the AOD or displacing the sample by moving the piezo stage) and the data of the PSDs are acquired. In the last level, the “view level”, the graphical user interfaces (GUIs) and the direct execution of the measurements (without GUI) are both prepared. The GUIs were made to ease the transition from LabVIEW to Python and for users unfamiliar with Python. The GUI or direct measurement can then be executed with Python.

2.4 Data acquisition and analysis

2.4.1 Alignment of the trapping and detection beams

As described above, the trap laser is split into two, based on polarization. One branch passes through the AOD (hereafter AOD trap) and the other one is controlled by the piezo mirror (hereafter piezo trap). To properly align the AOD trap with the detection beam, an AOD sweep is performed. In this sweep the trapped bead is moved laterally (along the x- or y-axis as depicted in fig. 1.7a) by changing the acoustic frequency of the AOD. The detection beam remains at its position during this sweep, but can be moved by the piezo mirror to improve alignment. The two PSDs recording the bead position are placed at a $\sim 0^\circ$ angle, which means that when sweeping along one axis the signal of only one axis changes, see fig. 2.4. The PSD position can be optimized in x-, y- and z-axis with the knobs of the translation stage (Thorlabs, Inc. DT12XYZ/M). The detection beam and PSD are correctly aligned with the trapped bead when the voltage

2 Building and programming a dual trap optical tweezers setup

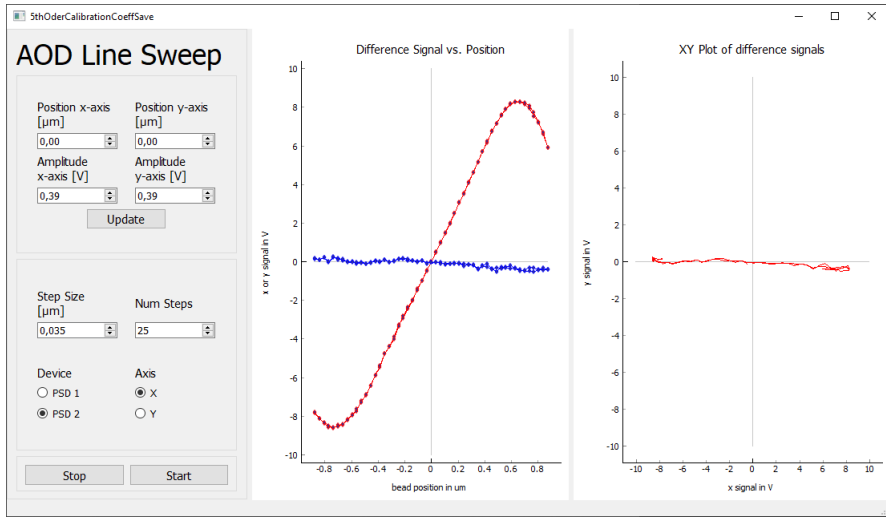


Figure 2.4: **Alignment of the detection beam and PSD with the AOD sweep.** The bead is moved $\pm 1 \mu\text{m}$ in x-axis. The red dots and line give the voltage signal in the x-axis and the blue dots and line in the y-axis.

for the x- and y-signal are zero at bead position zero and as close to 0 V as possible for the end positions of the sweep ($\pm 1 \mu\text{m}$ in fig. 2.4) in the x- and y-axis sweep.

The piezo trap has to be aligned in two steps. First, the AOD trap is moved to the desired position and used to correctly align the detection beam that corresponds to the piezo trap. The piezo trap and its detection beam are moved such that they are roughly at the desired position. Then a bead is trapped with the AOD trap and used to precisely align the detection beam (of the piezo trap). Second, the detection beam is used to align the piezo trap. The piezo trap takes over the bead that was previously trapped by the AOD trap and again the AOD sweep is initiated. However, the bead will remain stationary as it is trapped by the piezo trap which is not moving. Nonetheless, the signal of the bead is recorded by the PSDs. Whenever the signal of both axis is 0 V for all bead positions the trap is correctly aligned or outside the detection range. This should be checked before assuming correct alignment. Now, the piezo trap and



Figure 2.5: **Position calibration.** The bead was moved $0.025\ \mu\text{m}$ per step, for 8 steps in each direction ($\pm x$ -axis and $\pm y$ -axis). The colors indicate the magnitude of the voltage with red positive voltages and blue negative voltages.

its detection beam are correctly aligned and positioned.

2.4.2 Position calibration

To acquire the bead position and movements, the transmittance and deviation of the detection beam is measured by the PSD. This recorded signal is in voltage. The voltage is transformed to bead position in nanometer by the, so called, position calibration. To obtain the map the trapped bead is moved laterally (x and y) in a step wise manner by the trap laser. The detection laser remains stationary at the initial position of the bead, if well aligned, and measures the voltage signal at each position. With this step wise position measurement a grid is formed with bead positions and their voltage signal. A full map, of all bead positions within the scanned range, is then obtained by fitting a fifth order through the data set. The obtained fifth order coefficients are used to convert the position of the bead to nanometer.

2.4.3 Trap stiffness calibration

In order to determine the pulling force experienced by the bead if it displaces from the trap center, while remaining in the linear range (as explained in section 1.3.1), the stiffness of the trap has to be determined. This can be done with different methods, each with its own advantages and disadvantages [10, 13–15].

Equipartition method

One of the most fundamental and easiest ways to determine the trap stiffness is the equipartition method [10]. This method is based on a measure of thermal fluctuations in terms of position of the trapped bead. It only requires the temperature T and the variance of the bead position $\langle x^2 \rangle$ to compute the trap stiffness κ . The stiffness is computed by: $\frac{1}{2}\kappa\langle x^2 \rangle = \frac{1}{2}k_B T$ for a bead bound in a harmonic potential and with k_B the Boltzmann constant, see section 3.2.7 for a more thorough description of the method.

To obtain the variance, a graphical interface was made that allows for the position acquisition (in voltage or nanometer) for some time. This interface was designed in such a manner that it is also compatible to different types of measurements, such as the aaFtsH experiments which required a longer measurement time and lower acquisition rate, as described in chapter 4, than the stiffness measurement. When the bead recording has finished, a histogram of the measured positions (in voltage or nanometer) is plot, which can be used as a quick check for any disturbances such as a bacteria. A Gaussian distribution is expected for a bead that undergoes random thermal fluctuations, any deviation indicates an unwanted disturbance. From this Gaussian distribution, the variance of the bead position is determined to compute the trap stiffness by the Equipartition method.

The data analysis of the equipartition method can easily be computed with a self-written script. In the self-written Python script, the bead position is first converted to nanometer (the raw data is always measured in voltage), then the variance of the bead position is determined and the trap stiffness calculated. Finally, the result is plotted to allow for a visual check upon the obtained result, as shown in supplementary information section 2.7.2.

Power spectrum method

From the bead recording used to determine the trap stiffness by the Equipartition method, described above, the trap stiffness can also be determined by the power spectrum [10, 16]. The power spectrum method is based on the frequencies of vibration, induced by Brownian motion, and will be more thoroughly described in section 3.2.9. The acquired bead positions were analyzed by an open access MATLAB script from Tolić-Nørrelykke et al. [16] to compute the corner frequency and with the viscosity η of the surrounding fluid and the radius of the bead R , the trap stiffness κ can be determined with: $f_c = \frac{\kappa}{12\pi^2\eta R}$.

Drag force method

Another method to determine the trap stiffness uses the drag force on the bead, the piezo drag force method. In this method an alternating flow is induced to displace the bead from the trap center. The flow is created by moving the sample back and forth with the piezo stage at constant speed while keeping the trap and detection beam position stationary and recording the trapped bead. The graphical interface of this measurement allows the user to alter the sweeping frequency, minimum and maximum amplitude of the sweep, the number of measurements, the axis along which the sweep is performed, the sweep style (triangular or sinusoidal sweep), the recording PSD and the directory to save in. The frequency, amplitude range and number of measurement determine the speed of the moving piezo stage. For example, three measurements are desired which are performed at a frequency of 2 Hz and with a minimum and maximum amplitude of 10 μm and 30 μm (peak-to-peak), relatively. The stage is then moved at 40 $\mu\text{m/s}$ ($2 \text{ Hz} \times 2 \times 10 \mu\text{m}$, one sweep goes back and forth so the traveled path is twice 10 μm), 80 $\mu\text{m/s}$ ($2 \text{ Hz} \times 2 \times 20 \mu\text{m}$), and 120 $\mu\text{m/s}$ ($2 \text{ Hz} \times 2 \times 30 \mu\text{m}$). The sweeps can be performed along the x-axis or y-axis and according to the trap holding the bead the corresponding PSD should be selected. Each measurement is saved in voltage in a different file with the filename including the axis, waveform, frequency, and amplitude.

To determine the stiffness the displacement of the bead from the trap center during the sweep needs to be computed, see section 3.2.7 for more details. First, the position in voltage is converted to nanometer by the

2 Building and programming a dual trap optical tweezers setup

fifth order coefficients of the position calibration. Then, depending on the performed sweep style (triangular or sinusoidal sweep), the data is fitted with a square or sinusoidal waveform, respectively. Throughout this thesis a triangular sweep is used to move the sample. From this fit the bead displacement is extracted for each measurement (the different amplitudes/speeds at which the sweep is performed), and by fitting a linear fit through the computed stiffnesses (for more than three measurements) the final stiffness of the trap in the sweeping axis is determined.

2.5 Passive force clamp experiment

2.5.1 Materials and method

Anti-Dig beads

Carboxylated polystyrene beads with diameter 1.00 μm (Polyscience Inc.) were coated with anti-digoxigenin (anti-Dig, Sigma-Aldrich). The carboxylated polystyrene beads were mixed with MES buffer (0.1 M MES buffer with 0.01 % tween-20 pH 4.5) and centrifuged (10 min at 5.000 rpm). The beads were washed 5 times with by centrifugation (10 min at 5.000 rpm) and resuspension in MES buffer. The washed beads were sonicated for 2 minutes in an ice bath. Freshly made EDC solution (2 % weight to volume) was added to the beads and the bead solution was rotated for 3 hours at room temperature. The bead solution was then centrifuged (10 min at 5.000 rpm) and resuspended in borate buffer twice, before a 2 minute sonication in an ice bath.

After sonication, 200 $\mu\text{g}/\text{mL}$ anti-Dig and 5 mg/mL BSA (bovine serum albumin) in borate buffer were added to the beads and the beads were rotated for 1 hour at room temperature and then overnight in a 4 °C room. The reaction was stopped by adding 0.25 M ethanolamine and mixed for 30 minutes on a rotator at 4 °C. The beads were centrifuged (10 min at 5.000 rpm) and resuspended in 10 mg/mL BSA in PBST (phosphate buffered saline with 0.01 % tween-20). The beads were sonicated for 1 minute in an ice bath and stored on a moving plate at 4 °C.

Biotin digoxigenin DNA

To construct the 3500 base-pair biotin digoxigenin DNA, a PCR using M13mp18 plasmid as template and two primers (an oligonucleotide primer with a 5' biotin and an oligonucleotide primer containing a 5' digoxigenin) was performed.

Flow cell

A simple flow cell consisting of a cleaned microscope slide (77x26x1 mm), two pieces of double-sided tape (forming the channel), and a cleaned cover slip (40x22x0.15 mm) was prepared. The flow cell was functionalized by PBS. Streptavidin beads (diameter 1.25 μm) were introduced in the flow cell, which would weakly bind to the glass surface. The non-bound beads were removed by washing the flow cell with 80 μL 50 $\mu\text{g}/\text{mL}$ BSA in PBS. Then the biotin digoxigenin DNA was introduced and incubated for 10 minutes. The flow cell was washed with 20 μL PBS before introducing the anti-Dig beads and sealing the in- and outlet of the flow cell.

Optical tweezers experiment

The flow cell was clamped onto the piezo stage holder and brought into contact with the objective and condenser through a layer of oil. When this experiment was performed, the setup had a 100x oil immersion objective (Nikon CFI Apo TIRF 100XC Oil) rather than the 60x water immersion objective that was later installed.

The AOD and piezo trap were aligned, such that there was 2.05 μm between the two traps. This was close to the expected length (bead-DNA-bead, 0.50 μm -1.00 μm -0.625 μm). The AOD trap was then moved \sim 0.19 μm towards the piezo trap, to ensure a non-stretched starting position and therefore to measure the complete force-displacement curve.

An anti-Dig bead was trapped in the weak AOD trap and brought in close proximity to the DNA bound streptavidin bead. To check if a DNA link was established between the beads, the AOD bead was moved away from the streptavidin bead. If the anti-Dig bead was pulled out of the trap, a link had established and the bead was trapped again. The streptavidin bead was then trapped by the strong piezo trap and the beads were

2 Building and programming a dual trap optical tweezers setup

moved upwards. The detection beams were unblocked and the recording was started. In the recording the anti-Dig bead was moved away from the streptavidin beads for 300 steps of step size 2.56 nm, while the bead position was recorded for 50 ms at 50 kHz each step.

After this recording, the calibration measurements (position calibration, a 3 s data acquisition, and drag force calibration) were performed with different beads than the passive force clamp measurement, as the beads would remain linked and were both trapped in the strong trap at the end of the measurement. The drag force calibration was done for amplitude range 1-50 μm (peak-to-peak), in 10 steps, and a sinusoidal sweep with a 2 Hz period.

Data analysis

Bead position were converted to nanometer. The bead displacement from the trap center (weak trap) was determined by the position of the trap minus the measured bead position, until the bead was pulled out of the trap. The pulling force was determined by the bead position of the bead in the strong trap times the trap stiffness, which was determined by the drag force method. These results were plotted as the force-displacement curve.

The force-displacement curve was then fitted by the derivative of a Gaussian:

$$F = \frac{-ax}{\sigma^2} e^{-\frac{x^2}{2\sigma^2}} \quad (2.1)$$

with F the pulling force, x the displacement from the center, and fitted values a and σ .

The force-displacement results of the drag force of the weak AOD trap were also added to the curve. The force-displacements of the drag force can only be obtained in the linear region and should be similar to the results of the passive-force clamp measurement.

2.5.2 Results

The force-displacement curve was computed and is shown in fig. 2.6. The weak trap had a stiffness of 0.07 pN/nm and the strong trap a stiffness of

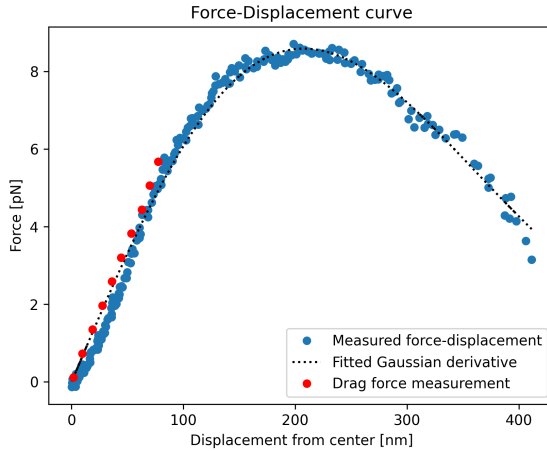


Figure 2.6: **Measured force-displacement curves, the fitted derivative of a Gaussian, and force-displacement obtained by the drag force.** a) Obtained force-displacement curve for the newly build optical tweezers with 100x oil immersion objective. b) Obtained force-displacement curve for the existing optical tweezers with 60x water immersion objective.

0.20 pN/nm. Similar to Greenleaf et al. [8], the trap has a linear region for displacement up to 100 nm and a passive force region of ~ 50 nm.

2.6 Discussion

2.6.1 Optical alignment

To build a high performance optical tweezers setup, it is of great importance that the laser beam is collimated before entering the objective. In this setup, the collimation of the laser beam was first checked by measuring the beam diameter close by and far away from the laser. This was done by blocking the laser beam in a step wise manner while measuring the intensity with a power meter. Then after each beam expander the collimation had to be checked to ensure correct positioning of the lenses. Due to a lack of space, to measure far away, this was done in a different

2 Building and programming a dual trap optical tweezers setup

manner. Now, a piece of paper with millimeter grid was placed in the beam path (which had a reduced intensity) and a picture of the laser spot was taken. Near infrared light can be seen with a camera, but not by eye. This was done close by and far away from the beam expander. However, it was difficult to accurately capture and measure the beam diameter and was therefore approximated. To ease and improve this alignment, I recommend using an interferometer when space is limited. These devices are highly qualified to accurately determine collimation and are commercially available.

Nonetheless, the new setup improved in trap movability. In the other setup, the bead could only be moved $\sim \pm 2 \mu\text{m}$ away from the center in one direction (both AOD and piezo trap). In the new setup, the bead could still be trapped $\sim \pm 10 \mu\text{m}$ from the center position in all directions. This is a major improvement and is most likely due to the fact that this setup satisfies the before mentioned *4f-arrangement*. However, both optical tweezers have showed to perform well in spatial-temporal resolution, and in force range at the center position.

2.6.2 Programming

The new setup is controlled with Python instead of LabVIEW, this transition was time consuming but effective. The setup no longer depend on company updates and their support on different versions. For example, when a LabVIEW file was opened with a newer version of LabVIEW, it could no longer be opened with an older version, which was relevant because the first setup is controlled by an old version of LabVIEW. Besides that, with Python we are one step closer to an open access world.

However, our decisions to implement GUIs for easier use comes with a drawback. Only one GUI can be displayed at a time. With LabVIEW you could have different interfaces open to sequentially initiate different measurements. It is therefore more time consuming to do a series of measurements (position calibration, data acquisition, drag force calibration for example) in Python, when using GUIs, than in LabVIEW. An easy solution is to not use GUIs in that case, but just write a new script that performs the series of experiments, as I did. Now, it actually became less time consuming and also less erroneous as I no longer had to manually name files and could run the series multiple times without intervention.

Being familiar with Python as user has great advantages.

Another decision that I made was to display bead position in nanometer instead of mega Hertz, which is the bead position in terms of AOD frequency. An optical tweezers setup dependent constant converts the mega Hertz position to nanometer. The direct conversion eases data interpretation and variable setting. The mega Hertz to nanometer constant should be checked regularly as this might slightly change over time. With the direct conversion in the new setup it is even more important to check this constant regularly to ensure that the desired and actual position correspond.

At the moment, the piezo trap has to be calibrated (AOD sweep and position calibration) with the AOD trap, because the piezo mirror of the piezo trap cannot yet perform a computer controlled, precise step wise movement. When working with two traps, it would certainly be advantageous, in terms of time and precision, to perform the piezo trap calibration with the piezo mirror itself. Therefore, I recommend that the script that I started will be functionalized and finished to enable quick and precise calibration of the piezo trap.

Even though Python is not dependent on company updates it still needs to be updated regularly. At the moment, there are already package updates available that need to be installed. However, these include some minor changes causing our current script to be incompatible with the newer version. To guarantee future efficacy the setup requires care and attention.

2.6.3 Passive force clamp

The force-displacement curve of the newly build setup is expected to be comparable to the one obtained for the existing setup, as both setups use the same water immersion objective. On the other hand, the force-displacement curve of the new setup might differ from the existing one as many other components differ, such as the overfilling of the objective and the lenses. Care will be taken if forces have to be computed from bead displacements that are larger than 100 nm

2.7 Supplementary material

2.7.1 Beam expander calculations

There are two beam expanders present in the trap laser path. The first beam expander decreases the beam diameter to match the aperture of the AOD (4x4 mm). The beam diameter 4.6 mm is reduced by a factor of 0.76 to 3.5 mm. To do so, L1 has a focal length of 50.2 mm (Newport Corporation KPX082AR.33) and L2 a focal length of 38.1 mm (Newport Corporation KPX079AR.33), as depicted in fig. 2.1. Then the beam is expanded 2.4 times to 8.4 mm by the second beam expander, overfilling the objective by 5%. This is done by L3 with a focal length of 250 mm (Newport Corporation KPX109AR.33) and L4 with a focal length of 600 mm (Newport Corporation KPX119).

The first lens (Thorlabs Corporation LA1978 with focal length 750 mm) in the detection beam path is used to collimate the laser beam. Then the beam expander is used to expand the detection beam to overfill the objective. The beam of 1.8 mm is expanded 4.8 times to 8.6 mm. The expansion is carried out by L6 with focal length 125 mm (Newport Corporation KPX097AR.16) and L4 with focal length 600 mm (Newport Corporation KPX119).

2.7.2 Data analysis equipartition method

"""

Created on Tues Dec 19 17:00 2018

@author: cvanaartrijk

"""

```
from os import path
```

```
import numpy as np
```

```
import matplotlib.pyplot as plt
```

```
Temp      = 20.0           #temperature [degrees Celsius]
```

```
Kelvin    = 273.15        #Zero Kelvin [K]
```

```
acq_rate  = 100           #acquisition rate [kHz]
```

```
Kb        = 0.0138065     #Boltzmann constant [pN*nm/K]
```

2.7 Supplementary material

```

date = '230511'
# First load the 5th order coefficients
# and the recorded raw data
root_fdpth = r'M:\tnw\bn\mea\Shared\Chaline\
-----Optical-tweezer\2023\2023-05-11'
coeff_path = path.join(root_fdpth, '5th_order2.dat')
root_fdpth_V = r'M:\tnw\bn\mea\Shared\Chaline\
-----Optical-tweezer\2023\2023-05-11'
volt_path = path.join(root_fdpth_V, 'rawdata_V.dat')
# New filename
new_filename = date+'rawdata_nm.dat'

# Load data 5th order coefficients
Coeff_x = np.loadtxt(coeff_path)[: ,0]
Coeff_y = np.loadtxt(coeff_path)[: ,1]
# Load raw data voltages
Vx = np.loadtxt(volt_path)[: ,0]
Vy = np.loadtxt(volt_path)[: ,1]

# Convert voltage into nm with 5th order coefficients
nm = np.zeros((len(Vx),2))
ones = np.ones(len(Vx))
Hessian = np.matrix([
    ones,          Vx,          Vy,
    Vx**2,        Vy**2,        Vx**3,
    Vy**3,        Vx**4,        Vy**4,
    Vx**5,        Vy**5,        Vx*Vy,
    Vx**2*Vy,    Vx*Vy**2,    Vx**3*Vy,
    Vx**2*Vy**2, Vx*Vy**3,    Vx**4*Vy,
    Vx**3*Vy**2, Vx**2*Vy**3,    Vx*Vy**4])
Vtoum_y = Coeff_y*Hessian #[um]
Vtoum_x = Coeff_x*Hessian #[um]
Mean_Vtoum = [np.mean(Vtoum_x[0,0:n]),
               np.mean(Vtoum_y[0,0:n])]
# Final position in nanometer, subtract mean to have

```

2 Building and programming a dual trap optical tweezers setup

```
# Brownian motion around 0 nm
nm[:,0] = (Vtoum_x - Mean_Vtoum[0])*1000
nm[:,1] = (Vtoum_y - Mean_Vtoum[1])*1000

# Calculate stiffness from variance
AOD_xVar = np.var(nm[:,0])           #[nm^2]
AOD_yVar = np.var(nm[:,1])           #[nm^2]
Ky = ((Temp+Kelvin)*Kb)/AOD_yVar     #[pN/nm]
Kx = ((Temp+Kelvin)*Kb)/AOD_xVar     #[pN/nm]

# Prepare x-axis time in seconds
t = np.linspace(0, len(nm)/(acq_rate*1000), len(nm))

# Save nm data and plot
volt_nm_path = path.join(
    root_fdpth, new_filename)
result_fig_fdpth = SF.MakeDirectory(path.join(
    root_fdpth_V,
    'figures'))
np.savetxt(volt_nm_path, nm)

# Plotting and saving plot
plt.figure(1)
ax = plt.subplot(211)
plt.plot(t, nm[:,0], '.', markersize=1)
plt.text(0.1, 0.9, '$K_{x, var}$'+str(round(Kx,3))+
    ' pN/nm', horizontalalignment='left',
    verticalalignment='top',
    transform=ax.transAxes)
plt.xlabel('Time [sec]')
plt.ylabel('Bead motion [nm]')
plt.title('Bead position (x-axis)')
plt.axis([0, t[-1], min(nm[:,0]), max(nm[:,0])])

ax = plt.subplot(212)
plt.plot(t, nm[:,1], '.', markersize=1)
```

2.7 Supplementary material

```
plt.text(0.1, 0.9, '$K_{y,var}$'+str(round(Ky,3))+
        'pN/nm', horizontalalignment='left',
        verticalalignment='top',
        transform=ax.transAxes)
plt.xlabel('Time (sec)')
plt.ylabel('Bead motion (nm)')
plt.title('Bead position (y-axis)')
plt.axis([0, t[-1], min(nm[:,1]), max(nm[:,1])])
plt.tight_layout()

fig1_pth = path.join(
    result_fig_fdpth, new_filename
    [0: len(new_filename)-4]+
    '_fig.png')
plt.savefig(fig1_pth, format='png', dpi=300)
plt.close()
```

References

- (1) Mao, H.; Arias-Gonzalez, J. R.; Smith, S. B.; Tinoco Jr., I.; Bustamante, C. Temperature Control Methods in a Laser Tweezers System. *Biophysical Journal* **2005**, *89*, 1308–1316.
- (2) Leake, M. C.; Wilson, D.; Gautel, M.; Simmons, R. M. The Elasticity of Single Titin Molecules Using a Two-Bead Optical Tweezers Assay. *Biophysical Journal* **2004**, *87*, 1112–1135.
- (3) Qu, E.; Guo, H.; Xu, C.; Liu, C.; Li, Z.; Cheng, B.; Zhang, D. Method used to measure interaction of proteins with dual-beam optical tweezers. *Journal of Biomedical Optics* **2006**, *11*, 064035.
- (4) Sung, J.; Sivaramakrishnan, S.; Dunn, A. R.; Spudich, J. A. In *Methods in Enzymology*; Elsevier: 2010; Chapter 14, pp 321–375.
- (5) Olivares, A. O.; Nager, A. R.; Iosefson, O.; Sauer, R. T.; Baker, T. A. Mechanochemical basis of protein degradation by a double-ring AAA+ machine. *Nature Structural; Molecular Biology* **2014**, *21*, 871–875.
- (6) Aubin-Tam, M.-E.; Olivares, A. O.; Sauer, R. T.; Baker, T. A.; Lang, M. J. Single-Molecule Protein Unfolding and Translocation by an ATP-Fueled Proteolytic Machine. *Cell* **2011**, *145*, 257–267.
- (7) Amador, G. J.; van Dijk, D.; Kieffer, R.; Aubin-Tam, M.-E.; Tam, D. Hydrodynamic shear dissipation and transmission in lipid bilayers. *Proceedings of the National Academy of Sciences* **2021**, *118*, DOI: 10.1073/pnas.2100156118.
- (8) Greenleaf, W. J.; Woodside, M. T.; Abbondanzieri, E. A.; Block, S. M. Passive All-Optical Force Clamp for High-Resolution Laser Trapping. *Physical Review Letters* **2005**, *95*, 208102.
- (9) Inanc, M. T.; Demirkan, I.; Ceylan, C.; Ozkan, A.; Gundogdu, O.; Goreke, U.; Gurkan, U. A.; Unlu, M. B. Quantifying the influences of radiation therapy on deformability of human red blood cells by dual-beam optical tweezers. *RSC Advances* **2021**, *11*, 15519–15527.

- (10) Visscher, K.; Gross, S. P.; Block, S. M. Construction of Multiple-Beam Optical Traps with Nanometer-Resolution Position Sensing. *IEEE Journal of Selected Topics in Quantum Electronics* **1996**, *2*, 1066–1076.
- (11) Deng, Y.; Bechhoefer, J.; Forde, N. R. Brownian motion in a modulated optical trap. *Journal of Optics A: Pure and Applied Optics* **2007**, *9*, S256–S263.
- (12) Jones, P. H.; Maragò, O. M.; Volpe, G., *Optical Tweezers*; Cambridge University Press: 2015.
- (13) Svoboda, K.; Block, S. M. Biological Applications of Optical Forces. *Annual Review of Biophysics and Biomolecular Structure* **1994**, *23*, 247–285.
- (14) Smith, S. B.; Cui, Y.; Bustamante, C. In *Methods in Enzymology*; Elsevier: 2003, pp 134–162.
- (15) Tolić-Nørrelykke, S. F.; Schäffer, E.; Howard, J.; Pavone, F. S.; Jülicher, F.; Flyvbjerg, H. Calibration of optical tweezers with positional detection in the back focal plane. *Review of Scientific Instruments* **2006**, *77*, 103101.
- (16) Tolić-Nørrelykke, I. M.; Berg-Sørensen, K.; Flyvbjerg, H. MatLab program for precision calibration of optical tweezers. *Computer Physics Communications* **2004**, *159*, 225–240.

Chapter 3

Local temperature sensing in optical tweezers with dual-sided heating approach

Many biological processes occur at temperatures above room temperature. Experimentally studying these processes at room temperature may lead to observations that do not correspond to the *in vivo* behavior. Therefore, it is often desirable to heat up the sample under study. Up to now, there was no convenient, fast, and objective-condenser optical tweezers setup compatible technique to heat up the whole sample above 40 °C. We propose an innovative design for a flow cell heating system that is compatible with objective-condenser optical tweezers and has a compact heating source, reducing stabilization time. The heating system obtained temperatures up to 70 °C, verified both by a thermocouple ~ 2 mm away from the trapped bead and by our presented method to locally determine the temperature. This flow cell heating system and the method to locally determine the temperature allows us to study temperature-dependent phenomena with pico-Newton resolution.

* Parts of this chapter will be submitted for publication

3.1 Introduction

Heating a sample in optical tweezers is challenging, because of the limited space around the sample, the (temperature sensitive) optics around it, and the need to transmit (near) infrared laser light through the system. Though, changing the temperature may reveal interesting features. With our double trap optical tweezers, the interaction of a fluid flow on a free-standing lipid bilayer has been studied [1]. With the ability to increase temperature, the transition state from a solid-like to a gel-like lipid phase can be studied [2–4].

One heating approach would be to heat the full setup, which is expensive and slow to stabilize. A simpler approach is to only heat the microscope objective [5–7]. However, on our setup, which consists of one objective below the sample, a temperature gradient inside the sample needs to be taken into account. Thereby, the maximum temperature supported by most objectives is usually 40 °C. Other approaches, which would not be limited by the objective, but can locally heat the sample are metal nanoparticles [8], heating with a (IR780) dye [9] and heating induced by a second laser [6, 10]. However, they induce a steep temperature gradient around the nanoparticles or laser [6, 8–10].

In this study, we propose a novel approach to address these challenges. Our method involves dual-sided heating of the sample, achieved through the application of the Joule effect [11]. By passing an electrical current through a conductive wire around the objective or a conductive layer on the microscope slide, the amount of heat generated is controlled. The microscope slide is coated with a transparent conductive layer of ITO (indium-tin oxide), while the objective is equipped with a resistive wire wrapped around it. This setup ensures that the sample is heated uniformly from both the top and bottom, effectively eliminating unwanted temperature gradients with a maximum heat of the sample to 70 °C while maintaining an objective temperature below 40 °C.

We also present a novel method for local temperature determination. Our approach suggests the use of trap stiffness calculation by the equipartition method in conjugation with the drag force method or power spectrum method to evaluate the viscosity of the surrounding medium, which depends on temperature. Additionally we employ a thermocouple probe

inside the flow cell at ~ 2 mm distance from the trap location as a control.

Upon testing the laser-induced heating in our ITO flow cell design, it was found that laser absorption by the ITO layer drastically contributes to the local temperature rise in the flow cell. The temperature increase recorded by the thermocouple rose to $2.5^\circ\text{C}/100$ mW, whereas the E-DF method yielded a substantially higher temperature increase of $14.4^\circ\text{C}/100$ mW. The effect of laser-induced heating was minimized by reducing the laser power as much as possible.

The heating experiments, performed at low laser power, demonstrated that temperatures up to 70°C were obtained when the objective and ITO heating systems were combined or by solely using the ITO heating system. Objective heating could not reach these high temperatures due to the maximal supported temperature of 40°C of the objective. Comparing the temperatures computed from our method(s) by the temperature measured with the thermocouple temperature indicated that the rise in temperature upon heating was comparable, but showed a discrepancy of a few degrees Celsius due to laser-induced heating.

The experiments mentioned above were all performed at the center of the flow cell (in terms of height). Changing the focal height in the flow cell corresponds to a change in distance between the objective and the flow cell. The computed temperature at different heights indicated that the local temperature remains constant.

Our novel method to determine the local temperature shows the importance of local temperature measurements. Even at low laser power, laser-induced heating was non-negligible in our ITO flow cell. Studying laser-induced heating in a standard non-conductive glass flow cell demonstrated a temperature rise of $2.8^\circ\text{C}/100$ mW, which aligns well with previously reported findings [12–14], and is thus non-negligible for higher laser powers.

The method to determine the temperature employs the change in viscosity upon temperature. However, this might be unknown for the experimental buffer. Our method can be used to study this relation when a thermocouple is added. The thermocouple measures the change in temperature while the trapped bead is used to determine the viscosity. Next to that, the heating system can be used to study biological processes at physiological temperatures if below 70°C and is especially valuable for

3 Local temperature sensing in OT with dual-sided heating approach

any objective-condenser optical tweezers setup.

Our (double-sided) heating system is not limited to optical tweezers setups. The system can be used on any microscopy setup, with the thermocouple to measure the flow cell temperature.

3.2 Materials and methods: our design

3.2.1 Objective heating

To realize objective heating, a conductive wire was twisted around and mounted on the objective. A current running through this wire allows us to control the temperature [11] of the objective, which should not exceed 40 °C to avoid risk of damage. The temperature was measured by a PT100 sensor mounted between the objective and the conductive wire. A **proportional-integral-derivative** controller (PID controller) was used to have a fine control of the temperature.

3.2.2 Thermocouple

To monitor the temperature within the sample, a type T thermocouple with an approximate thickness of 80 µm was fabricated. The type T thermocouple accurately (± 0.1 °C) measures temperatures between -200 °C and 200 °C. The copper- (TFCP-003-50, Omega) and a constantan (TFCC-003-50, Omega) wires were fused together using an electric spark. The average flow cell height in our study is 107 µm. Consequently, the thermocouple is designed to measure the average temperature within the channel and is positioned to accurately represent the temperature at the vertical midpoint of the flow cell.

3.2.3 Copper flow cell

Our first heating flow cell was designed by Dr. Roland Kieffer and had two copper circuits taped on a microscope slide (see fig. 3.1). To make it, the microscope slide was cleaned in a glass beaker filled with demineralized water and 3-5% hellmanex[®] III, the beaker was sonicated in a sonication bath for 30 minute. The hellmanex[®] III was removed by rinsing the beaker and slides 5 times with demineralized water. The beaker with slides, filled

3.2 Materials and methods: our design

with demineralized water, was sonicated for 25 minute and then dried with a nitrogen blow gun and stored in a 50 mL tube.

The copper circuits were made on the cleaned microscope slide. A piece of copper tape (5×2.5 cm) was taped on the microscope slide and pressed with tweezers to tightly stick to the glass surface. Then the copper surface was cleaned with a tissue and acetone. After evaporation of the acetone, a similar sized piece of packaging tape was placed on the copper tape. The circuit pattern was engraved in the packaging and copper tape with a laser cutter. The packaging tape was then removed from the non-circuit parts, revealing the copper. The entire slide was cleaned by spraying acetone, ethanol, and then demineralized water over it and dried with the nitrogen blow gun.

The cleaned copper microscope slide was placed, with the copper facing downwards, in a glass Petri dish filled with Cl_3Fe . This dissolves the unshielded copper and does not affect the copper shielded by the packaging tape. After 15 to 30 minutes the microscope slide was removed from the Cl_3Fe with tweezers and rinsed with demineralized water. The circuit, covered by the packaging tape, was peeled off the copper tape, revealing two copper circuits with the flow channel between them. At the flow channel position the Cl_3Fe dissolved the copper but did not affect the glue of the tape. To remove the glue, ethanol was put on the glue and scratched off with a scalpel. Exposing the transparent glass microscope slide.

The solution under study has to be shielded from the current running through the copper. The shield was created by a droplet of UV curing optical glue (NOA81), which was spread out and flattened by a polydimethylsiloxane (PDMS) block and cured by UV-light for 5 minute. The NOA81 should not cover the ends of the circuits, as electrodes were soldered on them. Three wires were soldered on the ends, two of them were connected to the power supply and one connected the two copper circuits. In the last step, two pieces of heat resistant double sided tape (Scotch[®], Pressure Sensitive Tape) were used to glue a coverslip on the copper circuit, creating the flow channel.

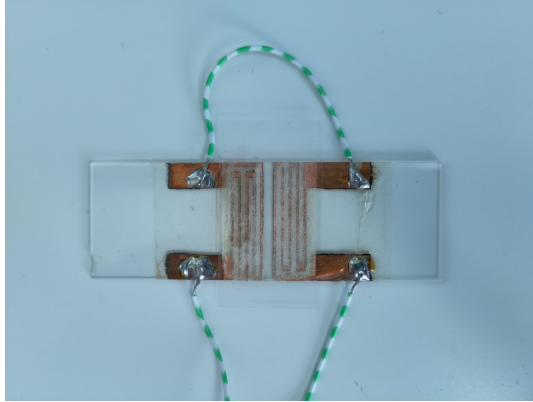


Figure 3.1: Copper flow cell

3.2.4 ITO flow cell

The indium-tin oxide (ITO) flow cell was designed by Dr. Roland Kieffer and I and consisted of a soda-lime glass slide with a thin layer ($\sim 220 \pm 50$ nm) of ITO deposited on one side (conductivity $7 \Omega/\text{sq}$), two coverslips (22x40x0.15 mm and 10x10x0.10 mm), UV-curing optical glue (NOA81), silver paint, copper tape, kapton[®] tape, soldering tin and two electrical wires, see fig. 3.2. In this flow cell design it is possible to put a thin thermocouple inside the flow cell.

To make the flow cell, the 100x100x1.1 mm ITO glass (GuangYi Store) was etched with a laser cutter and then broken into 12 slides of 75x10 mm. The dimensions of the glass slide were chosen such that it was compatible with our optical tweezers setup. The length was based on our optical tweezers holder, the width corresponds to the diameter of the objective, and the thickness meets the working distance of the condenser.

The ITO glass slides and the coverslips were cleaned and dried as described in 3.2.3. A clean 10x10x0.10 mm coverslip was glued on the ITO layer of the cleaned ITO glass slide by UV-curing the NOA81. After curing, it was cleaned and dried as described in section 3.2.3. Next, the electrodes were prepared. A piece of copper tape (150x5 mm) was cut in half along the long side of the tape. One of the pieces was stuck (glue on glue) on a piece of kapton[®] tape (170x10 mm), see fig. 3.2a. The other

3.2 Materials and methods: our design

piece of copper tape was stored and later used for other ITO flow cells. Then two lines of silver paint were painted on the ITO layer on either side of the coverslip and ~ 3.0 cm apart (center-to-center), see fig. 3.2b. A small piece of the copper/kapton[®] tape was placed on the silver paint with the copper on top of the silver paint. The tapes were a bit longer than the flow cell such that a wire can be soldered on it, see fig. 3.2c.

To create the flow channel, a PDMS-mold was made. A 22x40x0.10 mm coverslip was broken into two pieces and placed in aluminum foil, that was folded into a rectangular ‘boat’, with a ~ 3 mm gap between the pieces of glass. This gap will later form the negative of the channel. Then PDMS base and curing agent were mixed together with a 10:1 ratio and poured into the aluminum boat and cured in the oven for at least 4 hours at 80 °C. When the mold was cooled down the glass was removed and the mold was used to make the flow channel on the ITO slide. The PDMS-mold reversibly sticks to the ITO glass slide, see fig. 3.2d.

When desired, a thermocouple was placed next to the flow channel and between the glass slide and the mold. The thermocouple is ~ 80 μm thick and the space between the mold and glass slide is ~ 100 μm (from the dimensions of the coverslip used to make the mold). The rest of the space was filled by NOA81 through capillary forces, forming two NOA strips. The NOA strips were cured for 5 min by UV-light and the mold was removed, see fig. 3.2e. Two tiny droplets NOA81 are placed on the cured strips and then the 22x40x0.15 mm coverslip was placed on top of the on-cured NOA81 and then cured for 30 second in UV-light. In the last step, to create the heating flow cell, the electrodes were soldered on the ends of the copper tape, see fig. 3.2f and fig. 3.2g.

3.2.5 Sample preparation

All samples studied in this chapter consisted of the same bead concentration, except for section 3.3.2 in which ultrapure water was used. The bead solution stored in the fridge was a 1:1000 dilution of diameter 1.93 μm polystyrene beads (PolyScience[®]) in ultrapure water. Before the measurement, the bead solution was removed from the fridge, mixed by shaking, and further diluted by mixing 0.3 μL bead solution in 1000 μL ultrapure water. Roughly 20 μL was then pipetted at one side of the flow channel which filled itself by capillary forces. The excess bead solution was

3 Local temperature sensing in OT with dual-sided heating approach

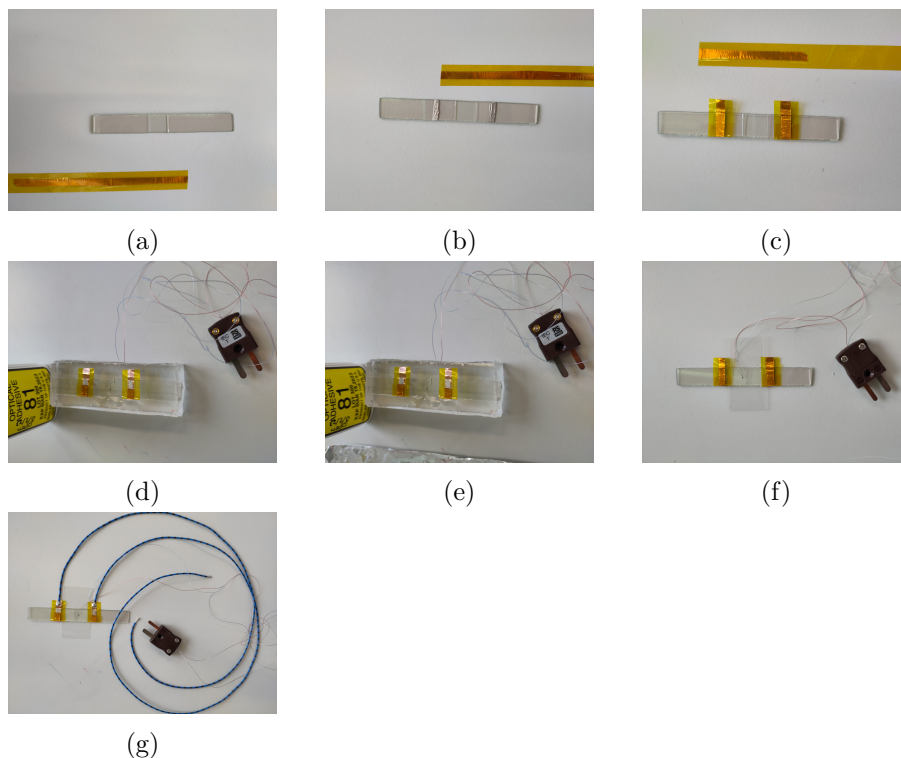


Figure 3.2: **Making an ITO flow cell.** a) ITO slide with coverslip and prepared kapton[®]/copper tape. b) ITO slide with coverslip and silver paint. c) ITO slide with coverslip, silver paint, and kapton[®]/copper tape. d) PDMS mold with ITO flow cell and thermocouple. e) PDMS mold with ITO flow cell and thermocouple. f) ITO flow cell with thermocouple in NOA strip. g) ITO flow cell with thermocouple in NOA81, coverslip and soldered electrodes. h) ITO flow cell with coverslip and soldered electrodes.

removed with a tissue and the channel was closed with a 2:1 mixture of silicon grease (VWR Chemicals BDH[®]) and silicon oil (Sigma-Aldrich).

3.2.6 Heating protocol

There are three heating protocols to heat the sample: with the objective, ITO, or both. When only objective heating was desired, the temperature was set on the PID controller, never exceeding 38 °C. For ITO heating, the thermocouple inside the NOA81 strip was used to control the heating. The desired temperature was manually adjusted with a supply voltage. It has been observed that the sample heats much quicker with ITO than with the objective. When heating with the objective and ITO were combined, the temperature of the objective was first set at the desired temperature by the PID controller. When stable, the temperature monitored by the thermocouple in the flow cell was used to obtain the desired temperature by progressively increasing the voltage supply of the ITO. When temperature was stable, the trap was calibrated by the position calibration, described in section 2.4.2.

3.2.7 Equipartition method + Drag Force method (E-DF method)

A trapped bead in an aqueous liquid undergoes Brownian motion within the trap. A bead displaced from the trap center will feel an attractive force towards the center of the trap. For small displacements the trap behaves as a linear spring. The force (F) therefore follows Hooke's law ($F = \kappa x$), and is dependent on the stiffness of the trap (κ) and the position of the bead (x). The potential energy (U) of a trapped bead then equals $U = \frac{1}{2}\kappa x^2$ and the displacement of the bead depends on the thermal energy of the surrounding liquid, due to the equipartition theorem, which states that energy is shared equally between all degrees of freedom when in thermal equilibrium [15]. The theorem results in the following equation:

$$\frac{1}{2}\kappa\langle x^2 \rangle = \frac{1}{2}k_B T \quad (3.1)$$

with $\langle x^2 \rangle$ the variance of the bead position, k_B the Boltzmann constant and T the temperature in Kelvin.

3 Local temperature sensing in OT with dual-sided heating approach

To compute the temperature at the position of the bead, the equipartition method, given by eq. (3.1), was combined with the drag force method. In the drag force method, a flow is exerted on the bead by moving the flow cell with a piezoelectric stage, while keeping the bead static with the trap. This flow induces a force on the bead causing the bead to displace from the center of the trap ($F_d = \kappa\Delta x$) [14, 15]. The force, experienced by the bead, depends on the velocity (ν) of the flow, the radius of the bead (R), and the viscosity of liquid, in this study water, around the bead ($\eta(T)$). This relationship is described by Stokes' law:

$$F_d = \kappa\Delta x = 6\pi R\eta(T)\nu \quad (3.2)$$

with the temperature-dependent viscosity of water ($\eta(T)$) given by eq. (3.3) [12], where T is the temperature in Kelvin.

$$\eta(T) = 10^{\frac{1.2372(293.15-T) - 0.001053(T-293.15)^2}{T-168.15}} - 2.999 \quad (3.3)$$

Equation (3.1) and eq. (3.2) can be rewritten to solve for the trap stiffness and set equal; this gives eq. (3.4a). This can then be rewritten into eq. (3.4b), which gives us the temperature-dependent viscosity on one side and an experimentally determined constant multiplied by the temperature on the other side. The equation was solved with a self-written python script, using the function "fsolve".

$$\frac{k_B T}{\langle x^2 \rangle} = \frac{6\pi R\eta(T)\nu}{\Delta x} \quad (3.4a)$$

$$\eta(T) = \frac{k_B \Delta x}{6\pi R\nu \langle x^2 \rangle} T \quad (3.4b)$$

3.2.8 Data acquisition and analysis of the E-DF method

To compute the temperature with the E-DF method, a bead was trapped, moved to a position in the flow cell ~ 2 mm away from the thermocouple and moved upwards to the center (in height) of the flow channel. Then, before bead recording, the detection laser was aligned by the AOD-sweep method (section 2.4.1), the light of the room was switched off and I left the room. This ensured accurate bead recording and eliminated (heat) vibrations from me and the light.

3.2 Materials and methods: our design

For the equipartition method, the bead position was recorded in voltage at a frequency of 100 kHz for a duration of 3 s. Subsequently, the recorded voltage data was converted to nanometers using the position calibration. To reduce low-frequency noise in the equipartition method, the data was divided into 300 sub-data sequences, each lasting 0.1 s. The equipartition stiffness calculation involved computing the variance $\langle x^2 \rangle$ from the median value of the variances obtained from all the 0.1 s sub-data sequences of bead positions.

As for the drag force method, the bead position was recorded for 2 s, while the piezoelectric stage moved the flow cell at a constant speed along the x- or y-axis at a frequency of 2 Hz. Except for the laser-induced heating experiment, the amplitude of the stage movement was increased from 10 μm to 30 μm in increments of 5 μm , resulting in velocities ranging from 40 $\mu\text{m/s}$ to 120 $\mu\text{m/s}$. For the laser-induced heating experiment, the amplitude of movement was adjusted according to the laser power. The recorded bead position data was then converted to nanometers and used to compute the drag force. This analysis was done for each of the four measurements, computing four temperatures. The average of those temperatures was plotted with the standard deviation (error-bar).

If desired this method can be used to compute the temperature directly after each measurement. Giving the temperature ~ 5 min after recording bead positions.

3.2.9 Equipartition method + power spectrum method (E-PS method)

The equipartition method can also be combined with the power spectrum method [15, 16]. This method is, like the drag force method, dependent on the viscosity of the surrounding liquid. In the power spectrum method, the vibrations of a trapped bead due to Brownian motion are computed in the frequency domain (from 100 Hz to 5000 Hz). Plotting the intensities of the vibrations against frequency results in a Lorentzian shaped power spectrum with corner (roll-off) frequency f_c , see eq. (3.5).

$$f_c = \frac{\kappa}{2\pi\gamma_0} \quad (3.5)$$

With κ the trap stiffness, γ_0 Stoke's friction coefficient, which is given by

3 Local temperature sensing in OT with dual-sided heating approach

$\gamma_0 = 6\pi\eta(T)R$. After solving for the trap stiffness, eq. (3.1) and eq. (3.5) were rewritten into eq. (3.6a) and solved for the temperature-dependent viscosity (eq. (3.6b)). This equation has the same form as eq. (3.4b) and can also be solved with a self-written python script using the function “fsolve”.

$$\frac{k_b T}{\langle x^2 \rangle} = \frac{f_c}{2\pi 6\pi\eta(T)} \quad (3.6a)$$

$$\eta(T) = \frac{k_B}{12\pi^2 R f_c \langle x \rangle} T \quad (3.6b)$$

3.2.10 Data acquisition E-PS method

The E-PS method was analyzed from the same data set as the E-DF method (section 3.2.8). However, the E-PS method only requires the data from the position calibration and the Brownian motion. The analysis of $\langle x^2 \rangle$ is the same as for the E-DF method. The roll-off frequency of the power spectrum method was determined with the matlab script from Tolić-Nørrelykke et al. [16]. The temperature for each measurement could then be computed with eq. (3.6b) and the average of the four temperatures was plotted with the standard deviation (error-bar).

3.2.11 TEM (bead size)

Bead size plays an important role in the temperature determination. A decrease of $0.5\ \mu\text{m}$ in bead radius decreases the temperature by $\sim 2^\circ\text{C}$ at room temperature for the E-DF method and E-PS method. The beads were imaged with a **t**ransmission **e**lectron **m**icroscope (TEM) and bead radius was measured in Fiji. The average bead radius was $0.92 \pm 0.01\ \mu\text{m}$, rather than the expected $0.965\ \mu\text{m}$.

3.3 Results and discussion

3.3.1 Confirming uniform heating of our flow cell designs

Prior to testing our heating system and temperature determination method, we needed to confirm that our flow cell design uniformly heats. A thermal

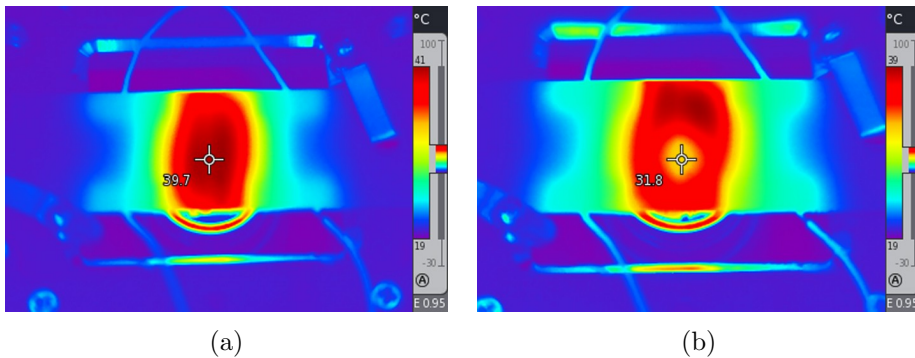


Figure 3.3: **Thermal images of copper heating flow cell.** a) Our self-made copper flow cells showed a minor temperature gradient. b) Bringing the heated copper flow cell in contact with the objective at room temperature, caused a significant decrease in temperature.

camera was used to image the temperature at the surface of the flow cell. It can be seen in fig. 3.3a that our self-made copper flow cell has a minor temperature gradient along the x- and y-axis. However, this gradient will be negligible for the nanometer displacements generally used in optical tweezers. Bringing the flow cell in contact with the objective, fig. 3.3b, demonstrated a significant drop in temperature. The flow cell temperature not in direct contact with the objective is much higher, flow cell dimensions are therefore limited by the size of the objective and objective heating is installed.

The commercially available ITO glass showed uniform heating between the electrodes, as can be seen in fig. 3.4, and is further tested as heating system.

3.3.2 The use of water vs. 'substitute oil' on water immersion objective

A water immersion objective in an optical tweezers setup is advantageous, as it enables to measure deep into the solution. Whereas the alternative, an oil immersion objective, is limited by spherical aberrations. They arise due to the refractive index mismatch between the immersion oil and the aqueous medium and can therefore only measure up to a few micrometers

3 Local temperature sensing in OT with dual-sided heating approach

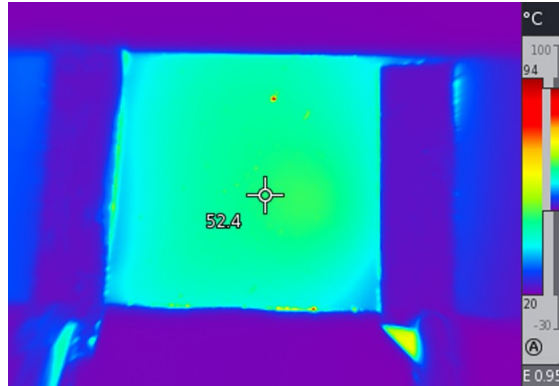


Figure 3.4: **Uniform heating between the electrodes was confirmed with the thermal camera.**

above the coverslip [17]. However, the water immersion objective on our setup imposes a challenge, because water evaporates and even quicker at higher temperatures. After 15 minutes at 50 °C, experiments were compromised due to water evaporation. To avoid evaporation and the use of an oil immersion objective, water was replaced by an oil based immersion (Immersol™W (2010)) that has a similar refractive index as water and is suitable for objectives.

The two immersions, water and the substitute oil, were compared during experimentation. The experiment tested the effect of immersion upon heating. To compare, our novel heating system was used to heat the flow cell from below and above (hereafter, double sided heating) and compared by two thermocouples; one inside the NOA strip, which was ~ 2 mm from the trap focus, and one inside the liquid of the channel, which was at the position of the trap. The channel was filled with ultrapure water, and the trapping and detection lasers were deactivated. The double sided heating system can heat equally from above and below up to 38 °C. After that, the temperature was increased by the ITO (above), while the objective (below) was kept at 38 °C. Temperature measurements were performed at three heights: 20 μ m above the flow channel surface (bottom), at the flow channel's center, or 20 μ m below the top surface.

Figure 3.5a depicts the disparity in ITO power required to achieve 50 °C

3.3 Results and discussion

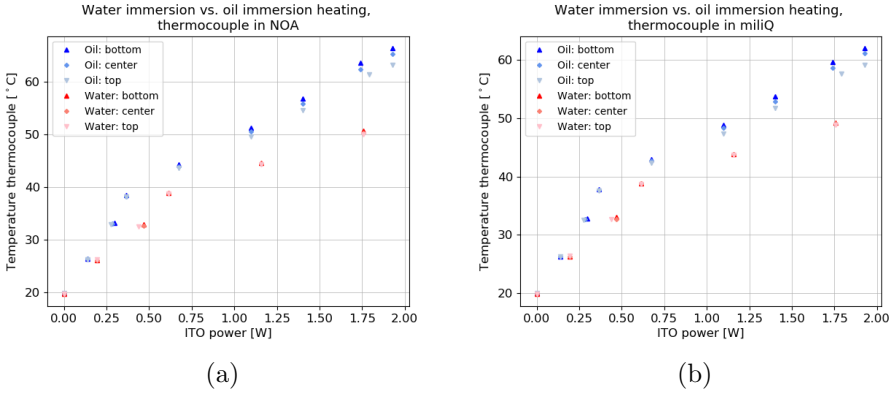


Figure 3.5: **Flow cell temperature for water and oil substitute on objective.** Temperature measured by a thermocouple in the NOA81 (~ 2 mm from trap focus) at different heights ($20 \mu\text{m}$ above bottom coverslip, center of the channel and $20 \mu\text{m}$ below top coverslip) in the flow channel with water or oil on the water immersion objective.

for water and oil substitute immersion. Specifically, achieving 50°C necessitated 1.76 W for water and 1.10 W for the oil substitute. This difference can be explained by the distinction in thermal conductivity of both materials. Water is a better thermal conductor than oil, and since the objective is 12°C below the desired temperature, the ITO needs to compensate the heat flux going through the solution to reach the objective.

An advantage of water usage, as opposed to the oil substitute, is the smaller effect on the temperature at the center of the flow channel upon changing focal height. Changing the focal height causes a change in the thickness of water/substitute oil between the objective and the flow cell. Focusing at the bottom of the flow cell gives a thicker layer of water/oil substitute than focusing at the top, see fig. 3.6. This and the difference in thermal conductivity explains the larger spread in temperature measured at the center of the flow channel, when focusing at the top compared to focusing at the bottom.

Due to evaporation and the high power required to heat, all experiments are conducted with the oil substitute.

3 Local temperature sensing in OT with dual-sided heating approach

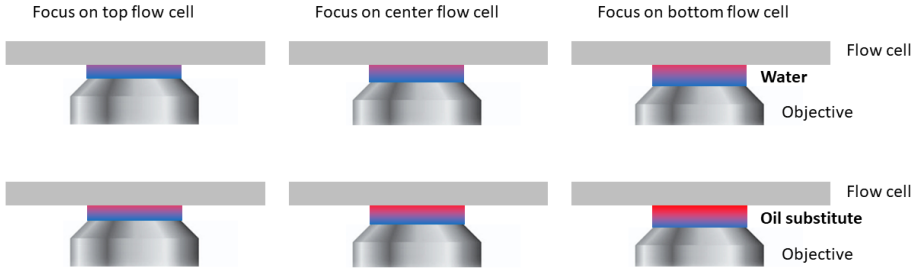


Figure 3.6: **Change in distance between flow cell and objective upon changing the focal height.** To change the focal height in the flow cell, the objective is moved down- or upwards. This movement increases or decreases, respectively, the distance between the flow cell and the objective. When ITO flow cell and objective temperature do not match, this affects the temperature gradient in the immersion used on the objective (water in top figures, and substitute oil in bottom figures). This temperature gradient is indicated by the transition from red (warm) to blue (cold) in the immersion layer.

3.3.3 Impact of laser heating

Laser-induced heating is a widely discussed concern in optical tweezers [7, 12, 14]. Undesired or unknown heating will influence the measurement and results. For instance, enzymatic activity is highly dependent on temperature [18–22] and force measurements rely on temperature through the stiffness of the trap.

The effect of laser-induced heating at the position of the bead was tested by our novel E-DF and E-PS methods and compared them to the temperature measured by a thermocouple in the NOA strip and a thermocouple in the substitute oil (both with a distance of about 2 mm to the trapped bead). Concurrently, the power of the trap laser emanating from the objective was measured directly after the objective, resulting in a power range of 10.1 to 83.0 mW. The laser-induced heating was determined in our ITO flow cell, but also in a flow cell constructed with standard soda lime microscope glass slide (Corning[®]; Micro Slides, Plain), called regular flow cell, to be able to compare our results with literature.

3.3 Results and discussion

The laser-induced heating in a regular flow cell computed by the E-DF method and measured by the thermocouples is shown in fig. 3.7a and for the E-PS method shown in fig. 3.7b. The temperatures measured by the thermocouples are very close and indicate a rise in temperature of 1.1 ± 0.1 °C/100 mW. The E-PS method computed a temperature fall, this fall is most likely caused by the exclusion of high frequency vibrations in the power spectrum method, while the equipartition method takes them into account. The sensitivity to high frequency vibrations (signal-to-noise) is dependent on the stiffness of the trap and thus on the laser power. The E-PS method was found not to be valid to determine laser-induced heating in a regular flow cell. The temperature rise computed from the E-DF method indicates local heating of 2.8 ± 0.1 °C/100 mW. This result is comparable to the theoretically calculated value of Peterman et al. [12], which was 2.5 °C/100 mW for a polystyrene bead with diameter 1.84 μm in water, Ebert et al. [13] who found 1.3 °C/100 mW when no bead was trapped and the measured value of Català et al. [14] who found 1.9 °C/100 mW for a 0.58 μm polystyrene bead in water.

In the ITO flow cell, a much larger temperature rise is measured according to both methods and both thermocouples, see fig. 3.8a and fig. 3.8b. The thermocouples showed a rise of 2.2 ± 0.3 °C/100 mW. With the E-PS method this rise increased to 10.7 °C/100 mW, apparently the large temperature increase overruled the presumed signal-to-noise ratio caused by trap power. As expected, the rise found by the E-DF method was larger than the E-PS method. Now, heating of 14.4 °C/100 mW was computed. The discrepancy between the flow cell designs is most likely caused by the ITO layer, which partially absorbs the trap laser and converts it to heat, resulting in a much larger effect of the trap power on the temperature. To minimize this heating effect and control the temperature only with our heating system, we chose to continue with the lowest possible trap laser power. At the same time, the trap laser needs to be powerful enough such that the effect of the detection laser on the trapped bead is negligible.

It should be pointed out that laser-induced heating in the ITO flow cell can be reduced drastically by tuning the protocol of vapor deposited ITO to limit the concentration of free charge [23]. This results in a lower absorption of (near) infrared light. On the other hand, laser-induced heating can also be used to locally obtain even higher temperatures.

3 Local temperature sensing in OT with dual-sided heating approach

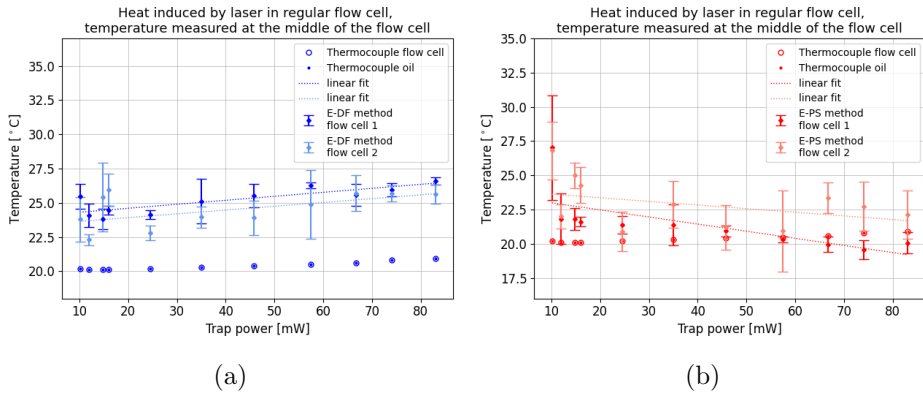


Figure 3.7: **Laser-induced heating in a regular flow cell.** The obtained temperature rise due to heat induced by the laser at different trap powers. The temperature at each trap power was measured by two thermocouples: one in the NOA strip and one in the substitute oil on the objective, both have a distance of about 2 mm to the trap focus. a) The temperature computed by the E-DF method (blue diamonds with error bars), with a linear fit (blue dotted line) for two flow cells. b) The temperature computed by the E-PS method (red diamonds with error bars), with a linear fit (red dotted line) for two flow cells.

3.3 Results and discussion

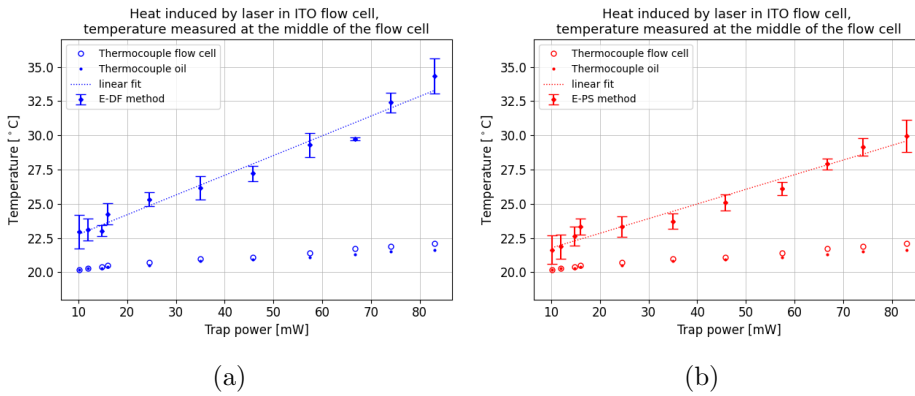


Figure 3.8: **Laser-induced heating in an ITO flow cell.** The obtained temperature rise due to heat induced by the laser at different trap powers. The temperature at each trap power was measured by two thermocouples: one in the NOA strip and one in the substitute oil on the objective, both have a distance of about 2 mm to the trap focus. a) The temperature computed by the E-DF method (blue diamonds with error bars), with a linear fit (blue dotted line). b) The temperature computed by the E-PS method (red diamonds with error bars), with a linear fit (red dotted line).

3 Local temperature sensing in OT with dual-sided heating approach

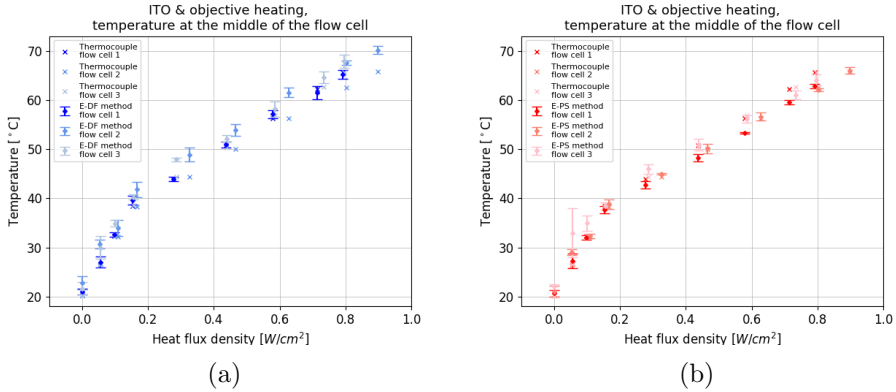


Figure 3.9: **Temperature rise in the flow cell upon double sided heating.** Heat flux density is obtained by the power supplied to the ITO divided by the surface between the electrodes. The temperature is measured by a thermocouple in the NOA strip, (a) computed by the E-DF method (blue diamonds with error bars), and (b) computed by the E-PS method (red diamonds with error bars) at the center of the flow channel in three different flow cells.

3.3.4 Double sided heating

The flow cell can be heated to at least $\sim 70^\circ\text{C}$ when both heating systems are employed, see fig. 3.9. For the temperature range $20\text{-}38^\circ\text{C}$, the flow cell was equally heated from both sides. After 38°C , the temperature was increased by the ITO. This can be seen by the change in slope from 0 to 0.2 W/cm^2 (20 to 38°C) and from 0.25 to 0.95 W/cm^2 (44 to 70°C) in fig. 3.9. The heat flux density is the power ($P = U * I$, with U the voltage and I the current) applied to the ITO divided by the surface between the electrodes. The surface was estimated from ImageJ measurements of photos of the flow cells.

The temperature rise computed from the E-DF method, fig. 3.9a, and the E-PS method, fig. 3.9b show a good correlation to the temperature rise measured by the thermocouple. Nonetheless, the temperature increase from the E-PS method is less than the E-DF method. As mentioned before, the discrepancy is expected to arise from the exclusion of

high frequency vibrations in the power spectrum method, but not in the equipartition method.

The heat flux density in the three different flow cells tested here show a good correlation. Even though the flow cells were handmade, and slight differences in channel height, trap to thermocouple distances, and approximations in the measured surface between the electrodes were present. This heating technique showed to be consistent. Therefore, the required heat flux densities and temperatures may be coupled, speeding up and easing the heating protocol.

3.3.5 Objective heating

In our optical tweezers setup any flow cell can be heated by the objective heating system. This technique has been utilized by others as well. Mao et al. [6] used copper jackets with fluid circulation channels to heat (or cool) their sample and Mahamdeh and Schäffer [7] used a heating foil around the objective to stabilize and control the temperature. They both have an optical tweezers setup with an objective below and above their sample, rather than an objective-condenser system (as our setup has). Heating the condenser is not as convenient as heating an objective, because the condenser is bigger, the casing is made of plastic and the working distance (distance between the condenser and the sample) is larger. Heating will therefore be even less effective. This and the recommendation to keep the temperature of the objective below 40 °C limits the heating range of the sample.

Nonetheless, small temperature increases may be desirable. The objective heating system was therefore characterized by itself. The temperature rise obtained is shown in fig. 3.10. The thermocouple positioned in the substitute oil logically shows the steepest temperature rise. Temperature computed from our methods show the least steep temperature rise. This is presumably due to the distinction in thermal conductivity of water and NOA and the design of the objective with the position of the thermocouple and the bead. The thermocouple is positioned above the conductive metal part of the objective, whereas the bead is trapped above the less conductive optical part of the objective. The discrepancy between obtained temperature at room temperature (20 °C) is caused by laser-induced heating.

3 Local temperature sensing in OT with dual-sided heating approach

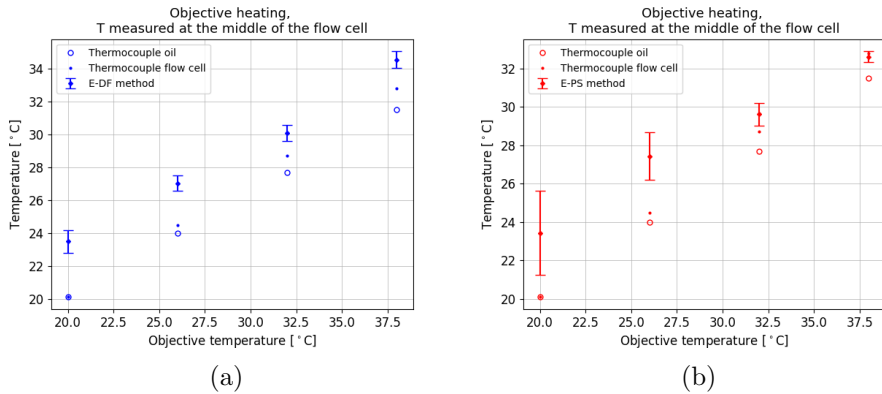


Figure 3.10: **Temperature rise in the flow cell by objective heating.** The temperature set on the PID controller was compared to the temperature measured by two thermocouples: one in the NOA strip and one in the substitute oil on the objective, both have a distance of about 2 mm to the trap focus. In (a) the PID controller temperature was also compared to the temperature computed by the E-DF method (blue diamonds with error bars), with a linear fit (blue dotted line). In (b) the PID controller temperature was compared to the temperature computed by the E-PS method (red diamonds with error bars), with a linear fit (red dotted line).

The maximum average temperature computed from the bead recordings is approximately 33 °C in the flow cell. Concurrently, the objective has a temperature of 38 °C. A discrepancy between the flow cell temperature and the set temperature at the objective was expected, since heat was only generated from below. Due to the mismatch in temperature at the top and bottom of the flow cell and the thickness change of the substitute oil, a change in focal height will cause a change in temperature. This will complicate temperature sensitive measurements. Besides that, the equilibration and stabilization time after temperature adjustment is long (about 20 mins) and it generates a drift in the focal height ($\sim 10 \mu\text{m}$ for a 6 °C change in temperature).

3.3.6 ITO heating

When objective heating is not a possibility, the flow cell can be heated by the ITO system. In this system, the heat source is much closer to the trapped bead. Reducing the thermal drift, decreasing equilibration and stabilization time, and the temperature limitation is not applicable. This allowed us to reach a temperature of 68 °C in the flow cell, see fig. 3.11.

The temperature increase computed by the E-DF method is comparable to the measured temperature by the thermocouple, see fig. 3.11a. The temperature increase measured by the E-PS method is slightly lower. The discrepancy is expected to be caused by the exclusion of high frequencies in the power spectrum method, but not in the equipartition method.

Even though this technique works well by itself, is quicker than objective heating, and has a smaller focal drift (roughly half of what is observed by objective heating)), combining it with objective heating has an advantage. The power (or heat flux density) required is lower and up to 38 °C, when the flow cell can be equally heated with the ITO and objective, the temperature at the center of the flow cell remains constant upon changes in focal height and at higher temperatures the effect will be smaller.

3.3.7 Temperature determination at different heights

In an attempt to confirm the absence of a temperature gradient within the liquid of the flow cell, the local temperature was measured at different heights in the flow cell. However, different heights are associated to

3 Local temperature sensing in OT with dual-sided heating approach

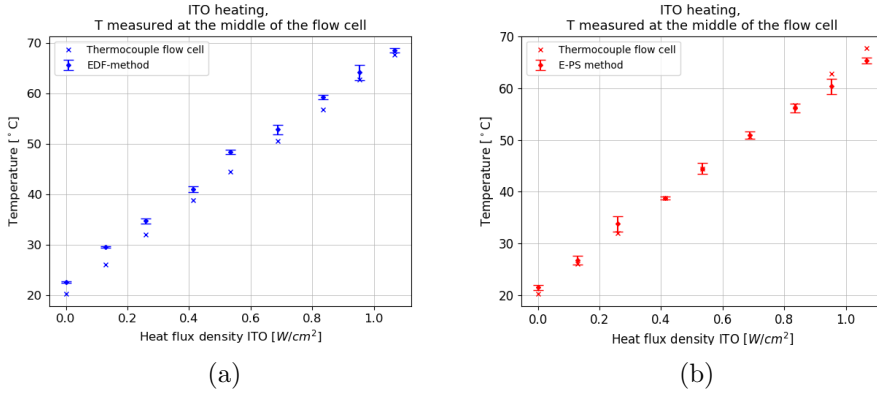


Figure 3.11: **Temperature rise at the center of the flow cell upon ITO heating.** Heat flux density is obtained by the power supplied to the ITO divided by the surface between the electrodes. Temperature measured by the thermocouple in the NOA strip and a) computed by E-DF method (blue diamonds with error bars) or b) computed by E-PS method (red diamonds with error bars).

different thicknesses of the oil substitute, thereby changing the insulating layer between the warmer flow cell and colder objective.

The local temperature at the bottom (20 μm above the flow channel surface), at the center, and at the top (20 μm below the top of the flow channel) is computed by the E-DF and E-PS method for double sided heating, fig. 3.12. A change in slope can be observed between 22-42 $^{\circ}\text{C}$ and 47-68 $^{\circ}\text{C}$ as caused by the limited temperature of the objective. The slope change occurred after 40 $^{\circ}\text{C}$, because there was no thermocouple present during the experiment. The ITO power required to match the objective temperature had to be approximated. The ITO power is not converted to heat flux density, because there was no photo taken of the flow cell. Nonetheless, it can be seen that up to 60 $^{\circ}\text{C}$ the temperature computed at all heights is comparable. At higher temperatures, the temperature might start to be affected by a change in focal height as observed in fig. 3.12a but not in fig. 3.12b.

When the flow cell is solely heated by the ITO, the temperature difference between the bottom and the top of the flow cell is larger. The effect of

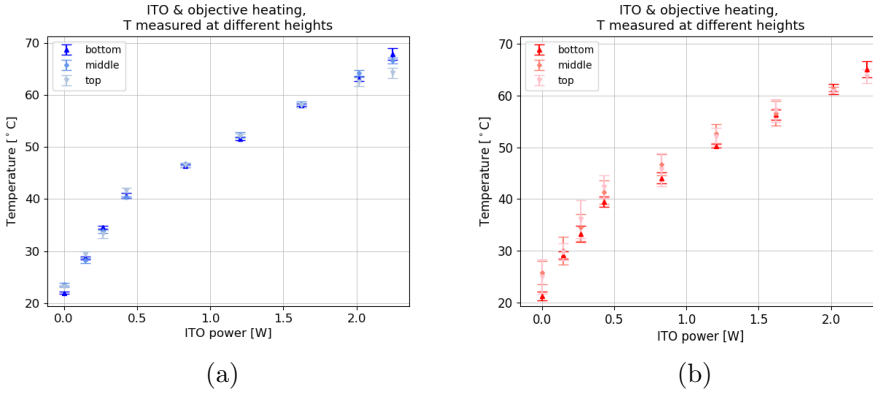


Figure 3.12: **Effect of focal height on temperature for double sided heating, i.e. ITO and objective heating.** a) Temperature computed by E-DF method (blue diamonds with error bars) at the bottom, center, and top of the flow channel. b) Temperature computed by E-PS method (blue diamonds with error bars) at the bottom, center, and top of the flow channel.

the larger temperature difference on the local bead temperature has been obtained for ITO heating, see fig. 3.13. However, a local change at the bead position was not apparent. This indicates that locally at the position of the bead there is no (apparent) change in temperature at different flow cell heights.

Even though, the ITO heating system can achieve the same high temperature as double sided heating, using double sided heating is recommended. This heating system significantly reduces the power required to obtain 70 °C and it minimizes the temperature discrepancy between the top of the flow channel and the objective.

3.4 Conclusion

In this work, we demonstrated that our heating system, which combines ITO and objective heating, is capable of heating the sample to temperatures as high as 70 °C. The temperature was measured by a thermocouple mounted in our heating flow cell and was computed by our newly proposed

3 Local temperature sensing in OT with dual-sided heating approach

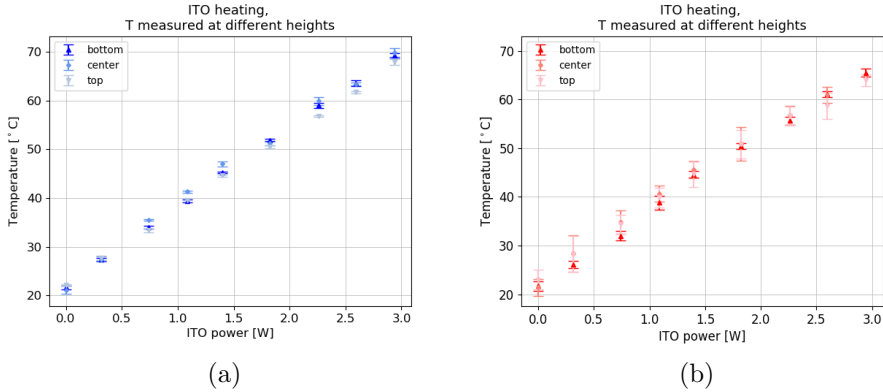


Figure 3.13: **Effect of focal height on temperature for ITO heating.** a) Temperature computed by E-DF method (blue diamonds with error bars) at the bottom, center, and top of the flow channel. b) Temperature computed by E-PS method (red triangles with error bars) at the bottom, center, and top of the flow channel.

methods, which uses a trapped bead to locally determine temperature. The E-PS method computes the temperature by comparing the thermal fluctuations of the bead with the vibrational frequencies. During data analysis the high vibration frequencies had to be excluded, which presumably caused the method to be less sensitive to temperature changes and could not determine laser-induced heating due to this. The E-DF method computes the temperature by comparing thermal fluctuations of the bead with bead displacements induced by a flow. This method showed temperature increases comparable to those obtained by a thermocouple. Besides that, it demonstrated that it could determine the heating effect of the trapping laser. We therefore conclude that our method is a valid technique to determine the local temperature.

Real-time temperature determination could be of great value during experimentation. Our method has this potential, with only a computational delay of about 5 minutes, it can determine the local temperature. On the other hand, adding a thermocouple in the flow cell allows for viscosity-temperature dependent measurements. The thermocouple would be used to measure the change in temperature, while the trapped bead is used

3.4 Conclusion

to determine the viscosity. The thermocouple and ITO flow cell heating system is not limited to optical tweezers setups. The system can be used on other microscopy setups as well and can be used to study the effect of temperature on biological phenomena.

References

- (1) Amador, G. J.; van Dijk, D.; Kieffer, R.; Aubin-Tam, M.-E.; Tam, D. Hydrodynamic shear dissipation and transmission in lipid bilayers. *Proceedings of the National Academy of Sciences* **2021**, *118*, DOI: 10.1073/pnas.2100156118.
- (2) Dimova, R.; Pouligny, B.; Dietrich, C. Pretransitional Effects in Dimyristoylphosphatidylcholine Vesicle Membranes: Optical Dynamometry Study. *Biophysical Journal* **2000**, *79*, 340–356.
- (3) Chen, W.; Duša, F.; Witos, J.; Ruukonen, S.-K.; Wiedmer, S. K. Determination of the Main Phase Transition Temperature of Phospholipids by Nanoplasmonic Sensing. *Scientific Reports* **2018**, *8*, DOI: 10.1038/s41598-018-33107-5.
- (4) Frallicciardi, J.; Melcr, J.; Siginou, P.; Marrink, S. J.; Poolman, B. Membrane thickness, lipid phase and sterol type are determining factors in the permeability of membranes to small solutes. *Nature Communications* **2022**, *13*, DOI: 10.1038/s41467-022-29272-x.
- (5) Leake, M. C.; Wilson, D.; Gautel, M.; Simmons, R. M. The Elasticity of Single Titin Molecules Using a Two-Bead Optical Tweezers Assay. *Biophysical Journal* **2004**, *87*, 1112–1135.
- (6) Mao, H.; Arias-Gonzalez, J. R.; Smith, S. B.; Tinoco Jr., I.; Bustamante, C. Temperature Control Methods in a Laser Tweezers System. *Biophysical Journal* **2005**, *89*, 1308–1316.
- (7) Mahamdeh, M.; Schäffer, E. Optical tweezers with millikelvin precision of temperature-controlled objectives and base-pair resolution. *Optics Express* **2009**, *17*, 17190.
- (8) Kato, H.; Nishizaka, T.; Iga, T.; Jr., K. K.; Ishiwata, S. Imaging of thermal activation of actomyosin motors. *Proceedings of the National Academy of Sciences* **1999**, *96*, 9602–9606.
- (9) Mondal, D.; Bandyopadhyay, S. N.; Mathur, P.; Goswami, D. On-the-Fly Calibrated Measure and Remote Control of Temperature and Viscosity at Nanoscale. *ACS Omega* **2018**, *3*, 12304–12311.

- (10) Mondal, D.; Mathur, P.; Goswami, D. Precise control and measurement of solid–liquid interfacial temperature and viscosity using dual-beam femtosecond optical tweezers in the condensed phase. *Physical Chemistry Chemical Physics* **2016**, *18*, 25823–25830.
- (11) Joule, J. P. On the production of heat by voltaic electricity. *Abstracts of the Papers Printed in the Philosophical Transactions of the Royal Society of London* **1843**, *4*, 280–282.
- (12) Peterman, E. J. G.; Gittes, F.; Schmidt, C. F. Laser-Induced Heating in Optical Traps. *Biophysical Journal* **2003**, *84*, 1308–1316.
- (13) Ebert, S.; Travis, K.; Lincoln, B.; Guck, J. Fluorescence ratio thermometry in a microfluidic dual-beam laser trap. *Optics Express* **2007**, *15*, 15493.
- (14) Català, F.; Marsà, F.; Montes-Usategui, M.; Farré, A.; Martín-Badosa, E. Influence of experimental parameters on the laser heating of an optical trap. *Scientific Reports* **2017**, *7*, DOI: 10.1038/s41598-017-15904-6.
- (15) Visscher, K.; Gross, S. P.; Block, S. M. Construction of Multiple-Beam Optical Traps with Nanometer-Resolution Position Sensing. *IEEE Journal of Selected Topics in Quantum Electronics* **1996**, *2*, 1066–1076.
- (16) Tolić-Nørrelykke, I. M.; Berg-Sørensen, K.; Flyvbjerg, H. MatLab program for precision calibration of optical tweezers. *Computer Physics Communications* **2004**, *159*, 225–240.
- (17) Sung, J.; Sivaramakrishnan, S.; Dunn, A. R.; Spudich, J. A. In *Methods in Enzymology*; Elsevier: 2010; Chapter 14, pp 321–375.
- (18) O'malley, J. J.; Ulmer, R. W. Thermal stability of glucose oxidase and its admixtures with synthetic polymers. *Biotechnology and Bioengineering* **1973**, *15*, 917–925.
- (19) Yumoto, I.; Ichihashi, D.; Iwata, H.; Istokovics, A.; Ichise, N.; Matsuyama, H.; Okuyama, H.; Kawasaki, K. Purification and Characterization of a Catalase from the Facultatively Psychrophilic Bacterium *Vibrio rumoiensis* S-1 (T) Exhibiting High Catalase Activity. *Journal of Bacteriology* **2000**, *182*, 1903–1909.

3 Local temperature sensing in OT with dual-sided heating approach

- (20) Daniel, R. M.; Danson, M. J. A new understanding of how temperature affects the catalytic activity of enzymes. *Trends in Biochemical Sciences* **2010**, *35*, 584–591.
- (21) Cordova, J. C.; Olivares, A. O.; Shin, Y.; Stinson, B. M.; Calmat, S.; Schmitz, K. R.; Aubin-Tam, M.-E.; Baker, T. A.; Lang, M. J.; Sauer, R. T. Stochastic but Highly Coordinated Protein Unfolding and Translocation by the ClpXP Proteolytic Machine. *Cell* **2014**, *158*, 647–658.
- (22) Wu, Q.-Y.; Wei, F.; Zhu, Y.-Y.; Tong, Y.-X.; Cao, J.; Zhou, P.; Li, Z.-Y.; Zeng, L.-Y.; Li, F.; Wang, X.-Y.; Xu, K.-L. Roles of amino acid residues H66 and D326 in the creatine kinase activity and structural stability. *International Journal of Biological Macromolecules* **2018**, *107*, 512–520.
- (23) Zhang, D.; Najafi, M.; Zardetto, V.; Dörenkämper, M.; Zhou, X.; Veenstra, S.; Geerligs, L.; Aernouts, T.; Andriessen, R. High efficiency 4-terminal perovskite/c-Si tandem cells. *Solar Energy Materials and Solar Cells* **2018**, *188*, 1–5.

Chapter 4

Studying the mechanical properties of FtsH

The mechanical properties of FtsH, such as translocation mechanism and pulling force, have not yet been fully unraveled. In an attempt to assess these properties, a dual trap optical tweezers assay was constructed to study the recently successfully purified full-length (biotinylated) *Aquifex aeolicus* FtsH (aaFtsH). The optical tweezers assay was initially comparable to the one that was developed for *E. coli* ClpXP and ClpAP. However, unlike *E. coli* ClpXP and ClpAP, aaFtsH was not active at room temperature, but required a temperature of at least 53 °C. This complicated the optical tweezers study, caused aggregation, and affected the spontaneous unfolding rate of the substrate. Due to these challenges, the mechanical properties of aaFtsH has not (yet) been obtained.

4.1 Introduction

After successful purification of full-length aaFtsH, its mechanical properties could be studied with optical tweezers. To study the translocation mechanism (i.e. step size and rate, and the pulling power (stalling force)) of aaFtsH, a construct similar to the one used for the AAA+ proteases ClpXP [1–5] and ClpAP [3, 5] (reviewed in [6, 7]) is employed. In the ClpXP experiments, two optical traps, two beads with different size, a dsDNA linker, a Halo domain, a multidomain degron-tagged substrate (generally four (mutated) titin I27 titin domains), and ClpXP were used, see fig. 4.1. Each trap contains one bead and the beads are linked through a $\sim 1\ \mu\text{m}$ long dsDNA linker, a Halo domain, a multidomain degron-tagged substrate, and the protease. The dsDNA linker creates enough distance between the two traps, to ensure the absence of crosstalk. The Halo domain covalently links to the dsDNA linker and to the multidomain degron-tagged substrate. The protease is linked to the other bead and interacts with the substrate. Taking into account the length of all components, the traps were positioned such that the bead displacements were within the passive force-clamp region [8], as described in section 1.3.1. By measuring the position of the beads at a high spatial-temporal resolution, the translocation step size and velocity could be determined. The translocation stalling force of ClpXP was determined by repeating the same measurement at different trap stiffness, thereby changing the applied (stretching) force on the beads. At increasing forces the translocation rate decreased, extrapolating this decrease determined the stalling force.

To study aaFtsH this same construct was employed, with some modifications in experimental conditions. The modifications included the addition of zinc, as aaFtsH is a metalloprotease which requires zinc; the replacement of the reducing agent, as it aggregated with zinc; and weak noncovalent immobilization of the substrate-bound bead to the glass surface, rather than being tethered to the glass surface by a DNA linker with glass binding peptide aptamer [1]. But the most significant modifications was the increase in temperature. Proteolytic activity of aaFtsH requires a temperature of at least $53\ ^\circ\text{C}$, therefore all experiments were performed at a temperature between $53\text{--}60\ ^\circ\text{C}$. This temperature could be reached by our newly designed heating flow cells, as described in section 3.2.4 and

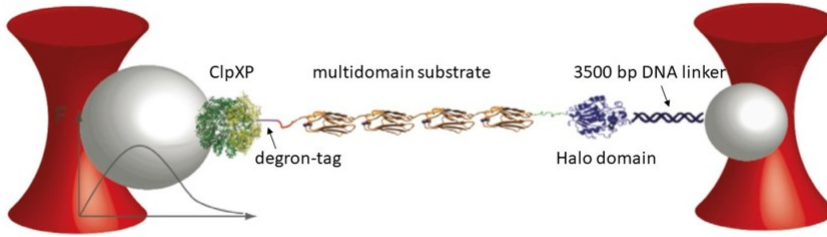


Figure 4.1: **Experimental setup of ClpXP degradation study.** The left bead is trapped in the weak trap and pulled into the passive force region of the trap, while being linked to the right bead that is trapped in (the linear region of) the strong trap. The link consists of ClpXP, a four multidomain degron-tagged substrate, a Halo domain, and a DNA linker. Figure taken and modified from [2].

demonstrated in section 3.3. Unfortunately, the high temperature caused some components of the experimental buffer to aggregate. These components were excluded as the aggregates interfere with the bead recording. The increase in temperature affected not only the buffer components, but also the stability of the substrate ($I27^{V13P}$ and $I27^{V15P}$), the persistence length of dsDNA-linker, and possibly the stability of the Halo domain. The high temperature significantly affected and complicated the aaFtsH experiment.

The chance of spontaneous unfolding (unfolding not induced by aaFtsH) when a mechanical load is applied to the substrate domains ($I27^{V13P}$, $I27^{V15P}$, and the Halo domain), increases with increasing temperature [9]. These spontaneous unfolding events were found to occur at low force (3-5 pN) and at temperatures of 21-42 °C for mutated I27 modules [9]. It is therefore possible that in our aaFtsH study, recorded unfolding events could also be spontaneous unfolding events rather than induced by aaFtsH. The spontaneous unfolding events would result in unfolding events without translocation and degradation. This would be the case if a module or domain that is not in contact with aaFtsH unfolds. It could also cause substrate degradation not preceded by an unfolding event, this would be the case when a module or domain (that was not in contact with aaFtsH) unfolded before bead recording. At the same time, FtsH might be a weak

4 Studying the mechanical properties of FtsH

unfoldase and not capable of degrading a more stable form of I27.

Recorded unfolding events of I27^{V13P} or I27^{V15P} were compared to the extension predicted by the worm-like chain (WLC) model (eq. (1.2)), with contour length 29 nm [10] and persistence length 0.8 nm [11]. However, it was found previously that the unfolding pathway of I27^{V13P} (C-terminal ssrA-tag) and I27^{V15P} (N-terminal ssrA-tag) was affected by the presence of a protease. During a ClpAP degradation study it was observed that some unfolding events included an intermediate state [10]. Interestingly, this observed (protease induced) intermediate state differs from the intermediate state found by chemical or mechanical denaturant studies [9, 11–15].

The mechanical stability of the Halo domain is also of importance as this domain has a folded and unfolded state. The stability of the Halo domain has been studied in conjugation with four mutated I27 modules by AFM [16]. The unfolding events of the Halo domain were distinguishable from I27 unfolding events by the unfolding extension length. This has also been reported by ClpXP optical tweezers studies [1, 2, 10, 17]. The force required to unfold the Halo domain was found to be lower (about 2/3) of that found for the I27 modules [16]. It is therefore likely that at the experimental temperature of 53–60 °C and an applied stretching force of 1–21 pN, spontaneous unfolding of the Halo domain occurs. The extension upon unfolding can be described by the WLC model with contour length 67 nm and persistence length 0.6 nm [16].

The dsDNA-linker will be stretched during the experiment. The force extension relation of dsDNA has been studied [18] and can be described by the extended version of the WLC model:

$$F = \frac{k_B T}{L_p} \left(\frac{1}{4(1 - x/L_c + F/K_0)^2} - \frac{1}{4} + \frac{x}{L_c} - \frac{F}{K_0} \right) \quad (4.1)$$

for $F < 60$ pN, with K_0 the elastic modulus which is expected to be 1050 pN [18]. The persistence length of dsDNA is dependent on temperature and decreases from ~ 50 nm at room temperature to about 38 nm at 55 °C [19]. The contour length is 0.338 nm/bp $\times 3500$ bp = 1183 nm and has not been reported to change upon temperature [19].

The lowest force computed from aaFtsH experiments was about 1.5 pN. At this low force the bead, DNA, folded Halo domain, four folded I27^{V13P}

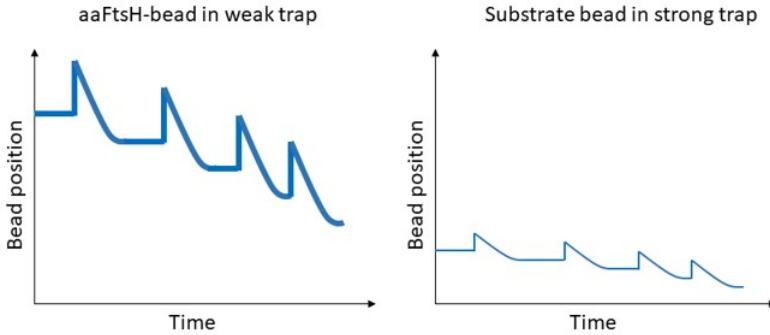


Figure 4.2: **Expected bead recordings of unfolding and translocation events, when the beads are in the linear region of the trap.** The figures demonstrate the expected unfolding and translocation patterns over time for the aaFtsH-bead in the weak trap (right figure) and the substrate-bound bead in the strong trap (left figure). In the right figure, the trap is weaker, thus the bead displacements are larger than for the substrate-bound bead in the strong trap (right figure). This is also depicted by linewidth (the Brownian motion in a weaker trap gives a larger variation in bead position) and by initial position of the bead (with the x-axis representing the center of the trap, the substrate bound bead is closer to the trap center than the aaFtsH-bead).

or I27^{V15P} modules, aaFtsH, and the second bead have a combined length of 2174.3 nm ($625 + 1015 + 3.3 + 4 * 4.4 + 13.4 + 500$ nm) [1, 12, 20]. The distance between the two traps should therefore be larger than 2174.3 nm. This ensures that the beads are pulled away from the center of the trap and ensures the ability to observe unfolding events. In a successful recording unfolding and translocation are present, with unfolding as a rapid change in bead position away from the center of the trap and translocation as a slow, gradual change in bead position towards the center of the trap. A schematic representation of the expected bead displacements is shown in fig. 4.2.

Bead recordings have been obtained for the substrate consisted of I27^{V13P} and for I27^{V15P}. Unfortunately, no recording was suitable to determine the mechanical properties of aaFtsH.

4.2 Materials and Methods

4.2.1 Substrate expression and purification

To construct the DNA-HaloEnzyme-[I27^{V13P}]_{x4}-ssrA or -[I27^{V15P}]_{x4}-ssrA substrate, the proteins HaloEnzyme, [I27^{V13P}]_{x4}-ssrA, and [I27^{V15P}]_{x4}-ssrA were expressed in *E. coli* and purified as described in the following paragraph. A 3500 base pair DNA with HaloTag was made and purified, mostly as previously reported [1]. Except that, it was possible to directly order the DNA-HaloTag oligonucleotide and thus not necessary to halogenate the DNA ourselves. The ordered DNA-HaloTag oligonucleotides were directly used in the PCR reactions.

The titin multidomains [I27^{V13P}]_{x4}-ssrA and [I27^{V15P}]_{x4}-ssrA consisted of four titin I27 repeats and were expressed in *E. coli* BL21(DE3) pLysS cells containing the expression plasmid of choice. The protein expression was induced for 3 hours with 1 mM IPTG (isopropyl β -D-thiogalactopyranoside). Cells were harvested and resuspended in lysis buffer (50 mM KPi (key performance indicators) pH 8.0, 1 M NaCl, 1 mM β -mercaptoethanol, 10 % glycerol; 0.1 % igepal and one dissolved protease inhibitor cocktail tablet (Roche)).

Cells were lysed by sonication and the lysate was clarified by centrifugation (37.000 rpm, 30 mins). Imidazole was added to the supernatant to a final concentration of 20 mM. This was then loaded on a pre-equilibrated Ni-column (nickel column; 50 mM KPi pH 8.0, 1 M NaCl, 1 mM β -mercaptoethanol, 10 % glycerol, 20 mM Imidazole) and eluted with a gradient using the elution buffer (50 mM KPi pH 8.0, 1 M NaCl, 1 mM β -mercaptoethanol, 10 % glycerol, 500 mM Imidazole). Peak fractions were pooled and loaded on a Sephacryl-300 gel filtration column, equilibrated in GF-buffer (25 mM Tris pH 8.0, 150 mM NaCl, 5 mM β -mercaptoethanol, and 10 % glycerol). Fractions containing the protein of interest were flash-frozen in liquid nitrogen and stored at -80 °C.

4.2.2 aaFtsH expression and purification

AaFtsH-biotin was expressed in OverExpress C43 DE3 (Immunosource) cells with an additional BirA plasmid. Cells were grown at 37 °C and induced for 3 hours with 1 mM IPTG and supplemented with 0.1 mM bi-

otin. After induction, the cells were harvested by centrifugation (4.000 rpm for 20 mins). The cells were resuspended in lysis buffer (20 mM Tris pH 8.0, 300 mM NaCl, 1 Pierce Protease Inhibitor pill, EDTA-free (ethylenediaminetetraacetic acid free), DNase I), lysed by French press, where the unlysed cells were removed through centrifugation (24.000 rpm for 15 mins), and the membrane fractions were isolated (40.000 rpm for 3 h).

The membranes were resuspended in 20 mM Tris pH 8.0, 100 mM NaCl, 1 % LMNG (lauryl maltose neopentyl glycol), homogenized with a Dounce homogenizer, and allowed to resolubilize at 4 °C for 3 hours. The solution was diluted 1:1 with 20 mM Tris pH 8.0, 500 mM NaCl and spun down at 40.000 rpm. The supernatant was loaded on a pre-equilibrated Ni-column (20 mM Tris pH 8.0, 500 mM NaCl, 20 mM imidazole, 0.01 % LMNG, 1 mM β -mercaptoethanol) and the protein was eluted with a gradient using the elution buffer (20 mM Tris pH 8.0, 500 mM NaCl, 20 mM imidazole, 0.01 % LMNG, 1 mM β -mercaptoethanol). The peak fraction was collected and loaded on the pre-equilibrated Ni-column. The peak fraction containing aaFtsH was collected and protein concentration was determined through Nanodrop measurements.

4.2.3 The aaFtsH heating flow cell

The heating flow cell was constructed as described in section 3.2.4. The substrate was prepared by mixing 8.75 mg $[I27^{V13P}]x4$ -ssrA or $[I27^{V15P}]x4$ -ssrA with \sim 3150 ng DNA-HaloTag and incubated for \sim 24 hours at 37 °C. The aaFtsH-beads were prepared by centrifuging (2.000 rpm for 10 mins) streptavidin coated beads of diameter 1.00 μ m (Polyscience Inc.) and resuspending them in 150 μ L centrifuge filtered (5.000 rpm for 3 mins, 0.1 μ m) aaFtsH. The aaFtsH-bead solution was incubated for at least 3 hours, but no longer than 8 hours, on a moving plate at 4 °C.

The flow cell was functionalized by 100 μ g/mL bovine serum albumin (BSA) in phosphate buffered saline (PBS) with 1 mM tris(2-carboxyethyl)-phosphine (TCEP). Streptavidin beads of diameter 1.25 μ m (Spherotech Inc.) were introduced in the flow cell, and would weakly bound to the functionalized glass coverslip. After washing off the free floating beads by flowing in 80 μ L 100 μ g/mL BSA in PBS with 0.1 mM TCEP, the biotinylated DNA-HaloEnzyme- $[I27^{V13P}]x4$ -ssrA or $-[I27^{V15P}]x4$ -ssrA was introduced in the flow cell. The unbound substrate was then removed by flowing in

4 Studying the mechanical properties of *FtsH*

80 μL 100 $\mu\text{g}/\mu\text{L}$ BSA in PBS with 0.1 mM TCEP and 10 μL experimental buffer. The experimental buffer consisted of 12 $\mu\text{g}/\text{mL}$ β -casein, 1 mM TCEP, 25 μM zinc, 10 mM magnesium, 10 mM ATP (adenosine triphosphate), 0.5 mg/mL glucose oxidase, dissolved in 110 mM Tris pH 8.0.

The aaFtsH-beads were centrifuged twice (2.000 rpm for 4 mins, second time for 2 mins) and resuspended in 100 μL 100 $\mu\text{g}/\text{mL}$ BSA in PBS with 0.1 mM TCEP, to remove any unbound aaFtsH. The beads were again centrifuged (2.000 rpm for 2 mins), but now resuspended in 20 μL experimental buffer. The aaFtsH-beads were introduced in the flow cell, after which the in- and outlet of the flow cell were sealed with silicon grease mixed with silicon oil (2:1).

4.2.4 Optical tweezers experiment

While preparing the aaFtsH sample, the objective was preheated to 38 °C. After sample preparation, it was placed on the sample holder of the optical tweezers and, through a layer of (substitute) oil, brought in contact with the objective and condenser. The electrodes were connected to the power supply and the power supply was switched on to initiate heating of the flow cell to 53-60 °C.

The aaFtsH measurement was carried out similar to previous protease studies [1–5]. In the assay two beads of different sizes were used, the smallest beads ($d = 1.00 \mu\text{m}$) were incubated with aaFtsH and the larger beads ($d = 1.25 \mu\text{m}$) contained the substrate, with DNA-linker, Halo domain, and recognition *ssrA*-tag bound to it. The substrate-bound beads were immobilized on the glass surface of the flow cell and the aaFtsH-beads floated around freely.

The aaFtsH-beads were trapped by the weak AOD trap and brought in close proximity to the immobilized substrate-bound bead. To check if aaFtsH was linked to the substrate, the aaFtsH-bead was moved away from the substrate bound bead by moving the piezo stage, see fig. 4.3a. If a link was established, the bead was pulled out of the trap, see fig. 4.3b. The bead was then re-trapped and the second laser beam was unblocked to trap the substrate bound bead and detach from the surface, see fig. 4.3c. When both beads were trapped, fig. 4.3d, the beads were moved upwards to a few micrometer above the glass surface, fig. 4.3e, and then the detection beams were unblocked, fig. 4.3f. The bead position was acquired at 4 kHz

for 2 min.

After the recording, the calibration measurements were performed and recorded at 100 kHz. It was preferred to do the calibration with the same beads as the aaFtsH measurement. To check if the link was broken, the aaFtsH-bead was moved away from the substrate-bound bead by moving the AOD trap. In the case of a broken link, the aaFtsH-bead would show no signs of restrictions upon movement. The aaFtsH-bead was moved back to its original position and the beads were recorded for some time to determine the zero position of the beads. The zero position is the position of the bead within the detection laser when trapped. The presence of a second bead and, especially, its detection beam introduces an offset in bead position. For the AOD trap, the presence of a second bead and detection beam could be compensated for by having a second bead and detection beam during position calibration. But, this is not possible for the piezo trap as the position calibration (section 2.6.2) required the AOD trap and, thus, making it impossible to do the position calibration in the presence of the second bead.

To be able to convert voltage into nanometer and determine the stiffness of the trap, the position calibration, as described in section 2.4.2, and individual bead positions were recorded. The equipartition method was used to determine trap stiffness, as the viscosity of the experimental buffer is unknown. The presence of the substrate or aaFtsH on the bead should not significantly interact with the trapping light as they are too small [21].

4.2.5 **Data analysis**

All recorded bead positions, of linked and unlinked beads, were first converted from voltage to nanometer position. Then the data of linked beads was visualized by a scatter plot, showing the bead positions of the beads in both traps along the axis of the link. The center of the trap was determined by the mean position of the unlinked beads and used as zero position in the graphs. When a jump in bead position along the linking axis was present in the linked data, the direction (towards or away from the trap center) of the jump was determined. When the bead-to-trap distance decreased, an unfolding event was assumed and the data was further analyzed (as described below). If the bead-to-trap distance decreased, the data was further analyzed to determine if a refolding event could explain

4 Studying the mechanical properties of FtsH

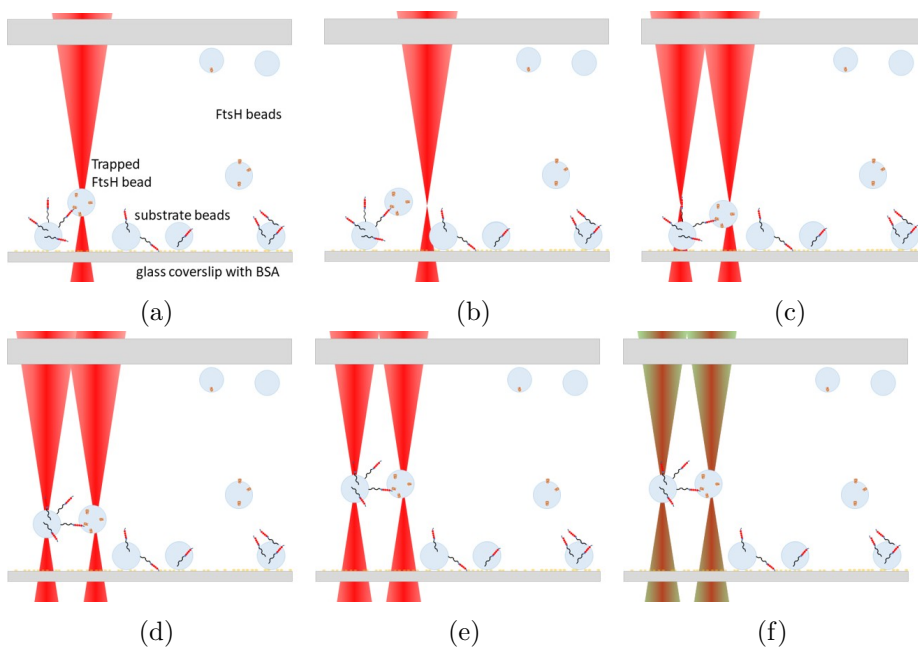


Figure 4.3: **Schematic representation of trapping procedure for an aaFtsH experiment** (not to scale). a) Bringing the aaFtsH-bead in close proximity of the substrate-bound bead and establishing a link. b) The trap was moved away to test if a link had formed. c) After re-trapping the aaFtsH-bead the second laser beam was unblocked. d) The substrate-bound bead was detached from the surface. e) The beads were moved upwards to a few micron above the glass surface. f) The detection beams were unblocked and data recording was started.

the jump. Degradation was considered when a gradual change of bead-to-trap distance was observed.

To ease visualization of the bead position and sudden changes in position, the recorded bead positions were grouped and averaged by a moving average. In the moving average, 100 points were grouped and averaged, and then plotted as a single data point after which the entire group moves to the next recorded bead positions. This reduces the bead fluctuations caused by Brownian motion by showing the mean position.

In an unfolding or refolding event, the displacement of the beads in both traps were analyzed. The displacement of both beads had to be considered, because the experiments were performed in the linear region of the trap, see section 1.3.1 for a description of the different regions of the trap, resulting in bead displacements of both beads. The displacements were determined by averaging the bead position over 250 ms before and after the jump. The bead movement of the bead in the weak trap should be larger than the bead movement of the bead in the strong trap with the ratio determined by the difference in trap stiffness between the traps. The displacements of an unfolding or refolding event were added up and compared to theory.

The theoretical change in bead-to-bead distance upon I27 or Halo unfolding or refolding was calculated by the WLC model (eq. (1.2)). The contour length has been previously experimentally determined to be 29 nm [10, 13] with persistence length 0.8 nm [11]; the temperature was measured; and the force was computed from the experimental results.

4.3 Results and discussion

4.3.1 Observed aggregation during the aaFtsH experiment

When the heated aaFtsH flow cell was visualized by the ccd camera, it could immediately be observed that the flow cell was 'dirty' with particles. These particles were first, mistakenly, denoted as bacteria. After observing these particles within each flow cell, in large quantities, and after extra cleaning steps, it was thought that perhaps some components of the experimental buffer aggregated at these high temperatures. This was not expected as activity of catalase (from bovine liver) [22], creatine

Table 4.1: **Observed aggregation for the components of the ATP-regeneration system and oxygen-scavenging system.** All components were dissolved in 20 mM Tris buffer, heated on a hot-plate of 52 °C flown into a flow cell and observed with a 60x microscope at room temperature.

Component	Concentration	Aggregation
ATP	10 mM	no
creatine kinase	0.06 mg/mL	yes
creatine phosphate	20 mM	no
glucose oxidase	0.25 mg/mL	no
dextrose	5 mg/mL	no
catalase	0.3 mg/mL	yes

kinase (of rat muscle) [23], and glucose oxidase [24] was confirmed up to 60 °C. Only for creatine kinase from human muscle it was reported that aggregation occurred after 20 min at 48 °C [23]. Nevertheless, aggregates need to be in the order of tens of nanometer to be visible with the ccd camera microscope, see section 4.5.1.

The components of the ATP-regeneration and oxygen-scavenging system, as used in previous protease optical tweezers studies [1–5], were individually dissolved in 20 mM Tris buffer and heated on a hot-plate to 52 °C for 10 mins. The solution was then studied with the ccd camera of the optical tweezers setup to scan for aggregation particles. It was observed that creatine kinase of the ATP-regeneration system and catalase of the oxygen-scavenging system had formed large aggregates, see table 4.1. Exclusion of these components was not trivial as the ATP-regeneration and oxygen-scavenging systems ensure protease activity [25] and viability of the organic compounds in the sample [26].

Reduction to a half or a third of the original catalase and creatine kinase concentration, still showed aggregation upon heating. These components were therefore excluded from the experimental buffer. The exclusion of creatine kinase made the ATP-regeneration system, which consists of ATP, creatine kinase and creatine phosphate, incomplete. Creatine kinase catalyzes the phosphorylation of ADP (adenosine diphosphate) to ATP by

dephosphorylating creatine phosphate. Excluding creatine kinase made creatine phosphate abundant, which was therefore also excluded from the experimental buffer. The ATP concentration in the experimental buffer was doubled to compensate for the absence of the regeneration system.

The exclusion of catalase made the oxygen-scavenging system, which consists of glucose oxidase, dextrose, and catalase, incomplete. Glucose oxidase catalyzes the oxidation of dextrose to hydrogen peroxide and gluconolactone. Catalase then catalyzes hydrogen peroxide to water and oxygen, preventing oxygen radicals to damage the organic compounds [26]. By mistake, dextrose was excluded from the experimental buffer as well. When later dextrose was re-introduced, it caused the substrate-bound beads to bind more tightly to the glass surface and also to the aaFtsH-bead when brought (too) closely together. This made the experimental procedure nonfunctional. To increase the chances of successfully establishing a link and detaching the substrate-bound bead, dextrose was excluded again and only glucose oxidase was present of the oxygen-scavenging system. Without dextrose, glucose oxidase cannot work. Nonetheless, it was included as the experiment was optimized for the experimental buffer containing glucose oxidase and due to limited time the optimized buffer was used. Although, it is unknown how (severely) the absence of the oxygen-scavenging system effects the organic compounds and the effect on the measurement.

The aaFtsH experiments were carried out in the reduced experimental buffer. However, aggregation was still observed. The remaining components of the ATP-regeneration system and oxygen-scavenging systems were mixed, heated and observed, but did not show aggregation. Eventually, it was found that DTT (dithiothreitol) aggregated with the zinc-magnesium (ZnMg) mixture. Indeed, DTT and Zn^{2+} have been reported to form a zinc-dithiothreitol complex [27]. DTT is required in the experimental buffer as it prevents the formation of disulfide bonds in DNA. It was therefore replaced, rather than excluded, by TCEP which has the same function as DTT, but does not form a complex with zinc. After replacement of DTT by TCEP, aggregation was no longer observed during the aaFtsH experiment.

4.3.2 Optimizing the aaFtsH experiment

The optical tweezers experiment requires the success of many individual steps. These steps include the linkage of DNA-HaloTag to HaloEnzyme-I27^{V13P} or HaloEnzyme-I27^{V15P}, the presence of the ssrA-tag on I27^{V13P} and I27^{V15P}, the linkage of DNA-HaloEnzyme-[I27^{V13P}]_{x4}-ssrA or -[I27^{V15P}]_{x4}-ssrA to the streptavidin bead, aaFtsH activity, the linkage of aaFtsH to the streptavidin bead, the immobilization of the substrate bound bead to the glass surface of the flow cell, the temperature, placement of the sample in the optical tweezers, and the execution of the experiment. As the aaFtsH experiment remained unsuccessful without apparent reason many of these steps have been checked individually.

A bulk assay of aaFtsH degradation at different temperatures proved the success of many different steps. In the bulk assay aaFtsH and ssrA-tagged [I27^{V13P}]_{x4} were kept for one hour and a half at experimental temperatures and then loaded on an SDS-PAGE (sodium dodecyl sulfate polyacrylamide gel electrophoresis) gel and imaged. The degradation was determined by the intensity of the I27^{V13P} band present on the gel, with the intensity at 45 °C taken as 100 % (no degradation) in fig. 4.4 for three different batches of aaFtsH. These results show that aaFtsH did not degrade [I27^{V13P}]_{x4}-ssrA at temperatures of 49 °C and below, and reached maximal degradation of [I27^{V13P}]_{x4}-ssrA at 57 °C. It can also be observed that ~58 % of [I27^{V13P}]_{x4}-ssrA was not degraded. This could indicate that not all of the I27^{V13P} constructs have an ssrA-tag or this could be due to inactivation of aaFtsH after prolonged degradation [28]. A western blot analysis, using custom anti-ssrA primary antibodies, of bulk degradation indicated that the ssrA-tag for non-degraded I27^{V13P} was present, see fig. 4.9 in section 4.5.2. Therefore it is believed that aaFtsH becomes inactive after prolonged degradation. A bulk degradation time series to study this inactivation has not been performed.

Another concern was the presence of aaFtsH and DNA-HaloEnzyme-[I27^{V13P}]_{x4}-ssrA on the beads. The biotinylation of aaFtsH has been confirmed by western blot analysis. If the biotin is accessible, it will bind to the streptavidin beads. To test if aaFtsH and the DNA-HaloEnzyme-[I27^{V13P}]_{x4}-ssrA were indeed present on the beads, a fluorescence assay was employed for each. In the assay, aaFtsH or DNA-HaloEnzyme-[I27^{V13P}]_{x4}-ssrA was incubated with the streptavidin beads. The bead

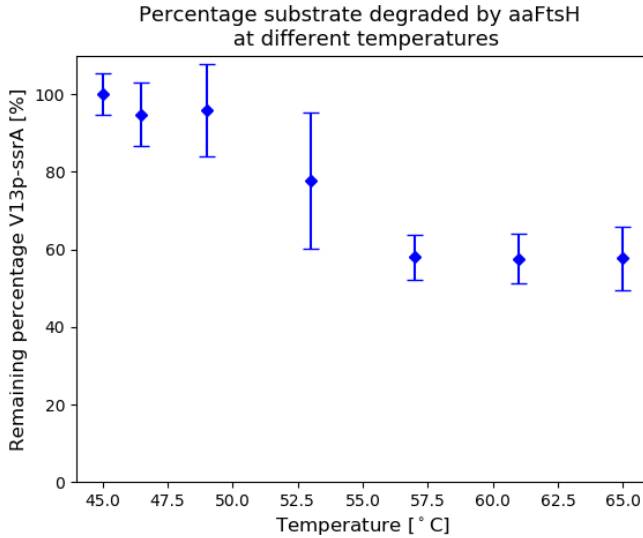


Figure 4.4: Degradation of $V^{13P}I27$ -ssrA substrate by aaFtsH at varying experimental temperatures.

solution was washed by centrifugation and resuspension in experimental buffer. This was repeated three times, to remove any unbound aaFtsH. The washed bead solution was incubated with an anti-his antibody or a custom anti-ssrA antibody and further amplified by a secondary antibody coupled to HRP (**h**orse-**r**adish-**p**eroxidase). This was then quantified through luminescence measurements based on HRP activity with luminol and stable isotopes of hydrogen peroxide. The luminescence results confirmed the presence of bound aaFtsH and the presence of bound DNA-HaloEnzyme- $[I27^{V13P}]_x4$ -ssrA, see table 4.5 and table 4.6 in section 4.5.3. The luminescence results of DNA-HaloEnzyme- $[I27^{V13P}]_x4$ -ssrA also demonstrated that the amount of DNA-HaloTag limited the fluorescence intensity. The amount of DNA-HaloTag that was incubated with HaloEnzyme- $[I27^{V13P}]_x4$ -ssrA was therefore increased.

A bulk activity assay with aaFtsH, that was about four weeks old, still showed activity. However, during optical tweezers experiments it was observed that after 4 or 5 days it became rare to establish a link between the aaFtsH-bead and a substrate-bound bead. Since aaFtsH was filtered be-

4 *Studying the mechanical properties of FtsH*

fore the optical tweezers experiment, but not before the bulk assay it was thought that aaFtsH might aggregate while remaining active and therefore lowering the number of aaFtsH hexamers present in the optical tweezers experiment, yet showing activity in the bulk assay. However, formation of (many) large aggregates were ruled out by the unchanging concentration of aaFtsH after filtration for a week, see section 4.5.4. The reason for the observed difference in activity is still obscure.

The challenges experienced during the optical tweezers experiment included air bubble formation in the oil substitute by the contact between the sample and objective, difficulty in trapping the immobilized bead after link formation, and the precision with which the sample had to be moved. To reduce the chance of air bubble formation in the substitute oil, a droplet of oil was placed both on the sample and on the objective. This significantly reduced the probability of having an air bubble, but it occasionally still occurred. Upon bubble formation, the experiment had to be terminated as it affects the trap.

The immobilized substrate-bound bead had to be detached from the glass surface after link formation by the 'strong' piezo trap. However, this was far from convenient. The temperature and casein concentration in the experimental buffer affected the binding of the substrate-bound bead to the glass surface. The casein concentration was therefore checked by UV-vis absorption and compensated by the volume added to the experimental buffer. The temperature affects the binding of the substrate bound bead, the activity of aaFtsH, and the (unfolding) stability of I27^{V13P}, I27^{V15P}, and the dsDNA. To have a finer control over the temperature, a thermocouple was added to the flow cell. Nonetheless, within a single flow cell some of these substrate bound beads would already detach when the 'weak' AOD trap was in close proximity, while others would not detach at all.

The remaining experimental challenge was the care and precision required. Manual movement of the piezo stage was done by two rotating knobs, one for the x-axis and one for the y-axis. However, upon movement in the y-axis, the trapping height was affected sometimes causing the bead to be stuck to the surface (after link formation). Besides that, the flow cell could be moved $\sim 1 \mu\text{m}$ without actually rotating the knob. Upon release of the knob, the flow cell would move back to its initial position. To have

the knob rotate, the flow cell had to be moved further, however, this could mean either losing the aaFtsH-bead (after link formation) or having the aaFtsH-bead and substrate-bound bead in contact.

Nonetheless, successful links have been obtained and a few of them could be recorded after successful bead detachment. However, after the optimization, the success rate was about one recording per experimental week.

4.3.3 Bead recordings of aaFtsH linked to I27^{V13P}

Surprisingly, it was found that links could be established at temperatures lower than the minimum temperature required for proteolytic activity. Forming links at such lower temperature allows for successful link formation and trapping of the beads without degradation activity. One successful link and trapping of the beads was established for the I27^{V13P} at 45 °C. The beads were recorded at 45 °C for 120 s before increasing the temperature to study the activity. However, analysis of the bead positions at 45 °C showed that the link broke at the end of the recording, see fig. 4.5.

It can be seen in the figure that after ~ 37 s a jump occurred and another, much larger, jump occurred at the end of the recording. Upon analysis, the first jump is expected to be an unfolding event and at the second jump breaking of the link. The total increase in distance during the unfolding event is 14.1 nm at approximately 2 pN. At this force the predicted extension of I27^{V13P} by the WLC model is approximately 6 nm, which is much smaller than the observed 14.1 nm. Therefore, the predicted extension of the Halo domain by the WLC model was determined. This gave an expected extension of approximately 11 nm. It is therefore likely that the observed unfolding event is from the Halo domain rather than an I27^{V13P} module. It is likely that the unfolding event occurred upon spontaneous unfolding, triggered by the high temperature and small stretching force, rather than active unfolding by aaFtsH as the protease is not active at 45 °C. The unfolding results are summarized in table 4.2.

Besides the unfolding event and breaking of the link, a change in bead fluctuations in the weak trap was observed, grey dots in fig. 4.5. This change in fluctuations is not apparent in the strong trap. It is possible that the larger bead fluctuations represent (unsuccessful) refolding or degradation attempts. The increase in fluctuations appears to be towards

4 Studying the mechanical properties of FtsH

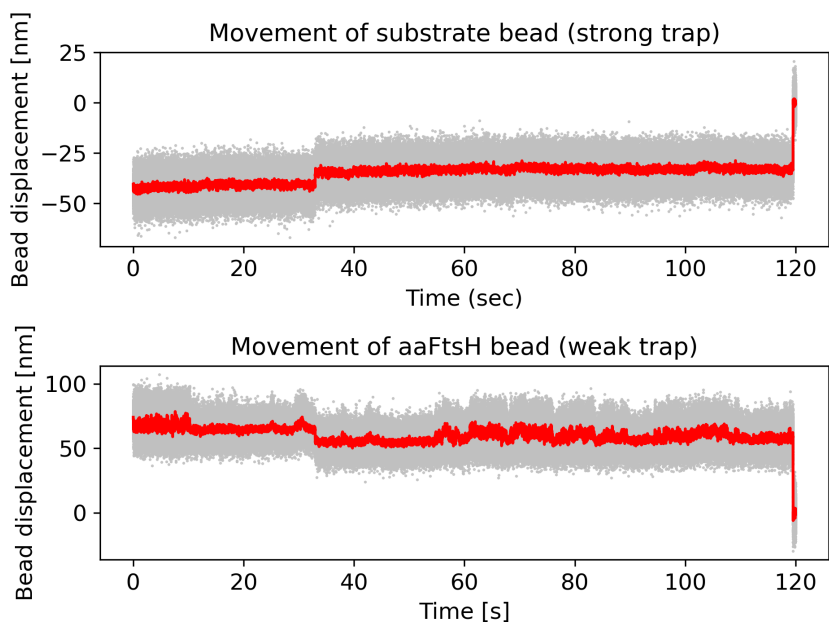


Figure 4.5: **Bead position recording of two linked and trapped beads at 45 °C.** The top figure shows the bead position with respect to time of the larger substrate-bound bead in the strong trap and the bottom figure the bead positions of the smaller aaFtsH-bound bead in the weak trap. The bead positions are shown in light grey and the moving average is shown in red. After ~ 37 s an unfolding event occurred, which can be seen by the bead positions moving closer to the trap center. At the end of the recording the link between the beads broke and the beads moved to the center of the trap.

Table 4.2: **Results of the unfolding event observed when aaFtsH was linked to the I27^{V13P} substrate at 45 °C.**

	Trap stiffness	Extension	Force pre-unfolding	Force post-unfolding
	[pN/nm]	[nm]	[pN]	[pN]
Weak trap	0.023	8.7	1.5	1.3
Strong trap	0.061	5.4	2.4	2.1
Total		14.1		

the other bead (away from the trap center) and is therefore presumed to be refolding or degradation attempts rather than unfolding attempts. Measuring the change in (moving) average bead position indicates a displacement of about 5 to 10 nm, this makes degradation attempts unlikely as a single step is expected to be smaller and, besides that, degradation is not expected to occur at 45 °C. These fluctuations are thus presumed to be spontaneous unfolding attempts.

The second recording, when the temperature was increased, was also analyzed. An apparent bead displacement was visible, especially at the beginning of the recording. This can be explained by the observed focal drift in the z-axis. This drift occurred after increasing the temperature [29, 30] and affected the apparent bead position. The change in temperature at the beginning of the recording is largest, due to the larger difference in temperature of the solvent and newly set temperature, which explains the apparent bead displacement that was mainly seen at the beginning of the recording (data not shown). This focal drift interferes with possible degradation and unfolding events and was therefore no longer carried out.

Establishing and maintaining a link after heating was rare. When a link was established, the substrate-bound bead had to be detached from the glass surface before bead recording was initiated. Detaching the bead proved to be challenging. Casein was added to the experimental buffer as this affects the binding of the bead to the glass surface. However, this is not exclusively affecting the binding, so does the temperature. The casein concentration in the experimental buffer was optimized, such that detachability of substrate-bound beads was feasible. Nonetheless, it still

4 Studying the mechanical properties of FtsH

Table 4.3: **Results of jumps and gradual bead displacements when aaFtsH was linked to the I27^{V13P} substrate at $\sim 55^\circ\text{C}$.**

	Trap stiff- ness	Jump 1	Jump 2	Gradual displace- ment 1	Gradual displace- ment 2
	pN/nm	nm	nm	nm	nm
Weak trap	0.023	4.4	1.6	6.9	5.0
Strong trap	0.149	6.1	10.5	12.4	18.8
Total		10.5	12.1	19.3	23.8

gave variability: within a single flow cell, there were beads that detached by the presence of the weak trap and at the same time beads that could not be detached by the strong trap.

A recording where the beads successfully linked and detached from the glass surface is shown in fig. 4.6. The bead recording, unexpectedly, showed large movements for the bead in the strong trap ($\kappa = 0.14$ pN/nm) and almost no movement of the bead in the weak trap ($\kappa = 0.02$ pN/nm). Analyzing the jumps and the bead displacements between the jumps resulted in jump sizes of 10.5 and 12.1 nm and gradual displacements of 19.3 and 23.8 nm, as shown in table 4.3. The pulling forces computed from the bead displacements in the strong trap range from 6.4 pN/nm pre-unfolding to 4.8 pN/nm post-unfolding. The WLC model predicted an increase in distance of approximately 12 nm upon I27^{V13P} and of approximately 23 nm upon Halo domain unfolding at 5 pN. The measured displacements correspond to the predicted I27^{V13P} unfolding. However, due to the discrepancy between expected and observed bead displacements in the weak and strong trap, no conclusions can be drawn.

The unfolding events in our study did not show an intermediate state. This could be due to the limited number of unfolding events or the increased temperature.

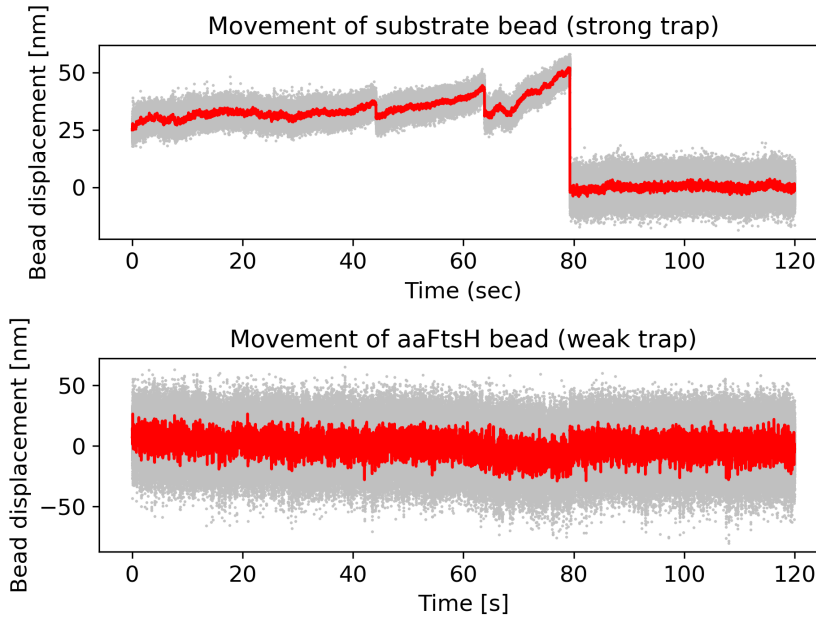


Figure 4.6: **Bead position recording of two linked and trapped beads at $\sim 55^\circ\text{C}$.** The top figure shows the bead position with respect to time of the larger substrate-bound bead in the strong trap. The bottom figure shows the bead positions of the smaller aaFtsH-bound bead in the weak trap. The bead positions are shown in light grey and the moving average is shown in red. Unexpectedly, bead movement is mainly observed in the strong trap, which was approximately 7 times stronger than the weak trap. It is therefore not clear what has been measured. Nonetheless, it seems as if unfolding events occurred at ~ 43 and ~ 62 s, as the bead is moving closer to the trap center. The gradual slope of the bead moving away would then be caused by degradation. At the end of the recording the link between the beads broke and the beads moved to the center of the trap.

4.3.4 Bead recordings of aaFtsH linked to I27^{V15P}

One bead recording for linked aaFtsH and I27^{V15P} was obtained. Before the recording was initiated, it was noted that the link appeared to be shorter than expected. Nonetheless, the big bead was trapped and bead recording initiated. The results of this recording are shown in fig. 4.7. The displacement of the bead from the trap center of the weak trap is indeed much larger than during I27^{V13P} recordings. This can partially be explained by the distance between the two traps, which was 2.20 μm for both recordings of I27^{V13P} and changed to 2.35 μm before this measurement. However, the expected displacement from the trap center should be close to 225 nm rather than the recorded 450 nm.

In the recording, a jump away from the trap center (after 5 s) was observed, before the link broke (at 40 s), see fig. 4.7. Analyzing this jump gave a total displacement of 204.5 nm. This is much larger than what can be expected for a refolding event of an I27^{V15P} module or the Halo domain and is therefore not considered to be a refolding event. The cause of the shortened link and sudden jump away from the trap center remains ambiguous. It should be noted that, due to the large displacement from the center of the trap in the weak trap, the bead might be located in or already past the passive force region and the detection beam could possibly no longer accurately measure the position of the bead. Even if the bead positions are no longer correct for the weak trap, the jump still appears to be much larger than a possible refolding event as the bead position within the strong trap should be accurate and already is larger than the expected refolding length. The results are summarized in table 4.4.

4.3.5 Double tethered beads

Occasionally, the substrate-bound bead would not completely detach from the glass surface, but remain tethered. It is expected that either a single or multiple DNA-Halo-I27^{V13P} or -I27^{V15P} complexes linked to the glass surface, causing the bead to be only partially detached from the surface. These beads have been recorded and visualized (data not shown), but were not analyzed due to its complexity.

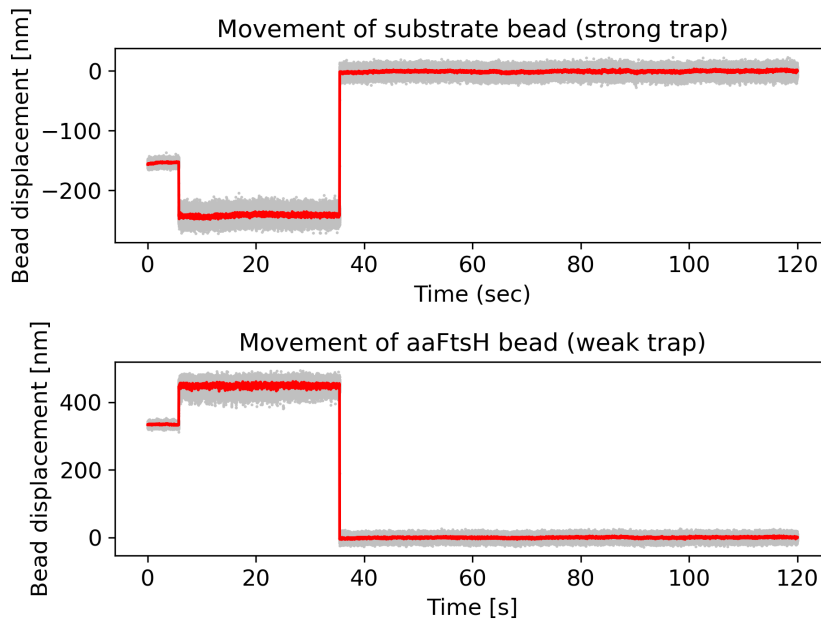


Figure 4.7: **Bead position recording of two linked and trapped beads at 45 °C.** The top figure shows the bead position with respect to time of the larger substrate-bound bead in the strong trap and the bottom figure the bead positions of the smaller aaFtsH-bound bead in the weak trap. The bead positions are shown in light grey and the moving average is shown in red. After ~ 5 s a jump occurred away from the center of the trap. After ~ 40 s link between the beads broke and the beads moved to the center of the trap.

4 Studying the mechanical properties of FtsH

Table 4.4: **Results of the unfolding event observed when aaFtsH was linked to the I27^{V15P} substrate at 54 °C.**

	Trap stiffness [pN/nm]	Extension [nm]	Force pre-unfolding [pN]	Force post-unfolding [pN]
Weak trap	0.045	115.1		
Strong trap	0.086	89.4	13.2	20.9
Total		204.5		

4.4 Conclusion

Studying the mechanical properties of aaFtsH by optical tweezers turned out to be very challenging. The high temperature required for aaFtsH activity caused the exclusion of the oxygen-scavenging and ATP regeneration system in the experimental buffer. The ATP regeneration system was compensated by doubling the ATP concentration. However, the oxygen-scavenging system could not be compensated and was thus absent. It is unknown how (severely) this affects the organic compounds during the optical tweezers measurement. Nonetheless, aaFtsH-substrate links were established and occasionally recorded. Unfortunately, these recordings could not be used to determine the step size, translocation rate, or pulling power of aaFtsH, because the data was faulty or no degradation occurred.

4.5 Supplementary information

4.5.1 Aggregation observed during optical tweezers aaFtsH experiments

Aggregation observed with ccd camera during optical tweezers aaFtsH experiments. At 44 °C no aggregation was observed, as shown in fig. 4.8a where the beads with a diameter of 1.25 μm are encircled in red, camera artifacts in black, and two clustered beads of diameter 1.25 μm .

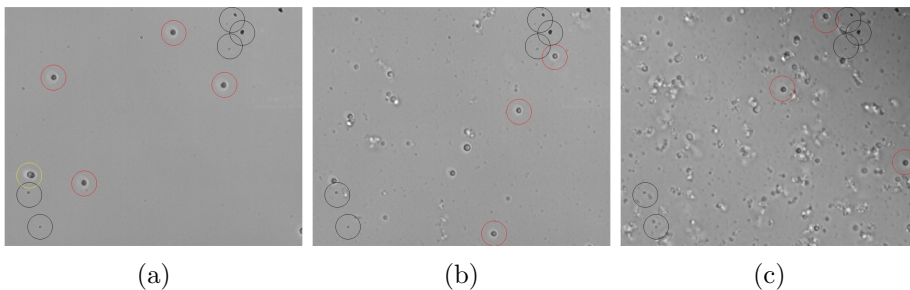


Figure 4.8: **Images of beads (and aggregates) as observed during aaFtsH experiment when temperature was increased from 44 °C to 72 °C.** The beads with a diameter of 1.25 μm are encircled in red, camera artifacts encircled in black, and two clustered beads of diameter 1.25 μm encircled in yellow. a) No aggregation was observed at 44 °C. b) Small and large aggregates are present at 55-60 °C. c) Many small and large aggregates have formed at 72 °C.

4.5.2 Bulk degradation of I27^{V13P} by aaFtsH

The SDS-PAGE gels and western blot were done by Dr. Ramon van der Valk. In the SDS-PAGE gel, top figure in fig. 4.9, an example of a degradation bulk assay for I27^{V13P} and aaFtsH at varying experimental temperatures is shown. They were kept for one hour and a half at the experimental temperature before loading on gel.

The SDS-PAGE gel was used to do a western blot with an anti-ssrA antibody. The result is shown in bottom figure in fig. 4.9. The top bands show the non-degraded [I27^{V13P}]₄-ssrA. It can be seen that even at 60 °C,

4 Studying the mechanical properties of *FtsH*

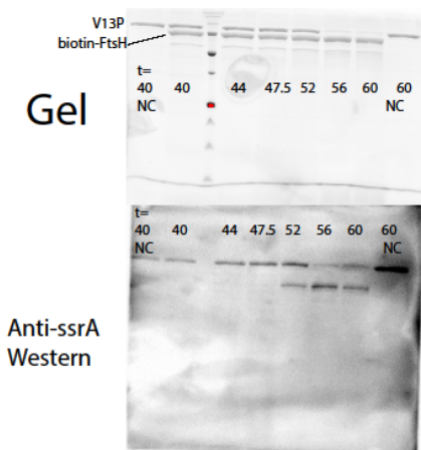


Figure 4.9: **Bulk degradation of [I27^{V13p}]x4-ssrA by aaFtsH at varying experimental temperatures.** The top figure shows the SDS-PAGE gel of [I27^{V13p}]x4-ssrA degradation by biotin-aaFtsH. The negative control (NC), on the left side (at 40 °C) and right side (at 60 °C) of the gel, only contains [I27^{V13p}]x4-ssrA and no biotin-aaFtsH. The bottom figure shows the anti-ssrA western blot. The top bands show the non-degraded [I27^{V13p}]x4-ssrA and the lower band at 52, 56, and 60 °C is thought to be the ssrA-tag covalently bound to biotin-aaFtsH.

where maximal degradation was reached, the ssrA-tag is still present. This supports the argument of Yang et al. [28] that aaFtsH is inactivated after prolonged degradation. Another interesting finding is that (some of) the ssrA-tag seem to covalently bind to biotin-aaFtsH after degradation.

4.5.3 Luminescence results

Binding of aaFtsH and DNA-HaloEnzyme-[I27^{V13p}]x4-ssrA to the streptavidin beads was confirmed through luminescence. Table 4.5 shows the luminescence results of aaFtsH-beads used during the optical tweezers experiment on different days. These beads were compared to the luminescence of beads without aaFtsH. It should be noted that the concentration of beads in absence of aaFtsH was much higher than for the beads in presence of aaFtsH. The concentration of aaFtsH-beads on different

Table 4.5: **Luminescence results confirm the binding of aaFtsH to streptavidin beads.** The luminescence values between different days varies significantly, this is caused by the variation in the number of beads present in the measurement. The standard deviation was obtained from measuring each sample thrice. The bead concentration for beads **without** aaFtsH is much larger than the bead concentration for beads **with** aaFtsH. The equal luminescence of beads without and beads with on day 2 and 3, confirm that aaFtsH is present.

Sample	Luminescence [a.u.]	Stdev of luminescence
Beads	12331	235
No beads	4799	516
aaFtsH-beads day 1	9012	400
aaFtsH-beads day 2	17695	575
aaFtsH-beads day 3	64526	3980
aaFtsH-beads day 4	4283	82

days also varied greatly and caused the large differences in luminescence. Nonetheless, the luminescence results show that aaFtsH is bound to the beads. Table 4.6 shows the luminescence results of DNA-HaloEnzyme-[I27^{V13P}]_{x4}-ssrA-beads. The results indicate that the amount of DNA limits the luminescence and thereby the number of DNA-HaloEnzyme-[I27^{V13P}]_{x4}-ssrA bound to the streptavidin beads.

4.5.4 AaFtsH aggregation

The aaFtsH concentration after filtration was determined by nanodrop on the experimental day before aaFtsH with bead incubation. Two 0.1 μm centrifugal filter units (Merck Millipore Ltd.) were first saturated by centrifuging 100 μL aaFtsH buffer (5.000 rpm for 3 mins). Then 160 μL aaFtsH was loaded on the filter unit and centrifuged at 5.000 rpm for 3 mins. The concentration of the filtrate aaFtsH was determined by nanodrop before the experiment.

4 Studying the mechanical properties of *FtsH*

Table 4.6: **Luminescence results confirm the binding of DNA-HaloEnzyme-[I27^{V13P}]x4-ssrA to streptavidin beads.** The luminescence results show that the substrate is bound to the beads and that the amount of DNA-HaloTag limits the luminescence.

Sample	Luminescence [a.u.]
20 μ L of HRP + Luminol	228844
Luminol	27
800 ng DNA + 25 μ L I27 ^{V13P}	7695
240 ng DNA-HaloTag + 25 μ L I27 ^{V13P}	6586
600 ng DNA-HaloTag + 25 μ L I27 ^{V13P}	20999

Table 4.7: **Measured aaFtsH (buffer) concentrations after 0.1 μ m filtration, before aaFtsH bead incubation.** The concentration of the filtrate of the 100 μ L saturation aaFtsH buffer was also determined as a control. The nanodrop blank was determined by unfiltered aaFtsH buffer. After which the aaFtsH concentration of sample 1 was taken, then the aaFtsH buffer concentration of sample 1, followed by the aaFtsH concentration of sample 2, and the aaFtsH buffer concentration of sample 2.

		aaFtsH concentration	Buffer concentration
Day 0	sample 1	0.35 mg/mL	-0.01 mg/mL
	sample 2	0.31 mg/mL	0.00 mg/mL
Day 1	sample 1	0.39 mg/mL	0.00 mg/mL
	sample 2	0.38 mg/mL	0.00 mg/mL
Day 2	sample 1	0.32 mg/mL	-0.02 mg/mL
	sample 2	0.36 mg/mL	-0.02 mg/mL
Day 3	sample 1	0.34 mg/mL	0.01 mg/mL
	sample 2	0.32 mg/mL	-0.02 mg/mL
Day 6	sample 1	0.36 mg/mL	-0.02 mg/mL
	sample 2	0.34 mg/mL	-0.01 mg/mL

References

- (1) Aubin-Tam, M.-E.; Olivares, A. O.; Sauer, R. T.; Baker, T. A.; Lang, M. J. Single-Molecule Protein Unfolding and Translocation by an ATP-Fueled Proteolytic Machine. *Cell* **2011**, *145*, 257–267.
- (2) Cordova, J. C.; Olivares, A. O.; Shin, Y.; Stinson, B. M.; Calmat, S.; Schmitz, K. R.; Aubin-Tam, M.-E.; Baker, T. A.; Lang, M. J.; Sauer, R. T. Stochastic but Highly Coordinated Protein Unfolding and Translocation by the ClpXP Proteolytic Machine. *Cell* **2014**, *158*, 647–658.
- (3) Olivares, A. O.; Nager, A. R.; Iosefson, O.; Sauer, R. T.; Baker, T. A. Mechanochemical basis of protein degradation by a double-ring AAA+ machine. *Nature Structural; Molecular Biology* **2014**, *21*, 871–875.
- (4) Iosefson, O.; Olivares, A. O.; Baker, T. A.; Sauer, R. T. Dissection of Axial-Pore Loop Function during Unfolding and Translocation by a AAA+ Proteolytic Machine. *Cell Reports* **2015**, *12*, 1032–1041.
- (5) Olivares, A. O.; Kotamarthi, H. C.; Stein, B. J.; Sauer, R. T.; Baker, T. A. Effect of directional pulling on mechanical protein degradation by ATP-dependent proteolytic machines. *Proceedings of the National Academy of Sciences* **2017**, *114*, DOI: 10.1073/pnas.1707794114.
- (6) Olivares, A. O.; Baker, T. A.; Sauer, R. T. Mechanistic insights into bacterial AAA+ proteases and protein-remodelling machines. *Nature Reviews Microbiology* **2015**, *14*, 33–44.
- (7) Olivares, A. O.; Baker, T. A.; Sauer, R. T. Mechanical Protein Unfolding and Degradation. *Annual Review of Physiology* **2018**, *80*, 413–429.
- (8) Greenleaf, W. J.; Woodside, M. T.; Abbondanzieri, E. A.; Block, S. M. Passive All-Optical Force Clamp for High-Resolution Laser Trapping. *Physical Review Letters* **2005**, *95*, 208102.
- (9) Yu, M.; Lu, J.-H.; Le, S.; Yan, J. Unexpected Low Mechanical Stability of Titin I27 Domain at Physiologically Relevant Temperature. *The Journal of Physical Chemistry Letters* **2021**, *12*, 7914–7920.

4 Studying the mechanical properties of FtsH

- (10) Kotamarthi, H. C.; Sauer, R. T.; Baker, T. A. The Non-dominant AAA Ring in the ClpAP Protease Functions as an Anti-stalling Motor to Accelerate Protein Unfolding and Translocation. *Cell Reports* **2020**, *30*, 2644–2654.e3.
- (11) Carrion-Vazquez, M.; Oberhauser, A. F.; Fowler, S. B.; Marszalek, P. E.; Broedel, S. E.; Clarke, J.; Fernandez, J. M. Mechanical and chemical unfolding of a single protein: A comparison. *Proceedings of the National Academy of Sciences* **1999**, *96*, 3694–3699.
- (12) Li, H.; Carrion-Vazquez, M.; Oberhauser, A. F.; Marszalek, P. E.; Fernandez, J. M. Point mutations alter the mechanical stability of immunoglobulin modules. *Nature Structural Biology* **2000**, *7*, 1117–1120.
- (13) Taniguchi, Y.; Brockwell, D. J.; Kawakami, M. The Effect of Temperature on Mechanical Resistance of the Native and Intermediate States of I27. *Biophysical Journal* **2008**, *95*, 5296–5305.
- (14) Somkuti, J.; Mártonfalvi, Z.; Kellermayer, M. S.; Smeller, L. Different pressure-temperature behavior of the structured and unstructured regions of titin. *Biochimica et Biophysica Acta (BBA) - Proteins and Proteomics* **2012**, *1834*, 112–118.
- (15) Yuan, G.; Le, S.; Yao, M.; Qian, H.; Zhou, X.; Yan, J.; Chen, H. Elasticity of the Transition State Leading to an Unexpected Mechanical Stabilization of Titin Immunoglobulin Domains. *Angewandte Chemie International Edition* **2017**, *56*, 5490–5493.
- (16) Taniguchi, Y.; Kawakami, M. Application of HaloTag Protein to Covalent Immobilization of Recombinant Proteins for Single Molecule Force Spectroscopy. *Langmuir* **2010**, *26*, 10433–10436.
- (17) Chen, H.; Yuan, G.; Winardhi, R. S.; Yao, M.; Popa, I.; Fernandez, J. M.; Yan, J. Dynamics of Equilibrium Folding and Unfolding Transitions of Titin Immunoglobulin Domain under Constant Forces. *Journal of the American Chemical Society* **2015**, *137*, 3540–3546.
- (18) Wang, M.; Yin, H.; Landick, R.; Gelles, J.; Block, S. Stretching DNA with optical tweezers. *Biophysical Journal* **1997**, *72*, 1335–1346.

- (19) Rico-Pasto, M.; Ritort, F. Temperature-dependent elastic properties of DNA. *Biophysical Reports* **2022**, *2*, 100067.
- (20) Carvalho, V.; Prabudiansyah, I.; Kovacik, L.; Chami, M.; Kieffer, R.; van der Valk, R.; de Lange, N.; Engel, A.; Aubin-Tam, M.-E. The cytoplasmic domain of the AAA+ protease FtsH is tilted with respect to the membrane to facilitate substrate entry. *Journal of Biological Chemistry* **2021**, *296*, 100029.
- (21) Bustamante, C. J.; Chemla, Y. R.; Liu, S.; Wang, M. D. Optical tweezers in single-molecule biophysics. *Nature Reviews Methods Primers* **2021**, *1*, DOI: <https://doi.org/10.1038/s43586-021-00021-6>.
- (22) Yumoto, I.; Ichihashi, D.; Iwata, H.; Istokovics, A.; Ichise, N.; Matsuyama, H.; Okuyama, H.; Kawasaki, K. Purification and Characterization of a Catalase from the Facultatively Psychrophilic Bacterium *Vibrio rumoiensis* S-1 (T) Exhibiting High Catalase Activity. *Journal of Bacteriology* **2000**, *182*, 1903–1909.
- (23) Wu, Q.-Y.; Wei, F.; Zhu, Y.-Y.; Tong, Y.-X.; Cao, J.; Zhou, P.; Li, Z.-Y.; Zeng, L.-Y.; Li, F.; Wang, X.-Y.; Xu, K.-L. Roles of amino acid residues H66 and D326 in the creatine kinase activity and structural stability. *International Journal of Biological Macromolecules* **2018**, *107*, 512–520.
- (24) O'malley, J. J.; Ulmer, R. W. Thermal stability of glucose oxidase and its admixtures with synthetic polymers. *Biotechnology and Bioengineering* **1973**, *15*, 917–925.
- (25) Shi, X.; Wu, T.; Cole, C. M.; Devaraj, N. K.; Joseph, S. Optimization of ClpXP activity and protein synthesis in an *E. coli* extract-based cell-free expression system. *Scientific Reports* **2018**, *8*, DOI: [10.1038/s41598-018-21739-6](https://doi.org/10.1038/s41598-018-21739-6).
- (26) Fridovich, I. The Biology of Oxygen Radicals. *Science* **1978**, *201*, 875–880.
- (27) Cornell, N. W.; Crivaro, K. E. Stability constant for the zinc-dithiothreitol complex. *Analytical Biochemistry* **1972**, *47*, 203–208.

4 Studying the mechanical properties of FtsH

- (28) Yang, Y.; Gunasekara, M.; Muhammednazaar, S.; Li, Z.; Hong, H. Proteolysis mediated by the membrane-integrated ATP-dependent protease FtsH has a unique nonlinear dependence on ATP hydrolysis rates. *Protein Science* **2019**, DOI: 10.1002/pro.3629.
- (29) Mao, H.; Arias-Gonzalez, J. R.; Smith, S. B.; Tinoco Jr., I.; Bustamante, C. Temperature Control Methods in a Laser Tweezers System. *Biophysical Journal* **2005**, *89*, 1308–1316.
- (30) Mahamdeh, M.; Schäffer, E. Optical tweezers with millikelvin precision of temperature-controlled objectives and base-pair resolution. *Optics Express* **2009**, *17*, 17190.

Chapter 5

Conclusion and outlook

In attempt to study the thermophilic aaFtsH, a novel heating system was designed and tested. AaFtsH showed to be active at temperatures above 53 °C and our novel heating system demonstrated the capability to achieve a temperature of up to 70 °C. However, this high temperature caused aggregation of biomolecules and complicated the optical tweezers study. Bead recordings have been obtained, but were not yet suitable to determine the mechanical activity of aaFtsH. Future studies could improve the success rate of the aaFtsH optical tweezers experiments and discover if and why the ssrA-tag binds to aaFtsH after degradation.

5.1 Conclusion

Throughout this thesis, I described my path towards the optical tweezers [1, 2] study of the protease FtsH [3]. The first step, described in chapter 2, was to build [4] and program a dual beam optical tweezers. The new setup can move a trapped bead (at least) $10\ \mu\text{m}$ in all directions and the code written to control the optical tweezers setup has been made available on the open-core company GitLab Inc. While building, the passive force clamp region on the existing setup was determined. This trap has a linear force-displacement over $\sim 100\ \text{nm}$ and a passive force region of $\sim 50\ \text{nm}$. The new setup has the same objective and is expected to have a similar force-displacement curve as the existing setup.

The objective heating system, as described in chapter 3, was mounted on the newly built setup. A heating system is required to study the purified full-length FtsH found in the thermophilic bacterium *Aquifex aeolicus* (aaFtsH) [5]. This bacterium is related to the filamentous bacteria which was found in the outflow of hot springs in Yellowstone National Park and grows best at temperatures between 85 and $95\ ^\circ\text{C}$ [6]. After an activity assay at varying experimental temperatures, the lower limit of aaFtsH activity for titin I27^{V13P} was found to be $\sim 53\ ^\circ\text{C}$ (chapter 4).

The heating system had to be complemented to reach such a high temperature and prevent for temperature gradients. A flow cell with a conductive microscope glass slide was constructed, which radiates heat by the Joule effect [7]. The conductive microscope glass slide was purchased, but our self-made copper circuit glued onto a microscope slide also proved to be usable. The commercial conductive microscope slide contained an indium tin oxide (ITO) conductive layer. To measure the temperature, a thin thermocouple was fixated in the flow cell and our novel method, that locally computes the temperature from bead recordings, was tested. Our novel method was tested by obtaining the laser-induced heating of our trap in a bare glass flow cell and was compared to theory. The laser caused a $2.8\ ^\circ\text{C}/100\ \text{mW}$ temperature increase for a $r = 0.92\ \text{nm}$ polystyrene bead in water. This was comparable to theory [8] and similar experimentally obtained results [9, 10]. The ITO flow cell demonstrated a much larger laser-induced effect, which can be attributed to laser absorption by the ITO layer. The absorption was diminished by minimizing the laser power.

The heating system was tested individually (objective or ITO flow cell heating) and together. The temperature realized by the objective heating system was restricted to 38°C avoid breaking of the objective due to thermal expansion. The maximal temperature achieved inside the flow cell by the ITO (and combined with objective) heating system(s) was $\sim 70^\circ\text{C}$. The temperature increase computed by our method and the thermocouple gave a similar temperature increase in each heating system. However, the temperature computed by our method at room temperature was typically higher. This was expected as our method is more sensitive to the temperature rise induced by laser heating.

The heating system could reach high enough temperatures to study aaFtsH. As discussed in chapter 4, the high temperature caused aggregation of the enzymes catalase and creatine kinase. These enzymes are part of the oxygen-scavenging and ATP regeneration system [11], which prevent damage of the organic compounds [12] and regenerate ATP. The oxygen-scavenging system remained absent throughout the aaFtsH experiment, but to what extent this effects the experiment is not known. The ATP regeneration system could be compensated for by doubling the ATP concentration.

Even after exclusion of these components from the experimental buffer, aggregates were still present. It was found that the zinc magnesium solution aggregated with DTT. More specifically zinc and DTT aggregate [13]. The reducing agent DTT was therefore replaced by another reducing agent, TCEP. After this replacement, aggregates were no longer observed and the aaFtsH optical tweezers measurement could be carried out.

The aaFtsH optical tweezers experiment was constructed similarly to the ClpXP optical tweezers experiment [11, 14–17]. In this construct two beads of different size are used, one bead contains the protease (aaFtsH or ClpXP) and the other bead contains the substrate with a linker, consisting of a degron-tagged multidomain (generally four (mutated) titin [18–20] I27 modules with an ssrA-tag), a Halo domain, and dsDNA. When a protease-bound and a substrate-bound bead are brought into close proximity, the protease will recognize the substrate tag and initiate unfolding and degradation. With both beads trapped, the bead displacements can be recorded and analyzed. Unfolding of one of the multidomains results in a sudden bead displacement, whereas degradation results in a gradual

5 Conclusion and outlook

bead displacement in the opposite direction.

Establishing a link between the aaFtsH-bound bead and the substrate-bound bead was rare during the optical tweezers experiment. The individual components, such as substrate (tag) and aaFtsH, have been tested and their presence or activity confirmed. However, it was found that the amount of dsDNA, that were to be incubated with the multidomain, limited the number of substrates bound to the bead. Upon increasing the amount of DNA, link formation was less rare and bead recordings of linked beads were obtained. One of these recordings was done at 45 °C. Surprisingly, it was found that links could be established at temperatures lower than activity temperatures. This would allow for successfully establishing a link and trapping beads before heating, and thus activity. However, upon heating a focal drift in the z-axis was observed, which affects the bead recording. Due to the focal drift it was decided to heat before linking. Another recording seemed to show unfolding and degradation, but with the bead displacements observed in the opposite trap. The degradation behavior was thus not further analyzed. The last recording was obtained for a link that appeared shorter than expected. During the analysis it was indeed found that the beads were closer together than expected and became even closer upon a sudden jump. The cause is unknown, but could be due to dimerization of dsDNA. Unfortunately, none of the recordings was suitable to determine the mechanical properties of aaFtsH.

5.2 Future work

Even though ClpX and FtsH both belong to the AAA+ superfamily, the mechanisms by which they unfold substrates are possibly distinct [21, 22]. It is of great interest to study the mechanical properties of FtsH, as it is essential in *E. coli* [23], an attractive drug target [24], and mutations in the human ortholog cause the disease hereditary spastic paraplegia [25, 26].

Up to date, the mechanical properties of FtsH are unknown. An attempt to study the properties has been made, but studying the thermophilic aaFtsH drastically complicated the optical tweezers experiment due to the high temperature required for aaFtsH activity. This high tempera-

ture and constant pulling force may cause the substrate to spontaneously unfold. That will affect the expected unfolding and degradation pattern observed during aaFtsH experiments. It would therefore be of value to determine the effect of our constant low pulling force and high temperature on the spontaneous unfolding rate of I27^{V13P}, I27^{V15P}, and the Halo domain. Studies of I27 with different mutations indicated that spontaneous unfolding happens upon a constant pulling force of just a few piconewton [27], with the rate of spontaneous unfolding increasing upon increasing temperatures [28]. It is likely, yet unknown, whether I27^{V13P} or the Halo domain is (partially) unfolded at 53-60 °C.

With our heating system, we can reach temperatures as high as 70 °C and might therefore be able to reach conditions at which I27^{V13P}, I27^{V15P}, and the Halo domain remain in an unfolded state. Besides that, the thermal stability of the Halo domain can be determined and we can verify whether the WLC model is suitable for them at high temperatures. To obtain these results, optical tweezers measurements with two beads of different sizes and coating (a streptavidin and an anti-digoxigenin bead for example) and a DNA-Halo-I27^{V13P}-digoxigenin or -I27^{V15P}-digoxigenin construct to link the beads can be performed. A linked bead pair can be studied by a dual beam optical tweezers, in the passive force region [29], at different constant stretching force, and at different temperatures. The thermal stability of the Halo domain can be determined in conjugation to I27^{V13P} or I27^{V15P} as the extension length of the Halo domain differs from the I27 module. Both I27 module and Halo domain unfolding extensions can be compared to the predicted extensions by the WLC model, to study if temperature affects the contour or persistence length.

When a folded state is confirmed for these constructs, aaFtsH experiments can be continued. The next step would be to investigate why link formation becomes rare after a few seconds upon heating. The biotin-streptavidin link between the bead and dsDNA linker should be stable at these temperatures [30]. Another possibility would be degradation by unbound aaFtsH. However, casein, which is also degraded by aaFtsH, is available in higher a higher concentration and would compete with the substrate. A time series of aaFtsH and the substrate can determine the time before aaFtsH becomes inactive. Inactivation of aaFtsH after prolonged degradation has been suggested before [22] and is supported by

5 Conclusion and outlook

our western blot showing undegraded ssrA-tagged substrate after 1.5 h degradation at different temperatures, section 4.5.2.

Surprisingly, the western blot showed a second band containing the ssrA-tag, when overlaid with the SDS-PAGE gel the band was found to be at the same height as aaFtsH. This suggests that the ssrA-tag somehow binds to aaFtsH. Due to the experimental procedure, it must be covalently bound. It would be interesting to investigate this more thoroughly. Does this linking cause inactivation of aaFtsH? Can it bind multiple ssrA-tags? Does it bind other tags? And in the end, determine why does the ssrA-tag bind to aaFtsH?

Finally, our novel heating system allows for future studies. Our system can be used to quickly heat up an optical tweezers sample to temperatures as high as 70 °C, and our novel method for local temperature determination or the thin thermocouple that fits in a flow cell can be used to (quickly) determine the temperature, as described in chapter 3. Our novel E-DF method, to determine the temperature, requires prior knowledge of the change in viscosity upon temperature. But the relation can also be studied when a thermocouple is added to measure temperature and the trapped bead to determine the viscosity. Besides that, the heating system can be used to study processes at temperatures above room temperature and is especially valuable for any objective-condenser optical tweezers setup. Nonetheless, our heating system is not limited to optical tweezers setups, but can be used on all sorts of microscope setups.

References

- (1) Ashkin, A. Acceleration and Trapping of Particles by Radiation Pressure. *Physical Review Letters* **1970**, *24*, 156–159.
- (2) Ashkin, A.; Dziedzic, J. M.; Bjorkholm, J. E.; Chu, S. Observation of a single-beam gradient force optical trap for dielectric particles. *Optics Letters* **1986**, *11*, 288.
- (3) Schumann, W. FtsH - a single-chain charonin? *FEMS Microbiology Reviews* **1999**, *23*, 1–11.
- (4) Sung, J.; Sivaramakrishnan, S.; Dunn, A. R.; Spudich, J. A. In *Methods in Enzymology*; Elsevier: 2010; Chapter 14, pp 321–375.
- (5) Carvalho, V.; Prabudiansyah, I.; Kovacik, L.; Chami, M.; Kieffer, R.; van der Valk, R.; de Lange, N.; Engel, A.; Aubin-Tam, M.-E. The cytoplasmic domain of the AAA+ protease FtsH is tilted with respect to the membrane to facilitate substrate entry. *Journal of Biological Chemistry* **2021**, *296*, 100029.
- (6) Deckert, G.; Warren, P. V.; Gaasterland, T.; Young, W. G.; Lenox, A. L.; Graham, D. E.; Overbeek, R.; Snead, M. A.; Keller, M.; Aujay, M.; Huber, R.; Feldman, R. A.; Short, J. M.; Olsen, G. J.; Swanson, R. V. The complete genome of the hyperthermophilic bacterium *Aquifex aeolicus*. *Nature* **1998**, *392*, 353–358.
- (7) Joule, J. P. On the production of heat by voltaic electricity. *Abstracts of the Papers Printed in the Philosophical Transactions of the Royal Society of London* **1843**, *4*, 280–282.
- (8) Peterman, E. J. G.; Gittes, F.; Schmidt, C. F. Laser-Induced Heating in Optical Traps. *Biophysical Journal* **2003**, *84*, 1308–1316.
- (9) Ebert, S.; Travis, K.; Lincoln, B.; Guck, J. Fluorescence ratio thermometry in a microfluidic dual-beam laser trap. *Optics Express* **2007**, *15*, 15493.
- (10) Català, F.; Marsà, F.; Montes-Usategui, M.; Farré, A.; Martín-Badosa, E. Influence of experimental parameters on the laser heating of an optical trap. *Scientific Reports* **2017**, *7*, DOI: 10.1038/s41598-017-15904-6.

5 Conclusion and outlook

- (11) Aubin-Tam, M.-E.; Olivares, A. O.; Sauer, R. T.; Baker, T. A.; Lang, M. J. Single-Molecule Protein Unfolding and Translocation by an ATP-Fueled Proteolytic Machine. *Cell* **2011**, *145*, 257–267.
- (12) Fridovich, I. The Biology of Oxygen Radicals. *Science* **1978**, *201*, 875–880.
- (13) Cornell, N. W.; Crivaro, K. E. Stability constant for the zinc-dithiothreitol complex. *Analytical Biochemistry* **1972**, *47*, 203–208.
- (14) Cordova, J. C.; Olivares, A. O.; Shin, Y.; Stinson, B. M.; Calmat, S.; Schmitz, K. R.; Aubin-Tam, M.-E.; Baker, T. A.; Lang, M. J.; Sauer, R. T. Stochastic but Highly Coordinated Protein Unfolding and Translocation by the ClpXP Proteolytic Machine. *Cell* **2014**, *158*, 647–658.
- (15) Olivares, A. O.; Nager, A. R.; Iosefson, O.; Sauer, R. T.; Baker, T. A. Mechanochemical basis of protein degradation by a double-ring AAA+ machine. *Nature Structural; Molecular Biology* **2014**, *21*, 871–875.
- (16) Iosefson, O.; Olivares, A. O.; Baker, T. A.; Sauer, R. T. Dissection of Axial-Pore Loop Function during Unfolding and Translocation by a AAA+ Proteolytic Machine. *Cell Reports* **2015**, *12*, 1032–1041.
- (17) Olivares, A. O.; Kotamarthi, H. C.; Stein, B. J.; Sauer, R. T.; Baker, T. A. Effect of directional pulling on mechanical protein degradation by ATP-dependent proteolytic machines. *Proceedings of the National Academy of Sciences* **2017**, *114*, DOI: 10.1073/pnas.1707794114.
- (18) Politou, A.; Thomas, D.; Pastore, A. The folding and stability of titin immunoglobulin-like modules, with implications for the mechanism of elasticity. *Biophysical Journal* **1995**, *69*, 2601–2610.
- (19) Improta, S.; Politou, A. S.; Pastore, A. Immunoglobulin-like modules from titin I-band: extensible components of muscle elasticity. *Structure* **1996**, *4*, 323–337.
- (20) Linke, W. A.; Ivemeyer, M.; Olivieri, N.; Kolmerer, B.; Rüegg, C. J.; Labeit, S. Towards a Molecular Understanding of the Elasticity of Titin. *Journal of Molecular Biology* **1996**, *261*, 62–71.

- (21) Snider, J.; Thibault, G.; Houry, W. A. The AAA+ superfamily of functionally diverse proteins. *Genome Biology* **2008**, *9*, 216.
- (22) Yang, Y.; Gunasekara, M.; Muhammednazaar, S.; Li, Z.; Hong, H. Proteolysis mediated by the membrane-integrated ATP-dependent protease FtsH has a unique nonlinear dependence on ATP hydrolysis rates. *Protein Science* **2019**, DOI: 10.1002/pro.3629.
- (23) Hanson, P. I.; Whiteheart, S. W. AAA+ proteins: have engine, will work. *Nature Reviews Molecular Cell Biology* **2005**, *6*, 519–529.
- (24) Hinz, A.; Lee, S.; Jacoby, K.; Manoil, C. Membrane Proteases and Aminoglycoside Antibiotic Resistance. *Journal of Bacteriology* **2011**, *193*, 4790–4797.
- (25) Nolden, M.; Ehses, S.; Koppen, M.; Bernacchia, A.; Rugarli, E. I.; Langer, T. The m-AAA Protease Defective in Hereditary Spastic Paraplegia Controls Ribosome Assembly in Mitochondria. *Cell* **2005**, *123*, 277–289.
- (26) Ruer, M.; Krainer, G.; Gröger, P.; Schlierf, M. ATPase and Protease Domain Movements in the Bacterial AAA+ Protease FtsH Are Driven by Thermal Fluctuations. *Journal of Molecular Biology* **2018**, *430*, 4592–4602.
- (27) Yuan, G.; Le, S.; Yao, M.; Qian, H.; Zhou, X.; Yan, J.; Chen, H. Elasticity of the Transition State Leading to an Unexpected Mechanical Stabilization of Titin Immunoglobulin Domains. *Angewandte Chemie International Edition* **2017**, *56*, 5490–5493.
- (28) Yu, M.; Lu, J.-H.; Le, S.; Yan, J. Unexpected Low Mechanical Stability of Titin I27 Domain at Physiologically Relevant Temperature. *The Journal of Physical Chemistry Letters* **2021**, *12*, 7914–7920.
- (29) Greenleaf, W. J.; Woodside, M. T.; Abbondanzieri, E. A.; Block, S. M. Passive All-Optical Force Clamp for High-Resolution Laser Trapping. *Physical Review Letters* **2005**, *95*, 208102.
- (30) González, M.; Argaraña, C. E.; Fidelio, G. D. Extremely high thermal stability of streptavidin and avidin upon biotin binding. *Biomolecular Engineering* **1999**, *16*, 67–72.

Acknowledgements

Over these past five, almost six, years many (unseen) things have happened and changed. The most apparent one is that I am no longer at the beginning of my PhD, but at the end. In this period, I have grown as a scientist by experiencing (many) experimental challenges, becoming a more confident speaker, and experiencing satisfaction in writing this thesis. It also confirmed the joy I expected to find in being in such a diverse, changing, scientific, and challenging environment. I am grateful for experiencing this challenging and unforgettable journey.

I want to start by thanking Dr. Marie-Eve Aubin-Tam who found me qualified for this study. I really appreciate the support and time you invested in me. Without your advice and care this experience would not have been the same and I would probably have been doing the same experiment over and over again while expecting a different outcome. I learned to take a step back to examine the results and to come-up with a different approach or supporting experiments.

I would like to thank Prof. Dr. Christophe Danelon and Dr. Arjen Jakobi, for being my go/no-go committee and (co)promotor. I would also like to apologize to Prof. Dr. Christophe for the unexpected and rushed decision to change (co)promotor. At the same time I would like to thank Dr. Arjen Jakobi for taking over the (co)promotor position of Prof. Dr. Christophe Danelon.

Then for my colleagues who have helped me throughout (parts of) my PhD journey. I would like to thank Dr. Ramon van der Valk. This experience would not have been so wonderful without your unlimited supply of cookies and other treats. Besides that, thank you for helping me tout in the wet lab, discussing results, and in general. Thank you Dr. Roland Kieffer for designing the heating flow cells, helping me out with (building)

Acknowledgements

the optical tweezers, writing the paper, and the (amusing) stories during lunch time.

Thank you Dr. Irfan Prabudiansyah and Dr. Vanessa De Carvalho (who I only met during her PhD defense) for being able to purify FtsH and thereby creating the opportunity of this PhD for me. Thank you Dr. Martin Caldarola for helping me programming the optical tweezers setup. Thank you Dr. René Delfos for letting us use the thermal camera.

A more personally related thanks to Dr. Auro Dols-Perez and Dr. Cecilia de Agrela Pinto. Thank you Aurora for supporting me during the emotional rollercoaster I went through. And, not to forget, the cocktails we had outside office hours with Dr. Guillermo Amador. I especially enjoyed the time you were a part of Marie's group. Thank you Cecilia for all the talks, walks, and coffees we shared. I guess you are not just an almost colleague, but more a friend.

A warm thanks to all other (previous) members of Marie's group. Dr. Dominik Schmieden, Dr. Da Wei, Dr. Ewa Spiesz, Dr. Kuang Liang, Dr. Kui Yu (who I saw coming without a doctorate, leaving with a doctorate, and coming back for a postdoc), Dr. Guillermo Amador, Dr. Lisa Dreesens, Dr. Srikanth Balasubramanian, Arash Yahyazadeh Shourabi, Donna van der Rijst, Ingo Nettersheim, Dr. Friedrich Kleiner, Dr. Jeong-Joo Oh, Djanick de Jong, Fan Jiang and Franka van der Linden.

Papa en mama, ik wil jullie ook graag bedanken. Jullie staan altijd voor me klaar en zijn altijd bereid om me te helpen. Ook toen ik zei dat ik graag natuurkunde aan de universiteit wilde gaan studeren in plaats van de HBO studie die ik toen deed. In mijn ogen was dit heel normaal en ook uit jullie reactie heb ik nooit op kunnen maken dat dit misschien niet zo normaal was. Bedankt dat jullie altijd in mij geloven.

Bedankt Amber en Zilla, ik weet dat ik minder vaak contact met jullie opneem dan dat jullie en ik zouden willen. Ik waardeer het echt dat jullie dan contact met mij zoeken en ik hoop dat jullie dit blijven doen.

Wietske, dankjewel voor het helpen met het ontwerpen van de cover. Zonder jou was deze niet zo vurig.

Finally, I would like to thank my husband Bas. Thank you for supporting me throughout all of the struggles, hopes and disappointments that I ex-

perienced during this PhD. You always make me smile with your puns and I would like to believe that, since I met you, I improved on recognizing them and making them. But most of all, thank you for having our two beautiful little daughters with me. They are very time consuming, but worth every second of my time as they tend to fulfill me with so much love and joy.

Curriculum Vitæ

Chaline Maria Margerethe Overtoom-van Aatrijk

31-10-1993 Born in Hilversum, The Netherlands

Education

2010-2011 Completed first year of Life Sciences and Chemistry
Hogeschool Utrecht, Utrecht, The Netherlands

2011-2014 B.Sc. in Physics
University of Groningen, Groningen, The Netherlands

2014-2016 M.Sc. in Neurophysics
Radboud University, Nijmegen, The Netherlands

2018-2023 Ph.D. candidate in Biophysics
Delft University of Technology, Delft, The Netherlands
*Studying protein unfolding and translocation by the protease
FtsH with optical tweezers*
Promotor: Dr. M.-E. Aubin-Tam
Copromotor: Dr. A. Jakobi

